IEEE Power & Energy Society

TECHNICAL REPORT

April 2018

PES-TR66

Microgrid Stability Definitions, Analysis, and Modeling

PREPARED BY THE

IEEE PES Power System Dynamic Performance Committee

IEEE PES Task Force on Microgrid Stability Analysis and Modeling

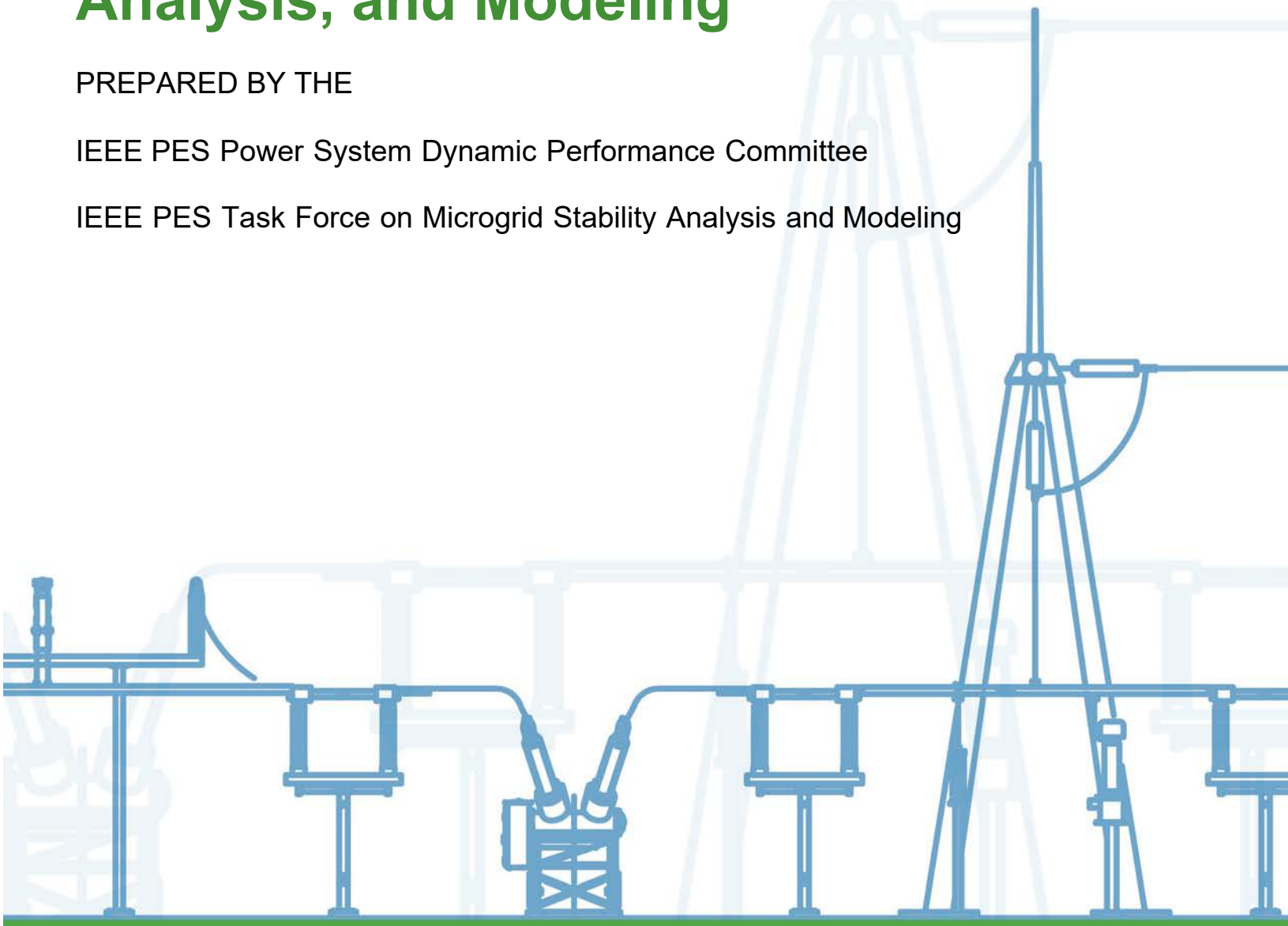

THIS PAGE LEFT BLANK INTENTIONALLY

Task Force on Microgrid Stability Analysis and Modeling

Chair: Claudio A. Cañizares, *University of Waterloo*
Co-Chair: Jim Reilly, *Reilly Associates*
Secretary: Rodrigo Palma Behnke, *University of Chile*

Contributors

Mostafa Farrokhabadi, *University of Waterloo*
Claudio A. Cañizares, *University of Waterloo*
John W. Simpson-Porco, *University of Waterloo*
Ehsan Nasr-Azadani, *Canadian Solar*
Lingling Fan, *University of South Florida*
Patricio A. Mendoza Araya, *University of Chile*
Reinaldo Tonkoski, *South Dakota State University*
Ujjwol Tamrakar, *South Dakota State University*
Nikos Hatziargyriou, *National Technical University of Athens*
Dimitris Lagos, *National Technical University of Athens*
Richard W. Wies, *University of Alaska Fairbanks*
Mario Paolone, *Ecole polytechnique fédérale de Lausanne (EPFL)*
Marco Liserre, *University of Kiel*
Lasantha Meegahapola, *RMIT University*
Mahmoud Kabalan, *University of St. Thomas*
Amir H. Hajimiragha, *IOTSEG*
Dario Peralta, *University of Waterloo*
Marcelo Elizondo, *Pacific Northwest National Laboratory (PNNL)*
Kevin P. Schneider, *Pacific Northwest National Laboratory (PNNL)*
Frank Tuffner, *Pacific Northwest National Laboratory (PNNL)*
Jim Reilly*, Reilly Associates*

Reviewers

Andreas Sumper, *Polytechnic University of Catalonia (UPC)*
Monica Aragues, *Polytechnic University of Catalonia (UPC)*

Abstract

This document defines concepts and identifies relevant issues related to stability in microgrids. It proposes a definition and a classification of microgrid stability, taking into account pertinent microgrid features such as voltage-frequency dependency, unbalancing, low inertia, and generation intermittency. The modeling of microgrid components such as generators, converters, distribution lines, loads, and distributed energy resources for stability analysis is discussed in detail. Analysis techniques and tools relevant to microgrid stability are also reviewed, as well as various examples highlighting some of the stability classes defined in this report.

KEYWORDS

Classification, definitions, microgrids, stability, modeling, techniques, tools, examples.

CONTENTS

THIS PAGE LEFT BLANK INTENTIONALLY

1. INTRODUCTION

Although small isolated grids have existed for decades in remote communities, the concept of a microgrid was initially introduced in [1], in the context of integration of Distributed Energy Resources (DERs) and controllable loads. Generally, a microgrid is defined as a group of DERs, including Renewable Energy Resources (RES) and Energy Storage Systems (ESS), and loads, that operate together locally as a single controllable entity [2] [3]. Microgrids exist in various sizes and configurations; they can be large and complex networks with various generation resources and storage units serving multiple loads, or small and simple systems supplying a single customer [3]–[5].

Microgrids exist in both grid-connected and isolated forms. Grid-connected microgrids have a Point of Interconnection (POI) or Point of Common Coupling (PCC) with a large power network and should be capable of seamless transition to islanded mode of operation [6], [7]. In both grid-connected and islanded/isolated operation modes, microgrids should maintain balance between generation and consumption, while satisfying certain reliability, power quality, and adequacy standards. To achieve these objectives, all controllable DERs and loads should be actively involved in keeping the system voltage and frequency stable and within acceptable ranges [6], [8]. In grid-connected microgrids, islanding can occur intentionally (e.g., to perform scheduled maintenance), or unintentionally due to the faults; in both cases, a microgrid should utilize appropriate control techniques to continue its operation [9]. On the other hand, isolated microgrids have no POI/PCC, thus islanding is not an issue in these systems; examples of isolated microgrids are those for remote communities and industrial sites [10]–[14].

Microgrids have received considerable attention in the past two decades, driven by global environmental issues, the need for energy access in remote communities, and the promise of increased system resiliency and reliability [15], [16]. Specifically, microgrids are considered a critical link in the evolution from vertically integrated bulk power systems to smart decentralized networks, by facilitating the integration of DERs [3], [17]. Entities, such as government agencies, utilities, military bases, and universities around the world are deploying microgrids, and an increasing number of microgrids are expected to be developed in the next decade [18]. Therefore, a clear understanding of microgrid system behavior, control, and stability is essential to ensure the successful transition to active decentralized power systems.

In general, stability in microgrids has been treated from the perspective of conventional bulk power systems [19]. However, intrinsic differences between microgrids and bulk power systems, such as size, feeder types, high share of RES, converter-interfaced components, low inertia, and unbalanced operation require a review of the stability

definitions, classification, component modeling, and analysis techniques and tools in the context of microgrids. Specialized microgrid stability definitions are necessary to reflect realistic system needs and operating conditions, and corresponding analysis methods are then required for the design of more efficient and robust microgrids. In this context, this document aims to provide a detailed discussion of stability in microgrids to address the aforementioned needs and requirements. Some related mitigation solutions to stability problems are also discussed in this document; however, protection issues are not considered here.

The remaining sections of this document are organized as follows:

- Section 2 discusses the main differences between microgrids and conventional power systems. Key microgrid characteristics, such as small system size, high penetration of RES, low system inertia, etc., are discussed and their impact is analyzed from the stability perspective.
- Section 3 introduces various stability concepts pertinent to microgrids, and proposes a proper stability classification. Thus, two major stability categories are proposed: Control System Stability, and Power Supply and Balance Stability. Control System Stability is categorized into Electric Machine and Converter Stability, and Power Supply and Balance Stability is categorized into Voltage and Frequency Stability. A discussion is provided with respect to large and small disturbances.
- Section 4 presents an overview of different component modeling from the perspective of microgrid stability. Various DERs, including synchronous machine, solar PV, wind turbine, ESS, and flywheel are discussed. In addition, generic models are presented for distribution feeders and static and dynamic loads. Finally, a discussion is provided on some major analysis tools and techniques, including methodologies to investigate large- and small-perturbation stability in microgrids.
- Section 5 presents and discusses relevant examples pertaining to various stability issues in microgrids, including examples of frequency and voltage instabilities, and converter stability problems.
- Section 6 provides a summary of the document.

2. MICROGRID UNIQUE CHARACTERISTICS: RETHINKING STABILITY CONCEPTS

In grid-connected mode of operation, voltage and frequency are mainly imposed by the main grid, limiting the microgrid role to performing ancillary services. Therefore, the problem of stability in grid-connected microgrids reduces to the stability of individual components such as a particular DER or of a set of local loads, including electrical motors,

and their impact on the system, as discussed in detail in [20]. With IEEE Standard 1547 allowing for the islanded operation of distribution networks [21], isolated microgrids are expected to play a significant role in smart active distribution grids; in this case, the system voltage and frequency are no longer supported by the main grid, and different DERs must maintain these variables in acceptable ranges. Due to the microgrid unique intrinsic features and systemic differences, operating them in standalone mode is more challenging than conventional power systems, facing particular stability and system adequacy problems [22]. These differences should be considered to ensure an efficient and adequate control of system variables. In the context of stability, the main relevant issues are discussed herein.

Many countries around the world provide incentives to invest in renewable energy, targeting a considerable increase in RES; examples of such efforts in the European Union, Germany, and Canada can be found in [23]–[25]. In addition, RES prices have decreased considerably over the last decade, making them a financially viable alternative to fossil-fuel-based generation in microgrids (e.g., [10]). As a result, the share of RES, such as wind turbines and solar PV units, operating in medium and low voltage grids has increased [26]. Since demand-supply balance is critical in microgrids, the intermittent and uncertain nature of RES such as wind turbines and PV units is particularly relevant in these systems, especially in isolated/islanded operation mode [27]. Bi-directional power flows between generators and prosumers are also an issue [26], due to complications in control and protection coordination [3]. Finally, since electric power is supplied by electronically-interfaced DERs and relatively small synchronous machines, system inertia is considerably lower in microgrids compared to conventional power systems.

The nature of stability problem and dynamic performance of a microgrid are considerably different than those of a conventional power system, since the microgrids system size is considerably smaller than that of a conventional large interconnected power system. Furthermore, microgrid feeders are relatively short and operated at medium voltage levels, forming a lower reactance to resistance ratio compared to conventional systems [28]. As a result, the dynamic performance of microgrids and the intrinsic mathematical relationships between voltages, angles, and active and reactive power flows are different than in conventional grids. Another consequence of the microgrid small size is higher uncertainty in the system, due to the reduced number of loads and highly correlated and fast variations of available RES [3].

In general, microgrid DERs such as diesel gensets are capable of significant temporary overloads, while converter-based sources have much lower ride-through capabilities. Thus, for low-inertia microgrids, with inverter-interfaced DERs, stability problems are likely to appear following a fault/failure at the utility side, due to the limited ride-through capability of the inverters and the relatively long disconnection time of breakers.

A significant concern in islanded microgrids, especially in remote communities with small distribution systems, is their relatively low short-circuit capacity. In such systems, even a small change in the microgrid configuration (e.g., start up or shut down of a diesel genset) can result in relatively large voltage and frequency deviations. This poses stability challenges especially when operating conventional synchronous generators and inverter-interfaced power generation resources together, since perturbations in this case may lead to inverter shut down. Hence, special attention should be put in this case on the design of power electronics systems to withstand voltage and frequency disturbances in such weak microgrids [11].

Unlike conventional power systems, loading in microgrids is typically unbalanced [29], which can be as significant as 100% between the three phases [30], [31]. Operating microgrids under such significant unbalance levels may jeopardize system stability [32], and requires controls that are designed to handle these conditions. In addition, traditional stability analysis techniques and models assume balanced operation, and therefore are not valid in unbalanced systems.

Considering the above-mentioned unique characteristics of microgrids, concepts, analysis techniques and tools, models, and controls for conventional power systems are not adequate for stable and reliable operation of microgrids. It follows that new analytical models, methods, controls, and tools are needed in the context of microgrids.

Summarizing, the most important differences of microgrids compared to large-scale traditional grids relevant to stability, motivating the present document, are the following:

- Smaller system size.
- Higher penetration of RES.
- Higher uncertainty in the system.
- Lower system inertia.
- Higher R/X ratio of the feeders.
- Low short-circuit capacities.
- Unbalanced three-phase loading.

3. DEFINITION AND CLASSIFICATION OF STABILITY IN MICROGRIDS

Stability in microgrids is based on the same principles as stability in conventional power systems [19]. The aim of this document is to identify and investigate relevant stability issues pertaining to the unique features of microgrids. This section proposes a definition and classification of stability in microgrids, discussing various stability issues especially pertinent to these systems.

3.1 Definitions

Consider a microgrid which is operating in equilibrium, with state variables taking on appropriate steady-state values satisfying operational constraints, such as acceptable ranges of currents, voltages, and frequency. Such a microgrid is stable if, after being subjected to a disturbance, all state variables recover to (possibly new) state-state values which satisfy operational constraints (e.g., [33]), and without the occurrence of involuntary load shedding. Note that a microgrid that performs voluntary load shedding, (e.g., demand response [34]), is considered stable if it meets the aforementioned conditions. In addition, if loads are disconnected to isolate faulted elements after a disturbance, and not for the sole purpose of shedding load due to system problems such as voltage or frequency issues, and the microgrid meets the aforementioned conditions, the system can also be considered stable.

In traditional power systems, due to the high number of loads and the large scale of the system, intentional tripping of loads is acceptable to preserve the continuity of its operation [35]; no single load has priority over the stability of the system as a whole. In contrast, microgrids are designed to serve a relatively small number of loads, and hence the operator can prioritize the connectivity of certain feeders (e.g., one that supplies a hospital) over the rest of the system; if such a critical feeder(s) is tripped, the microgrid is no longer achieving its primary objective. Thus, intentional tripping of loads to maintain the operation of the rest of the system during or after a disturbance, other than the specific ones previously mentioned, renders the system unstable by the definition presented here.

In above definition, disturbances represent any exogenous inputs, and may correspond to load changes, component failures, or operational mode/set-point adjustments. If the disturbances are considered to be “small”, such as minor load fluctuations, it is referred here as small-disturbance stability, as usual. Otherwise, the system would be called large-disturbance stable with respect to the corresponding disturbance if the microgrid is stable as previously defined. For example, an unplanned transition between grid-connected and islanded modes of operation is considered a large disturbance.

3.2 Classification

Due to the systemic differences between microgrids and conventional power systems, new types of stability issues can be observed in microgrids. For example, in conventional systems, transient and voltage stability problems typically occur more often than frequency stability ones, whereas in isolated/islanded microgrids, maintaining frequency stability is more challenging due to the low system inertia and a high share of variable RES. In addition, some stability problems observed in large interconnected systems, such as inter-area oscillations and voltage collapse, have not been observed in microgrids. Thus, there is a need to review and modify the power system stability classifications in [19] to properly reflect relevant stability issues in microgrids.

Based on the concept of “partial stability” [36], [37], stability in microgrids can be categorized according to the physical cause of the unstability, the relative size of the disturbance, the physical components that are involved in the process, the time-span during which the instability occurs, and the methodology to analyze or predict the instability, as in [19].

Due to the low X/R ratios of microgrid feeder lines, active and reactive power flows cannot be decoupled, and hence voltage and frequency are strongly coupled in microgrids. Thus, contrary to some instability phenomena in conventional systems such as voltage collapse, instability in microgrids is manifested by fluctuations in all system variables. This strong coupling between system variables makes it quite difficult to classify instability phenomena as "voltage instability" or "frequency instability" based solely on measurements of those respective variables. Given this difficulty, the more useful classification scheme proposed here places more emphasis on the type of the equipment and/or controllers that are involved in the instability process, triggered by a system disturbance.

Based on the aforementioned discussion, Fig. 1 illustrates the classification of stability in microgrids stipulated herein. Here it is proposed that stability considerations in microgrids should be divided into two main categories: phenomena pertaining to the equipment control systems, and phenomena pertaining to active and reactive power sharing and balance. The rest of this section discusses each type of stability depicted in Fig. 1 for microgrids.

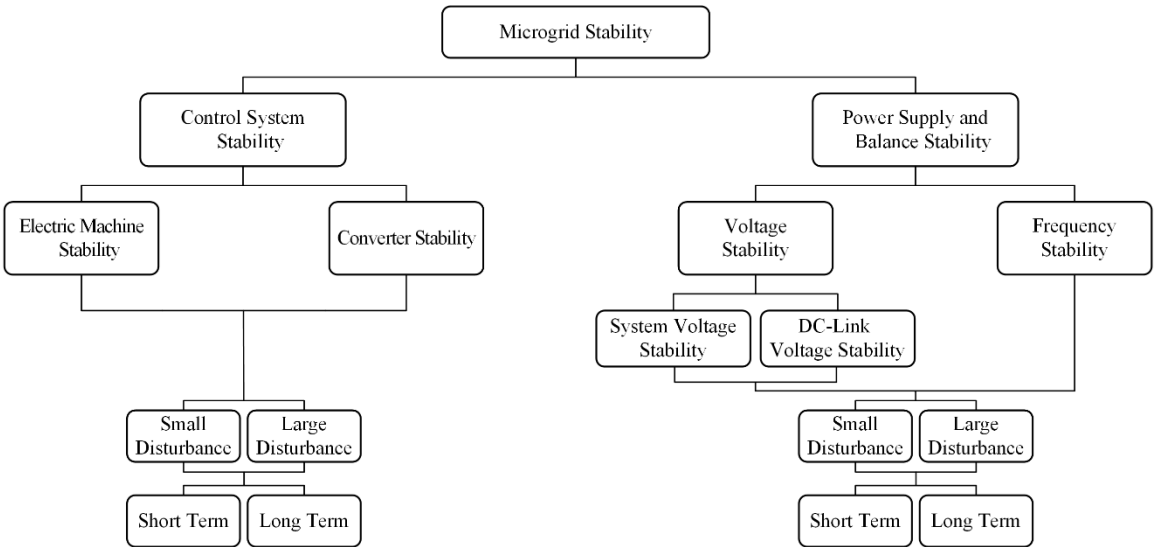

Fig. 1. Classification of stability in microgrids.

3.3 Power Supply and Balance Stability

Power Supply and Balance Stability pertains to the ability of the system to maintain the power balance, and effectively share the demand power among DERs, so that the system satisfies operational requirements. These types of stability issues are associated with the loss of a generation unit, violation of DERs power limits, poor power sharing among multiple DERs, wrong selection of slack(s) resources [38], and/or involuntary no-fault load tripping. This class of stability can be subcategorized into Frequency and Voltage Stability, as explained next.

3.3.1 Frequency Stability

Frequency regulation is a major concern in isolated/islanded microgrids, due to the systemic features explained in Section 2, including low system inertia and a high share of intermittent RES. In addition, the low number of generation units in microgrids puts the system at risk of large disturbances in the event of generator outages. Therefore, for such disturbances, the system frequency may experience large excursions at a high rate of change, jeopardizing the system frequency stability [39], [40]. In this context, conventional frequency control techniques and technologies may not be fast enough to overcome the rapid change of system frequency, even in the presence of sufficient generation reserve. Actual examples of such events have been reported around the world [41], [42].

Strong coupling between voltage and frequency in microgrids further complicates frequency regulation. First, due to the high R/X ratios of microgrid feeders, the

conventional decoupling of active power flow and voltage magnitudes is no longer valid [43]. Second, because of the relatively small scale of microgrids, voltage changes at the DERs terminals are almost instantaneously reflected on the load side, which in turn changes the system demand depending on the load voltage sensitivity indices [44]–[46]. Therefore, this voltage-frequency coupling should be accounted for in the stability analysis and control of frequency in microgrids.

Frequency instability can be triggered for a variety of reasons in microgrids. For example, a large load increase accompanied by inadequate system response can result in a fast decay of frequency, due to low system inertia, leading to a system blackout triggered by the protection scheme [39]. Poor coordination of multiple frequency controllers and power sharing among DERs may trigger small-perturbation stability issues resulting in undamped frequency oscillations in the span of a few seconds to a few minutes, a phenomenon rarely observed in large grids [47]. Hence, depending on the time it takes for the frequency protection schemes to trip the system, this may result in a long-term frequency instability. Insufficient generation reserve can also lead to the steady-state frequency being outside acceptable operating ranges, activating under-frequency load tripping relays, as in large grids. On the other hand, traditional long-term frequency instabilities in larger grids pertaining to steam turbine overspeed controls and boiler and reactive protection and control schemes [19] are not relevant in microgrids.

3.3.2 Voltage Stability

In conventional power systems, a major root cause of voltage instability is long transmission lines, which limit the power transfer between generation and loads. However, in microgrids, the feeders are relatively short, resulting in relatively small voltage drops between the sending and receiving ends of the feeders [29], [44]. Thus, voltage collapse, i.e., the slow and sustained decay of voltage associated with load recovery process and reactive power supply capacity, has not been observed in microgrids. Nevertheless, with the current distribution networks evolving into microgrids, voltage drops and current limits may become an issue, in particular for weaker and older grids [48].

In microgrids, the limits of DERs and the sensitivity of load power consumption to supplied voltage are critical factors in voltage instability. Thus, voltage instabilities in the form of unacceptable low steady-state and dynamic voltages may occur. One other major root cause of voltage instability is poor reactive power sharing among DERs in the system. In bulk power systems, reactive power is mostly managed locally by regulating the voltage at the terminals of generators and compensated loads. However, in microgrids, the feeders are short, and thus any changes in the DER terminal voltages are almost immediately reflected in the rest of the system. Hence, small differences in voltage magnitudes at DERs, if not properly coordinated, will yield high circulating reactive power flows and thus result in

large voltage oscillations [49]. Moreover, if reactive power is not properly shared, in the worst cases, it could cause pole slipping in a machine in the system.

Proper reactive power sharing among multiple DERs in a microgrid is most commonly done in practice through voltage-reactive power droop, similar to multiple generator plants in large power systems. As in the case of classical active power-frequency droop, under the voltage-reactive power droop paradigm, the output voltage magnitude reference of a DER linearly decreases as its reactive power injection increases [50]; thus, DERs with steeper voltage-reactive power droop slopes have a higher contribution to the reactive power supply of the system. This droop mechanism fails to achieve the desired reactive power sharing, for three main reasons [51]. First, unlike frequency, voltage magnitude varies, albeit slightly, throughout the system, and thus local voltage measurements cannot be easily used to enforce global reactive power sharing. Second, the concept of voltage droop has been developed based on the premise that the lines are inductive, thus reactive power flow is tightly coupled with voltage magnitude; however, as discussed in Section 2, such an assumption is generally not valid in microgrids. Finally, the relation between the system voltage and reactive power consumption is determined by the load voltage sensitivity, which is nonlinear in general.

Reactive droop compensation has the advantages of simple implementation and interoperability of dissimilar DERs and control systems; however, this approach is prone to steady-state voltage deviations in islanded microgrids. In this case, techniques that minimize these deviations would be more effective for reactive power load sharing among parallel DERs in microgrids. Cross current compensation is such an approach, in which the voltage remains the same in steady-state from no load to full load on the system. This technique is based on the insertion of a Current Transformer (CT), usually on phase *b* of each DER, and interconnecting the CTs together to provide an identical voltage bias to each Automatic Voltage Regulator (AVR) in the system [52]. Hence, it presents a better performance compared to reactive droop compensation. The disadvantage is that voltage regulators of DERs would have to be identical for this approach to work.

Another method that also yields no deviation in steady-state terminal voltage is isochronous reactive power load sharing [52], which is similar to the isochronous active power load sharing approach, and thus requires a communication link between individual DERs in an islanded microgrid [53]. This technique is based on each AVR receiving an additional signal from other AVRs that force the set-point to slightly increase or decrease to ensure that reactive power load sharing with other DERs remains at a fixed percentage of the DER's reactive power rating. This technique is based on the communication of reactive power load sharing data between individual DERs, which is an issue when interfacing dissimilar DERs; thus special care is needed in this case when communicating the reactive power load sharing data.

Another type of voltage stability in microgrids pertains to the ability of VSC-based DERs to maintain the voltage across the dc-link capacitor. Depending on the DER type, this voltage is maintained via a buck/boost converter or a dc/ac inverter; either way, the voltage ripples across the capacitor depend on the injected/absorbed instantaneous power of the inverter. Therefore, situations may occur where the active power injection of the inverter is close to its limit value, in which case an increase in the reactive power demand may result in undamped ripples in the voltage across the dc-link capacitor; as a result, large fluctuations occur in the active and reactive power injection of DERs, as demonstrated in the Section 5.1.1.

Depending on the system response and load characteristics, a voltage instability may occur following a large disturbance, such as a sudden change in the demand and/or output of RES, or a generator outage. Small disturbances, such as small incremental changes in the demand can also result in voltage instabilities, in particular for systems which are close to their loading limits or are highly unbalanced, as shown in Section 5. In terms of the time-frame, voltage instability can be a short-term or a long-term phenomenon. Short-term voltage instabilities arise from poor control coordination, or fast dynamics changes in the active and/or reactive power mismatch. On the other hand, long-term voltage instabilities in microgrids pertain to DERs output limits being gradually reached by a steady increase in the demand, as in the case of thermoelectrical loads.

3.4 Control System Stability

Control System Stability issues may arise due to inadequate control schemes (e.g., harmonic resonance of parallel DERs) and/or poor tuning of one or more equipment controllers. In the latter case, the poorly tuned controller(s) is the primary source of instability, and the system cannot be stabilized, by the definition provided in Section 3.1, until the controller is re-tuned or the associated piece of equipment is disconnected. This type of stability pertains to electric machines and inverter control loops, LCL filters, and PLLs. This category of stability is subcategorized into Electric Machine and Converter Stability, as explained next.

3.4.1 Electric Machine Stability

Conventionally, these types of stability studies are concerned with the ability of synchronous machines to return to synchronism with the rest of the system following the angular acceleration of these machines during a fault. However, this phenomenon has not been observed in microgrids. In fact, due to the resistive nature of microgrids, synchronous machines are likely to decelerate during short-circuits, as demonstrated by the experimental results discussed in [54], where faults result in large dips in voltage angles and magnitudes for both synchronous machines and inverter-based DERs in islanded/isolated microgrids.

In conventional power systems, small-perturbation stability issues can be manifested either by an aperiodic increase or undamped oscillations of the rotor angle of the synchronous generators [55]. The former instability occurs due to the lack of synchronizing torque, while the latter happens because of inadequate damping torque. However, in the context of microgrids, synchronizing and damping torque problems have not been observed in generators equipped with well-tuned voltage regulators and governors. From the aforementioned discussions, electric machine stability in microgrids is dominantly associated with poor tuning of synchronous machines' exciters and governors [31].

3.4.2 Inverter Stability

In microgrids, inverters inner voltage and current control loops are a major concern for small-perturbation stability of the system, since their tuning is a challenging issue in practice. In addition, a system blackout after large disturbances due to tripping of DERs, in particular inverter-based RES due to under-frequency and under-voltage protection schemes are a serious concern.

Contrary to low-frequency oscillations caused by outer power controls, interaction of inner current and voltage control loops may cause high harmonic-frequency oscillations, in the range of hundreds of Hz to several kHz [56], [57], a phenomenon referred to as harmonic instability. The presence of several inverters at close distance also generates interaction problems resulting in multi-resonance peaks [58]. Another root-cause of harmonic instability is high-frequency switching, triggering the parallel and series resonance introduced by LCL power filters or parasitic capacitors of feeders [56], [59]. The resonance of an inverter LCL filter can be also triggered by the control of the inverter itself or by interactions with controllers nearby [60]. Harmonic instability can be prevented and/or mitigated by so called active damping strategies [60], [61].

From the system point of view, the wide usage of grid synchronization strategies based on PLLs in grid-following/feeding inverters modifies the impedance and admittance matrices of the power system, which may lead to instabilities [62]. It has been shown that PLLs introduce a negative parallel admittance to the input admittance, which jeopardizes the stability of the system [63]. This effect on the output admittance within the PLL control bandwidth can affect the system voltages, and can be mitigated by reducing the PLL bandwidth [64]. On the other hand, low-bandwidth PLLs may cause stability issues, in particular in heavily-loaded microgrids, as shown in Section 5. In addition, low voltages can affect the PLL-based synchronization strategies in Voltage Source Converters (VSCs), since in this case, the PLL may fail to properly detect zero crossings of network voltages (e.g., [65]).

3.5 Large vs. Small Disturbance

In the context of microgrids, large disturbances include short-circuits, unplanned transitions from grid-connected to islanded mode of operation, and loss of generation units. Large disturbances can result in large frequency and voltage excursions and power swings among multiple DERs [66]. Such problems can be due to various reasons, such as a critical system mode being pushed to the unstable region by the fault, causing undamped oscillations in the system; similar behavior is observed during the unintentional islanding of a grid-connected microgrid [6]. Hence, proper power coordination among DERs and the response time of their controllers is critically important for retaining the stability of the system [6], [66]. In terms of the time-frame, stability issues due to large disturbances in microgrids can be classified as short-term phenomena, i.e., in the order of a few seconds.

It is important to note that planned islanding results in much less significant voltage and frequency excursions, since the DERs set-points are calculated and adjusted accordingly prior to islanding. When this transition takes place, one of the DERs in the island should be running in frequency-regulating/load-following/grid-forming mode. The time delay involved in this event, which may take a few cycles, adds to the complexity of maintaining microgrid stability. This is particularly an issue when the islanding is unplanned, microgrid has no or little inertia, and the exchanged power with the utility prior to disconnection is large (e.g., 50% of the local microgrid demand). In this case, over- or under-voltages may appear within a few cycles that could trip the inverters safety, resulting in the islanded microgrid becoming rapidly unstable.

As in bulk power systems, in microgrids, a disturbance is considered small if a linearized set of equations can adequately represent the system behavior [19], [55]. In this context, small-perturbation stability dominantly pertains to sustained oscillations arising from low-damped critical eigenvalues following a small disturbance. Depending on the root cause, small-perturbation instability can be either a short-term or a long-term phenomenon. For example, poor coordination of power sharing schemes among multiple DERs can yield undamped power oscillations growing quickly beyond acceptable operating ranges in the short term. On the other hand, heavily loaded microgrids in the long term, may show undamped oscillations with small load changes.

3.6 Summary

As previously mentioned, in microgrids, due to system characteristics such as feeder length and R/X ratios, a strong coupling exists between various system variables such as active and reactive power flows, as well as voltage and frequency. In particular, such a coupling is evident under stressed conditions associated with system instability issues. Hence, it is important to properly identify the major root causes of the instability problem, which based

on the discussion provided in previous sections, are summarized in Table 1, describing the way that each type of instability may manifest itself in the system.

TABLE 1. Characteristics of Various Types of Stability Issues in Microgrids

Category	**Control System Stability**		**Power Supply and Balance Stability**	
Subcategory	***Electric Machine Stability***	***Converter Stability***	***Voltage Stability***	***Frequency Stability***
Root Cause	Poor controller tuning.	Poor controller tuning, PLL bandwidth, PLL synchronization failure, harmonic instability.	DERs power limits, inadequate reactive power supply, poor reactive power sharing, load voltage sensitivities, dc link capacitor.	DERs active power limits, inadequate active power supply, poor active power sharing.
Manifestation	Undamped oscillations, aperiodic voltage and/or frequency increase/decrease.	Undamped oscillations, low steady-state voltages, high frequency oscillations.	Low steady-state voltages, large power swings, high dc-link voltage ripples.	High rate of change of frequency, low steady-state frequency, large power and frequency swings.

4. MODELING AND ANALYSIS

Despite the relatively small size, a typical microgrid consists of diverse components and technologies, including synchronous machines, inverter-based DERs, and various types of loads. In addition, the coordination among multiple assets in microgrids is critical, considering the strong interdependency and proximity among the various components in these systems. Therefore, microgrids design, control, and analysis require accurate models that adequately reflect their real performance, particularly for stability studies.

Generally, microgrid components can be divided in three main categories: DERs, the network, and loads. This section provides a discussion about each of these categories, providing details of their modeling and the techniques and tools used for stability studies.

4.1 DERs

DERs include generation and storage units, including renewable and non-renewable resources such as diesel engines, solar PV units, wind turbines, batteries, etc. A majority of DERs in microgrids are connected to the system via inverters; thus, the focus of this

section is on the modeling of the most commonly found inverter-based DERs. Modeling of non-inverter-based DERs, such as synchronous and induction machines, has been extensively discussed in the classical power system literature [55], and is only briefly discussed here.

4.1.1 Diesel and Hydro Gensets:

In microgrids, diesel generators [67] and/or hydro generators [68] are still an important source of power (e.g., [10]). Diesel generators are composed of a diesel engine (the prime mover), speed governor, synchronous machine, and a voltage regulator; in case of hydro systems, a hydraulic turbine is the prime mover rather than the diesel engine. The synchronous generator should be modeled in detail using higher-order machine models [55], since reduced-order machine models do not properly represent the generator under the unbalanced conditions typically found in microgrids.

The frequency and voltage of the synchronous machine are controlled by the speed governor and the voltage regulator, respectively. Voltage regulators have a voltage sensor that is used to measure the output voltage of the synchronous machine; this voltage is compared to a reference value and the error signal is used to change the field winding current in order to regulate the magnitude of the output voltage of the synchronous machine. The model for an AVR may consist of a single-phase thyristor rectifier, which is modeled as a first order system, and is typically controlled by a Proportional-Integral (PI) controller [55], [69]. The model equations are:

$$\frac{dz_v}{dt} = K_i^v(V_T^* - V_T) \tag{1}$$

$$u_v = z_v + K_p^v(V_T^* - V_T) \tag{2}$$

$$\tau_r \frac{dv_f}{dt} = -v_f + K_r u_v \tag{3}$$

Where V_T is the measured terminal voltage, V_T^* is the terminal voltage reference, z_v is the integrator state, u_v is the output of the controller, and v_f is the output voltage of the AVR rectifier. The parameters K_p^v and K_i^v are the proportional and the integral control gains, respectively. The time constant is τ_r and the gain of the AVR rectifier is K_r.

Speed governors are responsible for regulating the speed of the diesel engine by controlling the fuel injection. In the case of hydro systems, the governor would control the opening of the valves to control the flow of water into the turbines. The speed governor may be modeled as a PI controller with a droop function implemented with the feedback of the controller output, which is limited to the range (0, 1) to represent the operating stroke of the actuator [69], as follows:

$$\frac{dz_\omega}{dt} = \frac{K_i^\omega}{1 + K_p^\omega K_{dr}}\left(-K_{dr} z_\omega + (\omega_r^* - \omega_r)\right) \tag{4}$$

$$u_\omega = \frac{K_i^\omega}{1 + K_p^\omega K_{dr}}\left(z_\omega + K_p^\omega(\omega_r^* - \omega_r)\right) \tag{5}$$

where ω_r^* is the speed reference, z_ω is the integrator state, and u_ω is the output of the controller. The proportional control gain is K_p^ω and the integral control gain is K_i^ω. The speed droop gain is K_{dr} and is defined as $K_{dr} = R_{dr}\omega_0$, where R_{dr} is the static droop slope and ω_0 is the nominal speed of the prime mover in rad/s.

4.1.2 Power Electronic Systems

Microgrids consist of a wide array of power electronic systems like dc-dc converters, dc-ac converters, etc. These systems contain switching devices in addition to other passive components, which introduces complexity in modeling the power electronic converters [70]. Different modeling techniques are available for these converters depending upon the application, with detailed models being used for accurate time-domain, Electro-Magnetic Transient (EMT) simulation of the converters.

Average models, which neglect the switching are often employed for control system design [71], using simplified models obtained from averaging techniques [32]. Specifically, state-space averaging is used to obtain the dc and small-perturbation transfer functions of the power electronic system [72]. To reduce computational burden, these models can be used in cases where a system level simulation is required [32], [73]–[77].

The switching in power electronic systems implies that these models are non-linear, time-varying systems [78], where two or more sets of differential equations are required to represent the dynamics of the converters at different switching instances. Switching models are valuable for functional simulation of power electronic systems. The high switching frequencies in power electronic systems require small time-steps (in the range of microseconds) to numerically solve detailed models, leading to long simulation times and computational complexity. Furthermore, convergence of the differential equations can also be an issue when performing simulations using these models [79].

Power electronic converters, particularly inverters, can be of two kinds: voltage source or current source. As their names indicate, a Voltage Source Converter (VSC) and a Current Source Converter (CSC) employ a stiff voltage source (e.g., a capacitor) and a stiff current source (e.g., an inductor) at the dc side of the converter, respectively. The two kinds of converters have been shown to have advantages and drawbacks, depending on the application [80], [81]. Despite the topological differences between the converters (e.g., the need for a particular filter or an additional dc/dc stage [82]), and regardless of the converter

application, both can be controlled in either current control or voltage control mode, with single or multiple control loops [83]. However, VSC can control both active and reactive power in the AC side, while in CSC the reactive power is coupled with the active power. Most inverter-interfaced equipment is currently based on VSCs rather than CSCs, and hence the rest of these section discusses VSCs.

An inverter-based DERs can be modeled as an ideal dc-link VSC, as shown in Fig. 2, where the converter is divided into the physical inverter and ac filter, and the measurement and control components. Based on the DER type and the role it plays in a microgrid, three control strategies can be adopted by the control scheme [84], namely grid-forming, grid-supporting, and grid-feeding.

In the grid-forming mode, the VSC acts as a master control in the microgrid, providing voltage magnitude and frequency for the system. In Fig. 2, with the controls in State 1, the VSC operates in grid-forming mode. In grid-feeding mode, the VSC injects or absorbs constant active and reactive power to the grid, thus the controls are in State 2 in Fig. 2. In grid-supporting mode, the VSC injected/absorbed active and reactive powers change to minimize the voltage and frequency variations in the system; hence, in this case, there is an extra layer of control not shown in Fig. 2 that calculates and adjusts suitable power set-points P_{ref} and Q_{ref}.

The control of VSC is classically performed in Park's dq-axes reference frame [85]. Thus, in the grid-forming mode, the voltage dq-axes reference set-points would be directly used to create the abc-reference signals, as shown in Fig. 3. The reference angle is obtained by integrating the reference angular frequency. Observe that a PI controller is used to maintain the PCC voltage at its rated value.

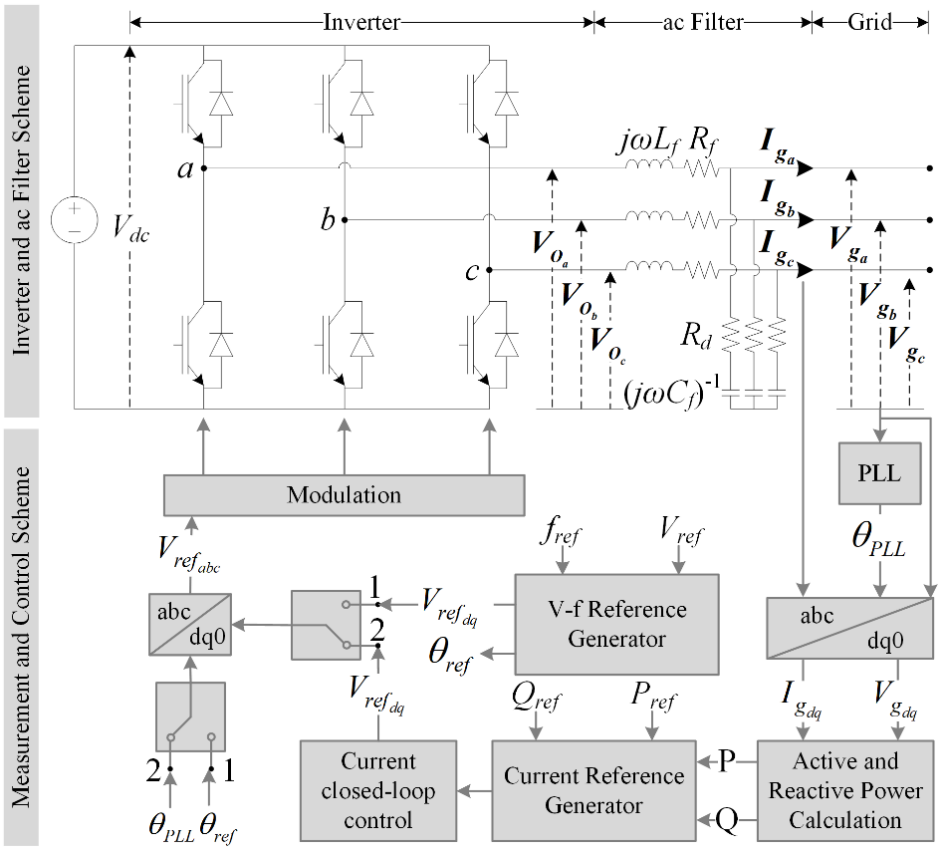

Fig. 2. VSC components, where phasors are shown in boldface font, as in the rest of the document.

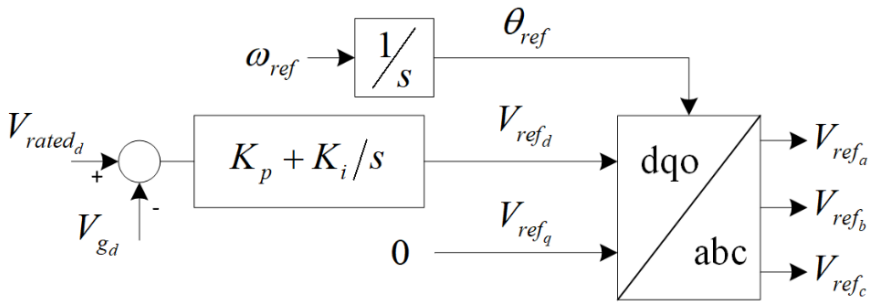

Fig. 3. Grid-forming voltage and phase reference generator.

In the grid-feeding control mode, the instantaneous injected active and reactive power for the VSC depicted in Fig. 2 are calculated first, as follows:

$$p = \frac{3}{2}\left(V_{g_d} I_{g_d} + V_{g_q} I_{g_q}\right) \tag{6}$$

$$q = \frac{3}{2}\left(V_{g_d} I_{g_q} - V_{g_q} I_{g_d}\right) \tag{7}$$

To obtain the corresponding fundamental P and Q components, the instantaneous active p and reactive q powers are passed through low-pass filters. The fundamental active and reactive powers are then passed through the current reference generator block to obtain the current dq-axes reference set-points, as follows:

$$I_{refd} = \frac{2}{3}\frac{P_{ref} V_{g_d} + Q_{ref} V_{g_q}}{V_{g_d}^2 + V_{g_q}^2} \tag{8}$$

$$I_{refq} = \frac{2}{3}\frac{P_{ref} V_{g_q} - Q_{ref} V_{g_d}}{V_{g_d}^2 + V_{g_q}^2} \tag{9}$$

These current references are then passed through the current closed-loop control to obtain the final voltage dq-axes references; feed-forward terms should be used to decouple the two axes, considering the difference between the voltages after and before the ac filter. Neglecting R_d in Fig. 2, a single line diagram can be used to derive such a relation, as shown in Fig. 4, resulting in the following equations:

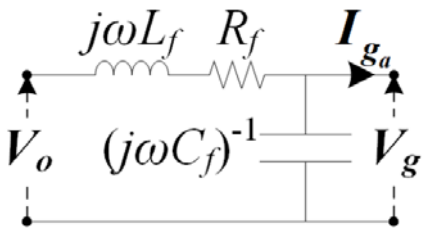

Fig. 4. Single-line diagram of ac filter, with phasors in boldface font.

$$V_{od} = V_{g_d}\left(1 - \omega^2 L_f C_f\right) + I_{g_d} R_f - I_{g_q} \omega L_f - V_{g_q} \omega R_f C_f \tag{10}$$

$$V_{oq} = V_{g_q}\left(1 - \omega^2 L_f C_f\right) + I_{g_q} R_f + I_{g_d} \omega L_f + V_{g_q} \omega R_f C_f \tag{11}$$

The final current closed-loop control block shown in Fig. 5 can be obtained from these equations. The output of the current controller are the voltage references $V_{\mathrm{ref}d}$ and $V_{\mathrm{ref}q}$, which are transformed back to the abc-reference frame to obtain the sinusoidal control

signals for the Pulse Width Modulation (PWM) control scheme of the converter. More information on alternative converter controls can be found in [86], [87].

To decrease the model complexity and reduce the computational burden, average models have been proposed that eliminate the power electronic switches (e.g., [88]), as shown in Fig. 6. In this case, the control system for the VSC is the same, and the only change is that abc-reference signals are directly fed to the ideal voltage sources, and PWM controls are eliminated.

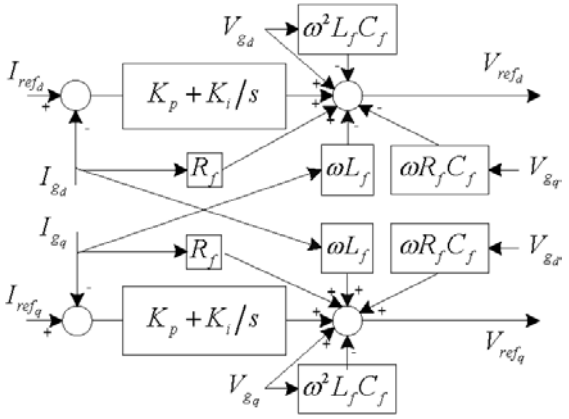

Fig. 5. Current closed-loop control.

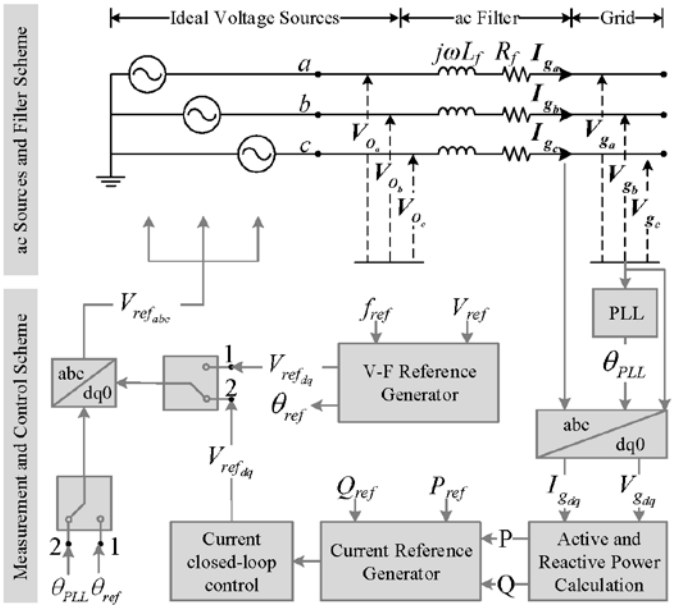

Fig. 6. VSC average model, with phasors in boldface font.

4.1.3 Wind Generators

These generators can be fixed speed or variable speed. Fixed speed technologies have low efficiency and low power quality; thus, variable speed generators have become the favored technology nowadays. Two popular variable speed wind generator technologies are Permanent Magnet Synchronous Generator (PMSG), also known as Type-4 generator, and Doubly Fed Induction Generator (DFIG) systems.

DFIG turbines use power electronic converters in the rotor, and maximize the power extraction from wind by operating in both sub- and super-synchronous speeds, allowing the turbine to operate at optimum tip-speed ratio. Fig. 7 shows the connection of the DFIG turbine to an electric system, where GSC is the grid side converter and RSC stands for rotor side converter. The dynamic equations governing the electromechanical and electrical components of a DFIG turbine can be found in [89].

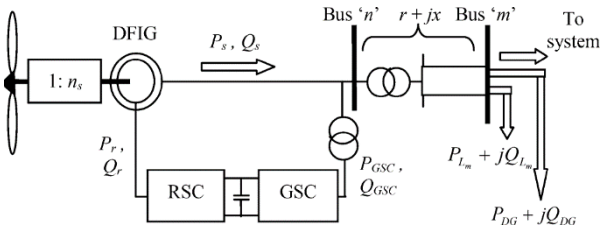

Fig. 7. DFIG wind turbine connection to grid.

A Type-4 wind generator model consists of grid-side converter controls (outer power and voltage control, inner current control), PLL, dc-link dynamics, machine-side converter controls and PMSG dynamics. For microgrid studies that are concerned with dynamics in the bandwidth of 0 to 10 Hz, the dc-link dynamics, machine-side converter controls, and machine dynamics can be ignored. Such practice was adopted by Vestas in a power system dynamic study related to wind in [90]; similar assumption can be found in [91] for Type-3 wind generator modeling in weak grids.

In [92], the authors give a simplified model of Type-4 wind where wind is treated as a current source with the current feedback control, converter RF filter dynamics, and PLL all aggregated as a first-order delay unit. If the microgrid dynamics are also modeled in a dq-frame, denoted as the grid dq-frame, then the entire system model will be suitable for small-perturbation analysis.

The modeling block diagram of a Type-4 generator in a microgrid is shown in Fig. 8, where the wind generator is treated as a voltage source that interfaces with the microgrid. The dq-axis voltages of the converter are all based on the PCC voltage, and are converted to the

grid dq-frame using the angle θ measured by the PLL, using the second-order PLL shown in Fig. 9. After the abc/dq block with θ as the input angle, the PCC voltage is in the converter dq-frame, as follows:

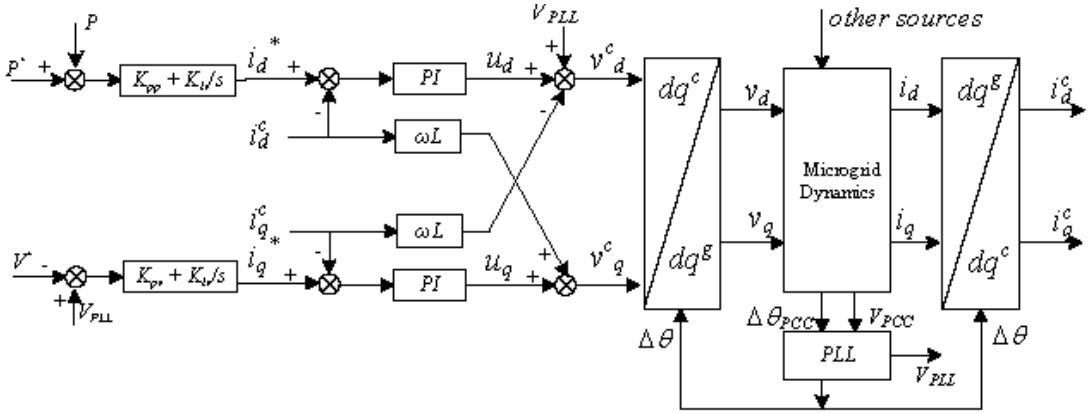

Fig. 8. Type-4 wind turbine modeling in a microgrid.

$$V_{\mathrm{PCC}}\angle(\theta_{\mathrm{PCC}}-\theta)=V_{\mathrm{PCC}}\angle(\Delta\theta_{\mathrm{PCC}}-\Delta\theta)=\left(v^{c}_{\mathrm{PCC},d}+jv^{c}_{\mathrm{PCC},q}\right) \tag{12}$$

where $\Delta\theta_{\mathrm{PCC}}=\theta_{\mathrm{PCC}}-\omega_0 t$ and V_{PCC} is the magnitude of the PCC voltage. The dq components are then:

$$\begin{aligned} V_{\mathrm{PLL}}=v^{c}_{\mathrm{PCC},d}&=V_{\mathrm{PCC}}\cos(\Delta\theta_{\mathrm{PCC}}-\Delta\theta)\\ v^{c}_{\mathrm{PCC},q}&=V_{\mathrm{PCC}}\sin(\Delta\theta_{\mathrm{PCC}}-\Delta\theta)\end{aligned} \tag{13}$$

with $v^{c}_{\mathrm{PCC},q}$ being fed into a PI control block to generate the frequency deviation $\Delta\omega$, which yields $\Delta\theta$ by integration.

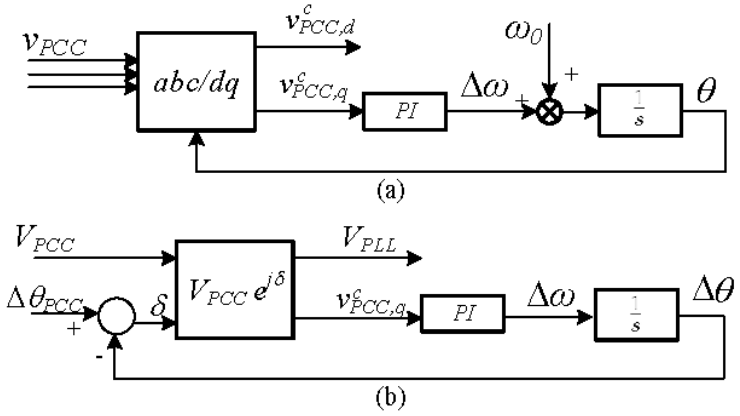

Fig. 9. Block diagrams of a PLL. (a) Original PLL, (b) PLL in dq-frames.

4.1.4 Batteries

A battery BESS model includes the battery and its buck/boost converter, as shown in Fig. 10 [93]. The rest of the BESS includes the dc/ac inverter and the ac filter, shown in Fig. 2. The dc-link voltage of the VSC is not ideal in this case, with the buck/boost converter being in charge of maintaining the dc-link voltage.

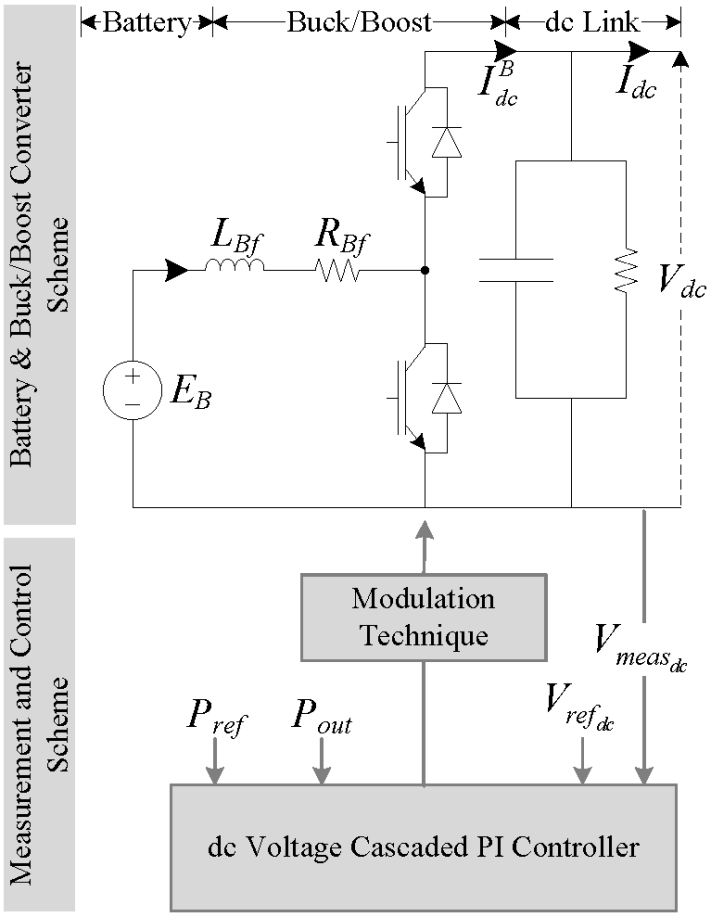

Fig. 10. Schematic of a battery circuit modeling.

Generally, for microgrid stability studies, E_B can be considered fixed, since the impact of the battery State-of-Charge (SOC) on the dc voltage dynamics is not as significant for stability studies, given its relatively slow dynamic response. However, the battery's performance close to its SOC lower limit, in particular pertaining to dc-link voltage stability, may require an accurate model reflecting the relation between the SOC and the dc voltage dynamics.

The battery's dc voltage dynamics as a function of the dc current can be modelled with the circuit shown in Fig. 11, which is composed of Two *RC* Time Constants (TTC), and is able to account for slow and fast electrochemical processes, R_1 and C_1 representing the fastest, and R_2 and C_2 the slowest BESS charge diffusion dynamics [94]. When considering voltage and current measurements sampled at resolution smaller than 10 seconds, an additional state is generally required to capture all the dynamics. R_0 is the Equivalent Series Resistance (ESR) and E_m is the electromotive force of the cell defined as the voltage across the BESS terminals without any connected load/generator connected and after the charge redistribution. All the TTC parameters are nonlinear and are a function of the cell SOC/energy.

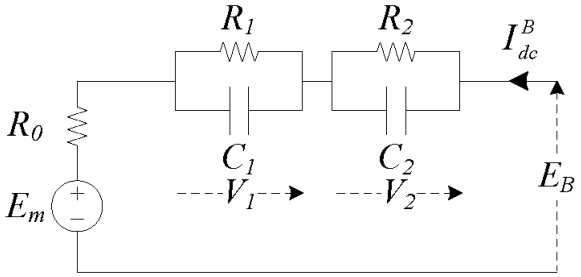

Fig. 11. Battery TTC model.

The SOC of a battery is defined as the difference between the initial battery capacity and the provided charge, in per-unit of the charge that the battery would nominally provide with respect to a constant discharge rate. Several models have been proposed in the literature (e.g. [95]-[98]), which are based on the following five basic criteria: (1) measurement of electrolyte specific gravity, (2) battery current time-integration, (3) battery impedance/resistance estimation, (4) measurement of the battery open circuit voltage, and (5) models that take into account the electrolyte temperature, discharge rate and other battery parameters. Additionally, an accurate estimation of the SOC needs to take into account the battery environmental conditions, with particular reference to its temperature, as well as the battery behaviour at different discharge rates and its life cycle. As discussed in [99], a combination of methods 2, 4 and 5 is summarized by the following general equation:

$$\mathrm{SOC}(t) = \frac{C(t_0) - \alpha(I,\theta)\int_{t_0}^{t} I_{dc}^{B}(t)dt}{C(I,\theta)} \tag{14}$$

where $C(I,\theta)$ is the battery capacity for a constant current discharge rate I at electrolyte temperature θ, $C(t_0)$ is the battery capacity at time t_0, $I_{dc}^{B}(t)$ is the instantaneous value of the battery current (both charge/discharge), and α is the efficiency coefficient associated to battery charge and discharge (a first approximation is $\alpha=1$).

The initial battery capacity, with null battery current output maintained for few hours, is based on the well-known correlation between battery open circuit voltage and electrolyte density (this relation is known for any type of battery electrochemistry), assuming appropriate use and maintenance of the battery. Fig. 12(a) shows this correlation for the 100 Ah - 48 V lead-acid battery storage system (at 20° C reference temperature). It is worth noting that the initial battery capacity takes into account the battery temperature by means of linear approximation described below, and adopted to correct the battery SOC during the battery charge/discharge cycles.

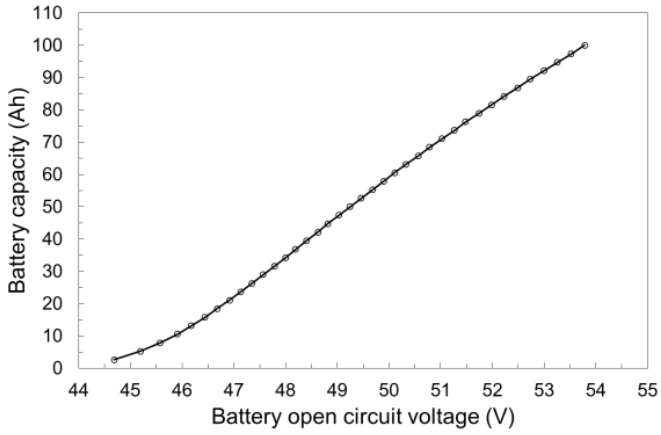

(a)

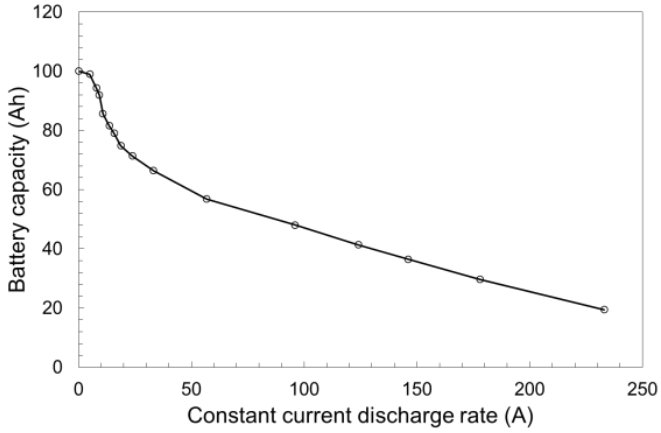

(b)

Fig. 12. (a) Initial battery capacity versus open circuit voltage, and (b) battery capacity as a function of different constant current discharge rates for a 100 Ah lead-acid battery at 20 °C.

Reliable SOC estimation requires a suitable procedure to compute (14) for the case of non-constant charge/discharge rates. In particular, assuming an array of values $C(I^*) = [C(I_0^*), \dots, C(I_k^*), \dots, C(I_n^*)]$ can be used that defines the battery capacities at various constant discharge rates I_k^* at a fixed temperature θ^*. These data are typically provided by the battery manufacturer as shown, for instance, in Fig. 12(b); alternatively, they can be determined by means of specific tests. The SOC estimator may calculate the average charge/discharge battery current $\tilde{I}_T^{fs}$ within a specific time window T by averaging the measured battery current I_{dc}^B sampled at given frequency *fs* (e.g., *fs* = 5 Hz, and T = 2 s). Assuming that the SOC value has been already estimated at time $T - \Delta t$, and considering that $\tilde{I}_T^{fs} \in [I_k^*, I_{k+1}^*]$, where I_k^* indicates various constant discharge rates at a fixed temperature θ^* used to define the array $C(I^*)$, is calculated within $[t - \Delta t, t]$ for $\Delta t = 1/fs$ (e.g., Δt = 200ms); then, (14) can be written as:

$$\mathrm{SOC}(t) = \frac{C(t - \Delta t) - \left(\tilde{I}_T^{fs}(t - \Delta t) + \tilde{I}_T^{fs}(t)\right)\frac{\Delta t}{2}}{C(\tilde{I}_T^{fs}, \theta)} \tag{15}$$

where:

$$C\left(\tilde{I}_T^{fs}, \theta\right) = \frac{C(I_k^*) + C(I_{k+1}^*)}{2} \tag{16}$$

The averaging of the charge/discharge battery current over a sufficient large time window T allows to consider an equivalent constant discharge ratio $\tilde{I}_T^{fs}$, for which the application of (14) can be assumed still valid. A discontinuity in the SOC estimation could take place when the calculated average charge/discharge battery current $\tilde{I}_T^{fs}$ switches from a discharge rate interval to a different one, i.e., when, at time t, $\tilde{I}_T^{fs} \in \left[I_j^*, I_{j+1}^*\right]$, for $j \neq k$ in (16). In order to avoid such a discontinuity in the SOC estimation, the value of battery capacity $C(t - \Delta t)$ in (15) is calculated as the product between the rated battery capacity associated with the new equivalent discharge rate $\tilde{I}_T^{fs}$ and the SOC value estimated at $t - \Delta t$, namely:

$$C(t - \Delta t) = C\left(\tilde{I}_T^{fs}, \theta\right)\mathrm{SOC}(t - \Delta T) \tag{17}$$

The rated capacity $C(\tilde{I}_T^{fs}, \theta)$ in (15) and (17) takes into account the capacity drift with the temperature as per the linear approximation:

$$\mathrm{C}(\tilde{I}_T^{fs}, \theta) = C(\tilde{I}_T^{fs}, \theta^*)(1 + \beta(\theta - \theta^*)) \tag{18}$$

For example, for a lead-acid battery, the coefficient β is in the order of 0.006 Ah/°C, and is in general known by the battery manufacturer for θ^* = 20 °C.

From the TTC equivalent circuit shown in Fig. 11, it is possible to derive a state space model expressed as a function of two state variables $x = [V_1 \ V_2]^T$, with I_{dc}^B as the only input and E_B as the only output, as follows:

$$\begin{aligned} \dot{V}_1 &= \frac{-1}{R_1 C_1} V_1 + \frac{1}{C_1} I_{dc}^B \\ \dot{V}_2 &= \frac{-1}{R_2 C_2} V_2 + \frac{1}{C_2} I_{dc}^B \\ E_B &= V_1 + V_2 + R_0 I_{dc}^B + E_m \end{aligned} \tag{19}$$

$$\begin{aligned} \dot{x} &= \boldsymbol{A}x + \boldsymbol{B}u \\ E_B &= \boldsymbol{C}x + \boldsymbol{D}u \end{aligned} \tag{20}$$

$$\boldsymbol{A} = \begin{bmatrix} \frac{-1}{R_{1C_1}} & 0 \\ 0 & \frac{-1}{R_2 C_2} \end{bmatrix} \qquad \boldsymbol{B} = \begin{bmatrix} \frac{1}{C_1} & 0 \\ \frac{1}{C_2} & 0 \end{bmatrix}$$
$$\boldsymbol{C} = [1 \quad 1] \qquad \boldsymbol{D} = [R_0 \quad E_m]$$
$$u = [I_{dc}^B \quad 1]^T \tag{21}$$

It is assumed here that the energy flow is positive during the charge and negative during the cell discharge. All the cell parameters depend on the SOC as well as on the rate of the discharge current (C-rate). For this reason, matrices A and B need to be experimentally fitted for different SOCs.

By using $I_{dc}^B = P_{dc}^B / E_b$ to express the battery current as a function of the battery power P_{dc}^B in the state space formulation, the battery voltage can be defined as follows:

$$E_B(t) = \frac{\boldsymbol{C}x(t) + E_m \pm \sqrt{(\boldsymbol{C}x(t) + E_m)^2 + 4R_0 P_{dc}^B(t)}}{2} \tag{22}$$

It is shown in [100] that for a unique value of P_{dc}^B, there is one and only one feasible solution for E_B in (22). More information on active power limits, dc voltage limits, and SOC limits can also be found in [94].

The practical use of a TTC model requires the knowledge of the two state components, which are a modelling abstraction and not directly measurable. Hence, a Kalman-based state estimation approach can be used to estimate the model's state vector as a function of battery terminal voltage measurements, and the structure of the state space matrices [101].

The buck/boost converter in Fig. 10 is in charge of controlling the dc link capacitor voltage by properly charging and discharging the battery. A PI controller can be used to generate

the duty cycle for the switches based on the difference of the dc link voltage and its set-point. Thus, when the dc link voltage is lower than the pre-defined set-point, the converter works in the boost mode, discharging the battery. When the dc link voltage is higher than the set-point, the converter operates in the buck mode, charging the battery. Note that since the average converter model is non-linear, particular attention is needed on the design of the controller. Hence, a more sophisticated control approach may be necessary for accurate stability studies, considering the fact that the two modes of operation (buck or boost) have different transfer functions; in particular, the point of control transition between these two modes deserves special attention.

4.1.5 Solar PV

A PhotoVoltaic (PV) cell is a semiconductor that, by using the PV effect, converts solar energy into electricity in the form of a direct current. A simplified circuit model of a single PV cell is shown in Fig. 13, where I_p represents the photogenerated current, I_D is the p-n junction (diode) dark current, and R_s and R_{sh} are the series and shunt equivalent resistances, with the output current and voltage being expressed as follows:

$$\begin{aligned} I_L &= I_p - I_D - \frac{V}{R_{sh}} \\ V_L &= V - R_s I_L \end{aligned} \tag{23}$$

where the diode characteristic is given by:

$$I_d = I_0 \left[e^{\frac{qV}{kT}} - 1 \right] \tag{24}$$

with I_0 representing the saturation current, q the elementary charge, k the Boltzmann constant, and T the absolute temperature. The I-V characteristic at the cell's terminals depends, among other parameters, on the irradiance level and temperature. The particular case of the impact of varying irradiance on the I-V curves is shown in Fig. 14, where the starred point on each curve indicates the Maximum Power Point (MPP), which varies with the operating conditions of the cell (e.g., temperature and irradiance). A solar PV module is built by connecting PV cells in series and/or parallel; the effect on the I-V curves is a scaling of the voltage magnitude and/or current magnitude, respectively. The I-V characteristic of a PV module, retains its shape and the relative location of the MPP.

To ensure maximum power transfer from the PV module, a Maximum Power Point Tracker (MPPT) system is employed. MPPT algorithms are widely covered in [101], [102]. The MPPT is usually part of a dc/dc converter in standalone applications (e.g., battery charging), and part of the dc/ac inverter in grid-tied applications. Voltage and current matching may require a dc/dc buck-boost converter in the grid-tied case. MPPTs are

particularly important in places where irradiance varies widely (e.g., cloud effect) and under partial shading of PV modules, which distorts the I-V characteristic [103].

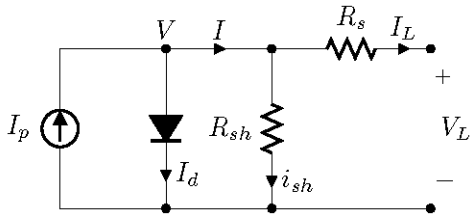

Fig. 13. Simplified PV cell model.

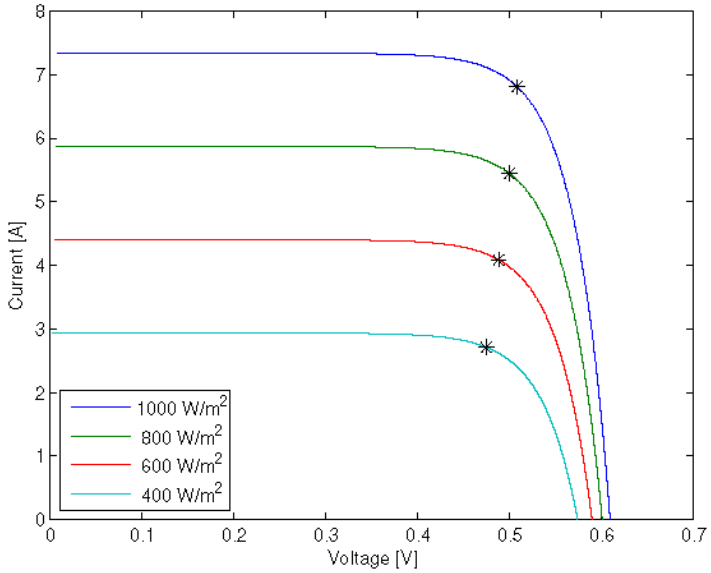

Fig. 14. Sample I-V curves for a solar cell with varying irradiance.

4.1.6 Flywheel Energy Storage System (FESS)

The FESS model presented here comprises an induction machine, a flywheel represented as a high inertia mass constant (*H*), two bi-directional VSCs, and all required controls, as shown in Fig. 15. The VSCs are full-bridge, self-commutated three-phase converters, as shown in Fig. 2. The dc buses of the VSC units are connected through a dc link with a capacitor. For charging conditions, the network-side VSC in Fig. 15 is assumed to be a rectifier, and the flywheel-side VSC is treated as an inverter. The machine in Fig. 15 is typically squirrel cage induction motor/generator, depending on the FESS charging/discharging mode, with a high inertia *H* representing the flywheel.

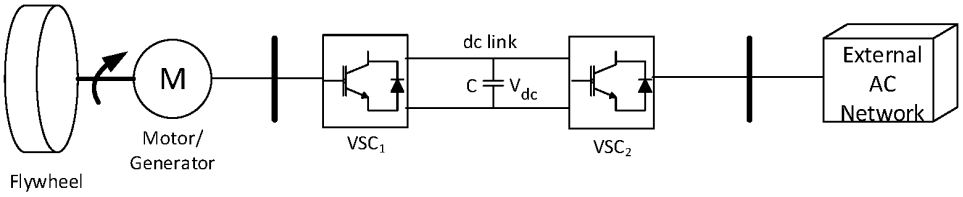

Fig. 15. FESS Configuration.

The network-side VSC maintains the dc link voltage constant at a reference value [104]. Fig. 16 illustrates the control structure of the VSC, which controls the dc link voltage and the network ac voltage. On the other hand, the active power control depicted in Fig. 17 controls the flywheel-side VSC. Note that this control topology is similar to the network-side VSC controls, but instead of controlling the dc voltage, it controls the power injection to/from the flywheel; it also controls the ac voltage level of the FESS induction machine.

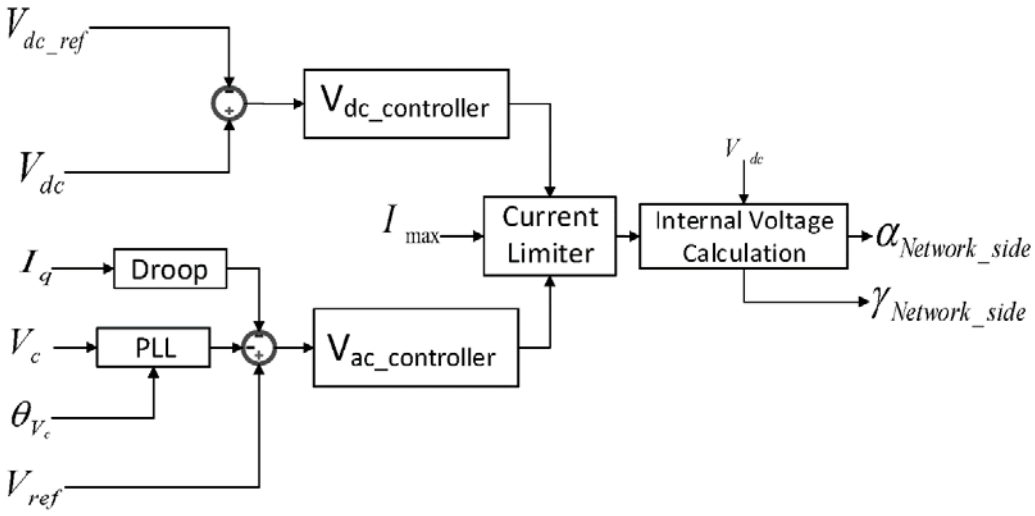

Fig. 16. Network side converter VSC.

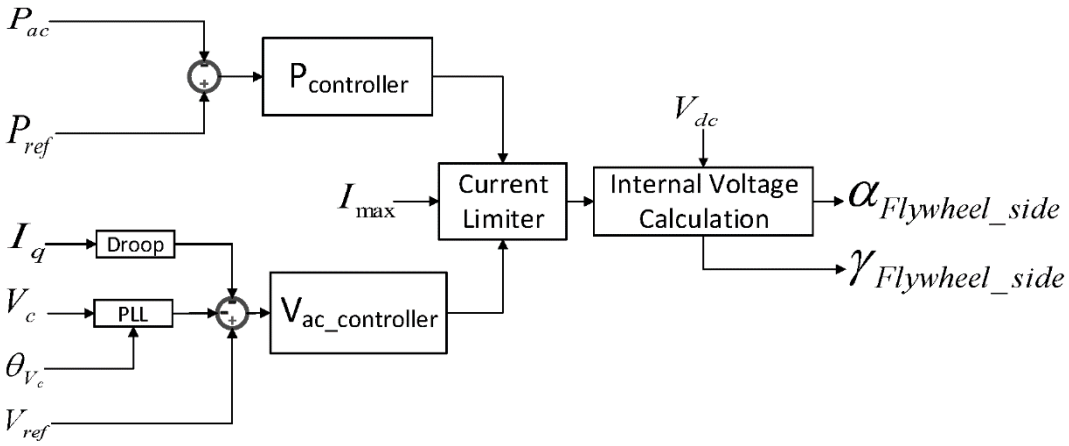

Fig. 17. Flywheel side converter VSC.

The power angle α and modulation ratio γ are the output signals of the VSCs' controls and determine the active and reactive power exchanged with the corresponding ac systems, as follows [105]:

$$P = \frac{V_{dc} V_c \gamma \sin(\alpha)}{X_c} \tag{25}$$

$$Q = \frac{V_{dc} V_c \gamma \cos(\alpha)}{X_c} - \frac{V_c^2}{X_c} \tag{26}$$

where V_{dc} is the converter dc voltage, V_c is the converter ac voltage, and X_c is the converter reactance.

The primary objective of the FESS is to regulate and control the system frequency, which can be accomplished with the control depicted in Fig. 18. This control determines the active power reference P_{ref} in Fig. 17, i.e., in the active power set-points of the flywheel-side VSC, to be injected to/from the FESS, responding to the frequency deviations detected at the terminal of the system. To prevent either the shortage or the surplus of energy stored in the FES, the rotor speed variation of the induction machine has to be constrained; hence, a speed limiter is needed, as shown in Fig. 18.

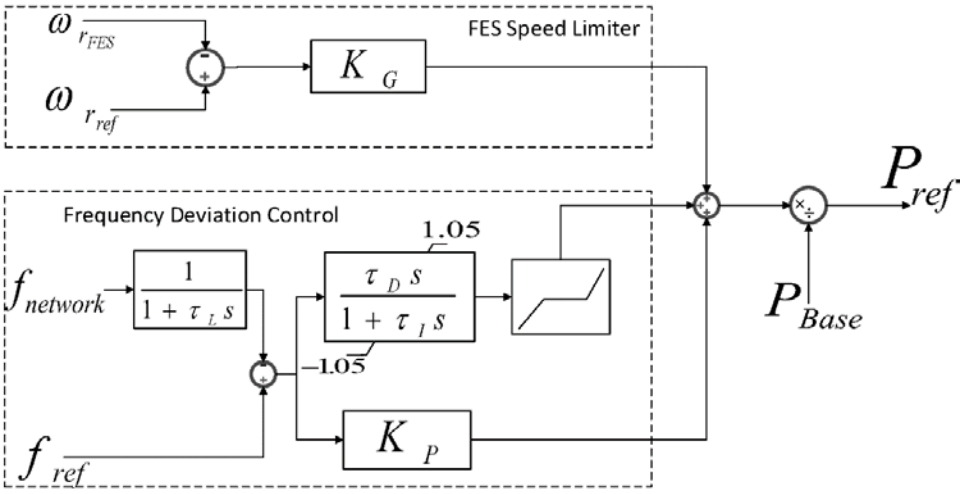

Fig. 18. FESS speed/frequency Control.

4.2 Network

For transmission lines modeling in bulk power systems, the system is considered balanced, i.e., the three-phase currents are balanced and the lines parameters are balanced by transposition. However, in distribution feeders, neither of these two fundamental assumptions are valid; thus, a modeling based on a three-phase grounded four-wire system is used herein [106]. A model of a three-phase distribution system with the neutral being grounded is shown in Fig. 19. Observe that the charging admittances are neglected since microgrid feeders are short and operate at medium/low voltage levels [106][1]. In this context, the following equations show the relation between the current through a feeder from node *i* to node *j*, and the voltage difference between these two nodes:

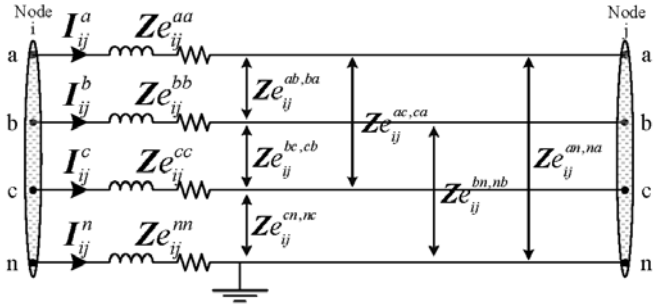

Fig. 19. Three-phase distribution feeder in a microgrid with grounded neutral.

[1] Note that this assumptions may not be valid for long feeders, where charging admittances can no longer be neglected.

$$\begin{bmatrix} \boldsymbol{V}_i^a - \boldsymbol{V}_j^a \\ \boldsymbol{V}_i^b - \boldsymbol{V}_j^b \\ \boldsymbol{V}_i^c - \boldsymbol{V}_j^c \end{bmatrix} = \begin{bmatrix} \boldsymbol{Z}_{ij}^{aa} & \boldsymbol{Z}_{ij}^{ab} & \boldsymbol{Z}_{ij}^{ac} \\ \boldsymbol{Z}_{ij}^{ba} & \boldsymbol{Z}_{ij}^{bb} & \boldsymbol{Z}_{ij}^{bc} \\ \boldsymbol{Z}_{ij}^{ca} & \boldsymbol{Z}_{ij}^{cb} & \boldsymbol{Z}_{ij}^{cc} \end{bmatrix} \begin{bmatrix} \boldsymbol{I}_{ij}^a \\ \boldsymbol{I}_{ij}^b \\ \boldsymbol{I}_{ij}^c \end{bmatrix} = Z_{ij}^{abc} \begin{bmatrix} \boldsymbol{I}_{ij}^a \\ \boldsymbol{I}_{ij}^b \\ \boldsymbol{I}_{ij}^c \end{bmatrix} \tag{27}$$

where the impedance matrix can be defined as follows:

$$\mathrm{Z}_{ij}^{abc} = \mathrm{Z}e_{ij}^{abc} - \mathrm{Z}e_{ij}^{\emptyset n}\mathrm{Z}e_{ij}^{n\emptyset}/Ze_{ij}^{nn} \tag{28}$$

where

$$\mathrm{Z}e_{ij}^{abc} = \begin{bmatrix} \boldsymbol{Z}e_{ij}^{aa} & \boldsymbol{Z}e_{ij}^{ab} & \boldsymbol{Z}e_{ij}^{ac} \\ \boldsymbol{Z}e_{ij}^{ba} & \boldsymbol{Z}e_{ij}^{bb} & \boldsymbol{Z}e_{ij}^{bc} \\ \boldsymbol{Z}e_{ij}^{ca} & \boldsymbol{Z}e_{ij}^{cb} & \boldsymbol{Z}e_{ij}^{cc} \end{bmatrix} \tag{29}$$

$$\mathrm{Z}e_{ij}^{\emptyset n} = \begin{bmatrix} \boldsymbol{Z}e_{ij}^{an} \\ \boldsymbol{Z}e_{ij}^{bn} \\ \boldsymbol{Z}e_{ij}^{cn} \end{bmatrix} \tag{30}$$

$$\mathrm{Z}e_{ij}^{n\emptyset} = \begin{bmatrix} \boldsymbol{Z}e_{ij}^{na} \\ \boldsymbol{Z}e_{ij}^{nb} \\ \boldsymbol{Z}e_{ij}^{nc} \end{bmatrix} \tag{31}$$

Single-phase microgrid feeders can be modeled by a resistance and an inductance connecting two nodes [106], as shown in Fig. 20, where the following equation models the current through a feeder connecting nodes *i* and *j*:

$$\boldsymbol{I}_{ij}^a = \frac{\boldsymbol{V}_i^a - \boldsymbol{V}_j^a}{\boldsymbol{Z}e_{ij}^{aa}} = \frac{\boldsymbol{V}_i^a - \boldsymbol{V}_j^a}{Ze_{ij}^{aa}\angle\theta_{ij}^{aa}} \tag{32}$$

Observe that if the single-phase current returns via a neutral wire, then the mutual impedance of the neutral current should also be considered.

Fig. 20. A single-phase distribution feeder in a microgrid, with phasors in boldface font.

The complex power flow from node *i* to node *j* in each phase ϕ is defined as follows:

$$P_{ij}^{\emptyset} - \mathbf{J}Q_{ij}^{\emptyset} = \boldsymbol{V}_i^{\emptyset^*}\boldsymbol{I}_{ij}^{\emptyset} \tag{33}$$

Substituting (27) into (33), the active and reactive power flows from node *i* to node *j*, in phase *a* are as follows:

$$P_{ij}^{a} = V_i^{a} \sum_{\emptyset=a,b,c} Y_{ij}^{a\emptyset}[V_i^{\emptyset}\cos\left(\theta_{ij}^{a\emptyset} + \delta_i^{\emptyset} - \delta_i^{a}\right) - V_j^{\emptyset}\cos\left(\theta_{ij}^{a\emptyset} + \delta_j^{\emptyset} - \delta_j^{a}\right)] \tag{34}$$

$$Q_{ij}^{a} = V_i^{a} \sum_{\emptyset=a,b,c} Y_{ij}^{a\emptyset}[V_i^{\emptyset}\sin\left(\theta_{ij}^{a\emptyset} + \delta_i^{\emptyset} - \delta_i^{a}\right) - V_j^{\emptyset}\sin\left(\theta_{ij}^{a\emptyset} + \delta_j^{\emptyset} - \delta_j^{a}\right)] \tag{35}$$

where $Y_{ij}^{a\emptyset}$ and $\theta_{ij}^{a\emptyset}$ are the magnitudes and angles of the elements of the matrix $Y_{ij}^{abc} = {Z_{ij}^{abc}}^{-1}$.

As seen in (34) and (35), the line impedance plays a significant role in determining the active and reactive power flows from node *i* to node *j*. Consider that for dominantly resistive lines, the active power flow is tightly linked to the voltage magnitudes.

Note that, in the context of network modeling, transformer saturation should be considered due to the associated inrush currents in microgrids, which are important for converter-based DERs, as these large currents could activate converter protections. Transformer models for inrush calculation considering saturation can be found in [107].

4.3 Load Models

4.3.1 Static Loads

Loads which display negligible dynamic response in a power system are typically modelled by the following equation [56]:

$$P_{\mathrm{L}} = P_{\mathrm{Lo}}\left(\frac{V_{\mathrm{L}}}{V_{\mathrm{Lo}}}\right)^{n_p} \tag{36}$$

which can be viewed equivalently as a ZIP load:

$$P_{\mathrm{L}} = P_{\mathrm{Lo}}\left[Z^p\left(\frac{V_{\mathrm{L}}}{V_{\mathrm{Lo}}}\right)^2 + I^p\left(\frac{V_{\mathrm{L}}}{V_{\mathrm{Lo}}}\right) + P^p\right] \tag{37}$$

$$n_p \approx \frac{2 \times Z^p + 1 \times I^p + 0 \times P^p}{Z^p + I^p + P^p} \tag{38}$$

And similarly for:

$$Q_{\mathrm{L}} = Q_{\mathrm{Lo}} \left(\frac{V_{\mathrm{L}}}{V_{\mathrm{Lo}}} \right)^{n_q} \tag{39}$$

$$Q_{\mathrm{L}} = Q_{\mathrm{Lo}} \left[Z^q \left(\frac{V_{\mathrm{L}}}{V_{\mathrm{Lo}}} \right)^2 + I^q \left(\frac{V_{\mathrm{L}}}{V_{\mathrm{Lo}}} \right) + P^q \right] \tag{40}$$

$$n_q \approx \frac{2 \times Z^q + 1 \times I^q + 0 \times P^q}{Z^q + I^q + P^q} \tag{41}$$

where P_{L} is the active power demand; Q_{L} is the reactive power demand; P_{Lo} is the rated active power, and Q_{Lo} is the rated reactive power at nominal operating voltage V_{Lo}; n_p and n_q are voltage indexes for the active power and reactive power respectively; and Z^p, I^p, and P^p are the constant impedance, constant current and constant power coefficients for P_{L}, and similarly Z^q, I^q, and P^q for Q_{L}.

As it can be seen from (36), the active power demand sensitivity to the operating voltage (*dP /dV*) is determined by n_p; thus, as n_p increases, the sensitivity of power consumption with respect to operating voltage also increases. In [108], a comprehensive study is carried out to model residential loads that shows an average n_p for existing residential load models in the range of 1.1 to 1.7. This value is demonstrated to be even higher in isolated microgrids, where the majority of the power is consumed by households for heating and lightning purposes [46].

4.3.2 Dynamic Loads

Different types of dynamic loads are connected to microgrids, of which Direct-on-Line (DOL) start induction motors, and Variable Speed-Drive (VSD) based motors are more common in residential/commercial and industrial/ship microgrids, respectively. The DOL start motor load represents induction motor loads which are directly connected to the microgrid, as in the case of residential appliances and Heating, Ventilation, and Air Conditioning (HVAC) systems in residential and commercial levels. These motor loads are modelled with induction motors with the associated load characteristics (e.g., fan, pump, compressors, etc.). In addition, for large motors, soft-starters can also be modeled at the front end of the induction motor to reduce the high starting motor currents, which would cause substantial reduction in microgrid voltage; it is recommended to install a soft-starter unit for three-phase induction motors rated more than 10 kW. A schematic of the DOL start motor load is shown in Fig. 21.

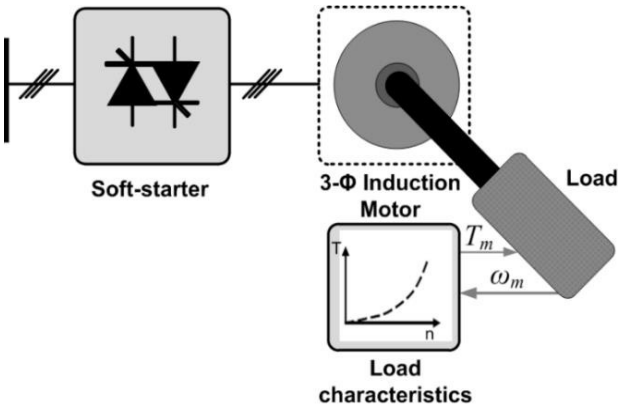

Fig. 21. DOL start motor load (soft-starter is usually needed for motors rated more than 10 kW).

The induction machine is the main component in the DOL motor model, and a number of assumptions and simplifications can be made in order to represent the motor in dynamic studies [55][2]. Thus, stator transients are ignored in the stator voltage equation, and the rotor currents are eliminated by representing a transient voltage E′ behind the stator transient impedance. In this case, the stator voltage V_s can be represented by:

$$V_s = (R_s + jX_s')I_s + E' \tag{42}$$

where R_s, X_s', and I_s denote stator resistance, stator transient reactance, and stator current respectively. The stator transient reactance X_s' is given by:

$$X_s' = \omega_s \left(L_{ss} - \frac{L_m^2}{L_{rr}} \right) \tag{43}$$

where L_{ss}, L_m, L_{rr}, and ω_s denote stator winding inductance, magnetising inductance, rotor winding inductance, and angular velocity of the stator field, respectively. The transient voltage E' is given by:

$$E' = \left(\frac{\omega_s L_m}{L_{rr}} \right) \psi_r \tag{44}$$

where ψ_r is the rotor flux linkage.

The rotor mechanical dynamics are represented by the following equations:

$$2H \frac{d\omega_r}{dt} = T_e - T_m \tag{45}$$

[2] More complex models can be found in [55].

where ω_r, H, T_e and T_m denote rotor angular velocity, combined inertia constant of the motor and load, electromagnetic torque and mechanical toque, respectively. The following mechanical load-torque T_m equation can be used to represent the typical load-torque characteristics of motor loads:

$$T_m = T_{\min} + \begin{cases} (T_s - T_{\min})\left(\dfrac{|\omega_m| - (1 - s_m)}{s_m}\right)^l \\ (T_o - T_{\min})\left(1 - \dfrac{|\omega_m|}{1 - s_m}\right)^n \end{cases} \quad (46)$$

where $T_{\min}$, T_s, T_0, ω_m, and s_m denote minimum torque, torque at synchronous speed, torque at standstill, angular velocity of the load in p.u., and slip at minimum torque, respectively. The parameters of the load-torque equation depend on the respective load characteristics, e.g., fan, compressor, etc.; sample parameters are illustrated in Table 2.

TABLE 2. Parameters of Various Types of Motor Connected Loads (in pu)

	T_{min}	T_s	T_0	S_m	l	n
Fan	0.0375	1	0.15	0.875	1.92	2.15
Centrifugal Compressor	0	0.775	0.0875	0.867	1.27	1.34
Pump	0.045	1	0.11	0.86	1.73	2.50
Centrifugal Pump	0.05	0.575	0.075	0.85	1.93	1.42

The soft-starter is modelled using two back-to-back thyristors, with the firing angle initially set to a high value to decrease the starting voltage of the induction motor, which would reduce the high starting current of the machine. Once the motor is started, the firing angle is linearly decreased to apply the nominal terminal voltage of the induction motor.

VSD motor loads are modelled using a three-phase controlled rectifier with an inbuilt transformer, a PWM inverter, and a three-phase induction motor with its mechanical load. In certain VSDs, simple three-phase diode-bridge rectifiers are used; however, controlled rectifiers allow maintaining a constant dc link voltage when the supply system voltage varies, thus improving the stability of VSD motor loads. The PWM inverter controls the supply frequency and the voltage for the three-phase induction motor while maintaining the *V/f* ratio constant, so that the air-gap flux remains constant. Similar to DOL start motor drives the load dynamics were represented by their respective load torque equations.

A schematic of the dynamic simulation model of VSD-driven motor load is shown in Fig. 22, where ω_{ref}, ω_m, L_f, C_d, f_m, and P_m denote the reference angular velocity, rotor angular

velocity (angular velocity of the load), dc-link inductor, dc-link capacitor, frequency, and modulation index, respectively. The front-end controlled rectifier of the VSD maintains the dc link voltage constant by varying the thyristor firing angle based on the measured ac voltage V_{ac}. The value of L_f is determined based on the allowable current ripple in the dc link, while C_d is determined by the allowable dc voltage ripple in the dc link [32]. The VSD controller, shown in Fig. 23, can soft-start the inductor motor and drive the load based on the speed reference ω_{ref}.

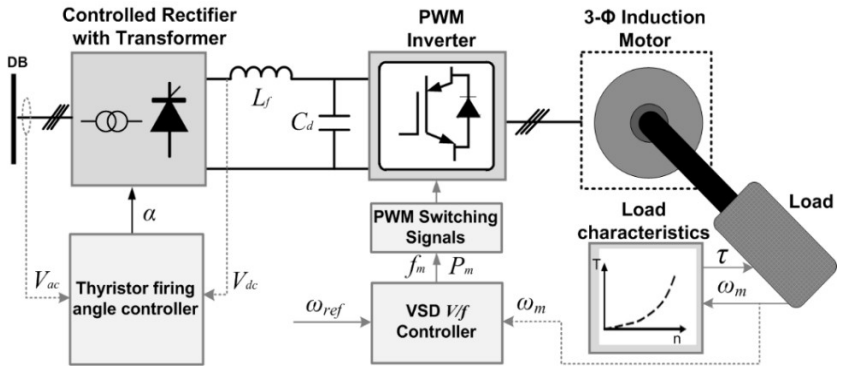

Fig. 22. Dynamic simulation model of the VSD-driven motor load.

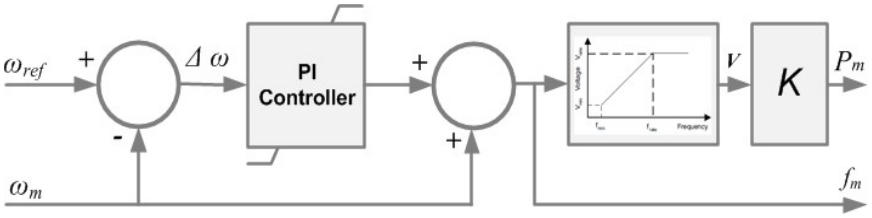

Fig. 23. VSD *V/f* Controller.

The VSD V/f controller compares the actual rotor speed ω_m of the induction motor with the speed reference ω_{ref}, and then the speed error $\Delta\omega$ is fed through the PI controller to generate the reference frequency f_m and modulation index P_m for the PWM, which drives the three-phase inverter. It must be noted that an average three-phase inverter model could be used for dynamic simulations.

4.4 Analysis Techniques and Tools

Stability studies start with the definition of the initial system conditions, typically computed using power flow techniques. These techniques allow to perform static studies such as the determination of voltage profiles in microgrids [31], [109].

4.4.1 Large-Perturbation Stability

Microgrids show highly non-linear dynamics [110], but microgrid stability studies have been typically based on small-perturbation linearization techniques [111]. Various bodies of work are demonstrating that small-perturbation stability might not give an accurate representation of stability in microgrids [112], [113]. The presence of power electronic converters and stochastic resources which can exhibit large dynamic changes makes the large-perturbation stability critical for microgrids.

When faults occur in an isolated/islanded microgrid, or a fault triggers an unintentional islanding of a microgrid, Critical Clearing Times (CCTs) can give a good idea of the relative stability. In [55], the CCT is defined as the maximum time between initiation and isolation of a fault such that the power system remains stable. Classical equal area criterion analysis is helpful in determining CCTs in transmission systems; however, in microgrids, this technique does not apply, as stability problems are not directly associated with synchronism problems among DERs, as discussed in Section 3.

Large-perturbation stability analysis in microgrids can be performed using two main approaches: Lyapunov-based stability studies [114]-[116], time-domain simulations carried out on accurate models of a microgrid [31], [6], and Hardware-in-the-Loop (HIL) approaches [117].

4.4.1.1 Lyapunov Techniques

Several Lyapunov approaches have been reported in the literature [114]–[116]. An advantage of Lyapunov's direct method is that the non-linear differential equations associated with the system do not need to be solved analytically for transient stability analysis [118]. Large-perturbation stability of various microgrid components have been discussed in the literature using Lyapunov based techniques [119], [120], such as for synchronous generators, inverters, rectifiers, and dc/dc converters. For example, in [121], an electrostatic machine based model for inverters are derived, which allows for easier small- and large-perturbation stability analysis of these systems. Lyapunov techniques can then be used on the derived "equations of motion" to analyze the large-perturbation stability.

Compared to small-perturbation studies, Lyapunov techniques have the following advantages: (1) the domain of validity and effectiveness of Lyapunov techniques is larger than that of small-perturbation analysis methods, (2) the proper representation of nonlinear power electronic converters, and (3) the adequate capture of large transient events experienced by renewable energy sources such as solar PV and wind. A system that is stable (as defined by Lyapunov-based techniques) is small-perturbation stable, but the

reverse is not always true. Thus, Lyapunov techniques give better insights on the transient stability of microgrids.

Successfully applying Lyapunov techniques to microgrids presents several challenges. First, finding the proper Lyapunov function is a significant hurdle and requires many simplifying assumptions; hence, these techniques have been limited to balanced three-phase systems. Moreover, studies that explore the dynamic interactions of power electronic converters and electromechanical systems have yet to be carried out using Lyapunov-based techniques. Additionally, Lyapunov functions can be nontrivial, so there is a need for systematic mathematical approaches that could be adopted widely with different generator and load models. Furthermore, modeling the microgrids as non-autonomous or time-varying systems is a challenging and nontrivial issue that adds another level of complexity.

4.4.1.2 Time-Domain Simulation

Large-perturbation stability analysis of microgrid systems using time-domain simulations, based on accurate models of the system components and loads, of the type found in EMT tools [121], [122], is the most effective way to investigate stability issues in microgrids, as reported in the literature [31], [123]. Time-domain simulations have some advantages over Lyapunov-based techniques, including higher accuracy and validity. On the other hand, time-domain simulations of non-linear systems are computationally intensive and typically many such simulations are required to ensure system stability over a wide variety of initial conditions and disturbances. It is also noteworthy that stability boundaries derived using time-domain simulations are precise, albeit expensive to obtain, and thus result in proper resource utilization of microgrids, as opposed to Lyapunov techniques.

Ideally, EMT tools should be used for time-domain simulations in microgrids, since they model all components in detail; however, for larger microgrids, this might be infeasible due to the computational complexities and burden. Electromechanical transient tools, also known as Transient Stability (TS) tools [124], [125], has been developed and used to address these computational issues in system transient studies, but these tools have been traditionally designed for balanced networks, and thus are not suitable for unbalanced microgrid studies. An intermediate solution could be provided by capturing unbalances in TS simulations, using phasor dynamic models that capture network and stator dynamics around the fundamental frequencies [126]-[128]. TS simulations are proposed for microgrids/distribution systems with unbalanced modeling in [129], with dynamic phasors in [130], and with transitions between dynamics and power flows solutions in [131].

4.4.1.3 Harware-in-the-Loop Studies

Real-time HIL simulations have proven to be an advanced and efficient tool for the analysis and validation of microgrids, in particular DER components and their controls. The two

main classes of real time HIL testing are Controller Hardware in the Loop (CHIL) and Power Hardware in the Loop (PHIL), as depicted in Fig. 24 and discussed next.

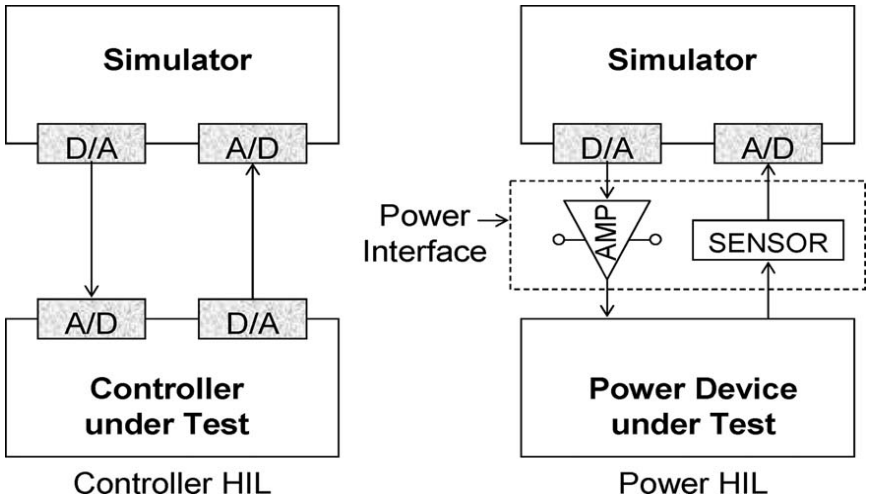

Fig. 24. PHIL and CHIL setup [117].

In CHIL simulations, a hardware controller is tested and connected to a microgrid network simulated entirely in a Digital Real Time Simulator (DRTS). For example, CHIL can be used to test an inverter controller, where the controller sends the PWM signals to the DRTS, which feeds back voltage and current measurements as analogue signals. A power system controller (e.g. distribution management system, microgrid controller) can also be tested with CHIL, where the signal exchange between the controller and the DRTS can be performed by digital or analog signals or via communication protocols. The advantages of CHIL testing compared to time-domain simulations are significant. Thus, DRTSs are able to solve the microgrid's mathematical equations in real time, allowing the implementation of control algorithms on a physical hardware controller, interfaced with the DRTS in real time. In addition, CHIL simulations can reveal weaknesses in the control algorithms, studying their performance under various realistic conditions such as time delays and noise, and interacting with complex power system models, thus providing valuable insights in control system stability issues [132].

In a PHIL setup, a part of the microgrid is simulated in great detail in a DRTS integrated with real hardware. In order to connect the hardware to a node of the simulated microgrid, an amplifier is used as an interface between the DRTS and the equipment. The amplifier receives as input a reference signal from the DRTS and provides the respective voltage value to the equipment, and a current sensor is utilized to transfer the current from the hardware to the simulator. This setup allows the user to test real equipment hardware under various circumstances, and to study the impact of the hardware on the system [133].

4.4.2 Small-Perturbation Stability

Conventionally, small-perturbation stability of a power system is studied through eigenvalue analysis by developing state-space models of the system. Efforts have been made to develop accurate state-space models of various microgrid components, such as inverters, the network, and dynamic loads [47], [134]. These studies reveal that critical low-frequency modes are highly affected by the tuning of inverters outer power sharing control loops, whereas the critical high-frequency modes are dominated by the inverter inner voltage and current control loops. However, such state-space approaches are limited to balanced systems, while microgrids in general are unbalanced systems, which is an important factor in determining the overall system stability in microgrids [31]. In this context, a combination of dynamic simulations and signal-processing methods such as the Prony technique have been shown to be effective studying the small-perturbation stability [31], [44].

Another drawback in classical state-space based approaches is that the validity and magnitude of the linearization domain is unknown. Small perturbations can be explored without an explicit knowledge of what constituents "small". In traditional power systems with large inertia and with an infinite bus, such disturbances are not likely to substantially perturb the system from its current operating state. However, since microgrids have a smaller inertia and no infinite bus, thus small perturbations are more likely to significantly affect the system.

As detailed in Section 3, this document presents a classification of stability in microgrids based primarily on the equipment origin of the potential instability (e.g., inner control loop tunings, PLL bandwidth issues, etc.). This approach is taken to avoid classical frequency/voltage categorizations, as these variables are strongly coupled in by microgrid dynamics. However, if faced with an instability, one must ultimately identify the true source of the problem. Small-perturbation stability analysis via linearization provides a useful tool for identifying the origin of the instability, by studying the left and right eigenvectors of the dynamic system matrix. Under technical conditions, a small-signal LTI model:

$$\Delta\dot{x} = A\Delta x$$

with state $\Delta x(t)$ and initial condition Δx_0 has the solution:

$$\Delta x(t) = R\mathrm{e}^{\Lambda t}L\Delta x_0$$

where Λ is the diagonal matrix of eigenvalues of A, R is (column-wise) the matrix of right-eigenvectors of A, and L is (row-wise) the matrix of left-eigenvectors of A. More simply, this can be written as [135]:

$$\Delta x(t) = \sum_{i=1}^{n} \mathrm{e}^{\lambda_i t} r_i (l_i \Delta x_0)$$

where r_i (resp., l_i) is the i[th] column of R (resp., i[th] row of L), and are normalized such that $l_i r_i = 1$. From this expression, the right-eigenvectors r_i determine the modal shape of the response, while the left eigenvectors l_i determine how greatly the initial condition excites the i[th] dynamic mode. State variables which participate heavily in a particular instability will have relatively large corresponding components within r_i, and thus the right eigenvectors provide a means of deducing the equipment origin of instability. As an example, in the case of a Control System Stability problem, it is likely to have state variables with large components within r_i pertaining to a particular piece of equipment. On the other hand, in the case of a Power Supply and Balance Stability issue, it is expected to have a wider range of state variables, corresponding to various equipment, to have larger components within r_i.

5. EXAMPLES

5.1 CIGRE Benchmark Microgrid Stability Studies

To demonstrate some of the aforementioned stability phenomena and issues in isolated/islanded microgrids, the test system in Fig. 25, which is based on the CIGRE benchmark for medium voltage distribution network introduced in [29], has been implemented in PSCAD/EMTDC. This microgrid has a 1.3 MVA diesel-based synchronous machine, a 1 MW ESS, and a 1 MW wind turbine, with the latter being modeled using an average model similar to Fig. 6. The diesel-based synchronous machine and its exciter and governor are tuned and validated according to actual measurements for the diesel gen-sets discussed in [30]; the grid and gen-set parameters are provided in Table 3 and 4 respectively, and the ESS parameters are shown in Table 5. The loads are modeled using the static exponential model (36) and (39) with a 1.5 exponent, which is a reasonable value for typical isolated microgrids [46]; the based values for P_0 and Q_0 of balanced loads are given in Table 6, with a total system demand of 1 MW and 1 MVar. Load demand and unbalance levels are different for each of the test scenarios discussed next.

5.1.1 Impact of Unbalanced Operation

To effectively study the impact of unbalanced loading on microgrid stability, the ESS is modeled in detail in this case, including the battery and its buck/boost converter, the dc/ac inverter, and the ac filter. Thus, the dc-link voltage is not ideal, with the buck/boost converter maintaining the dc-link voltage of the inverter via a cascaded PI controller.

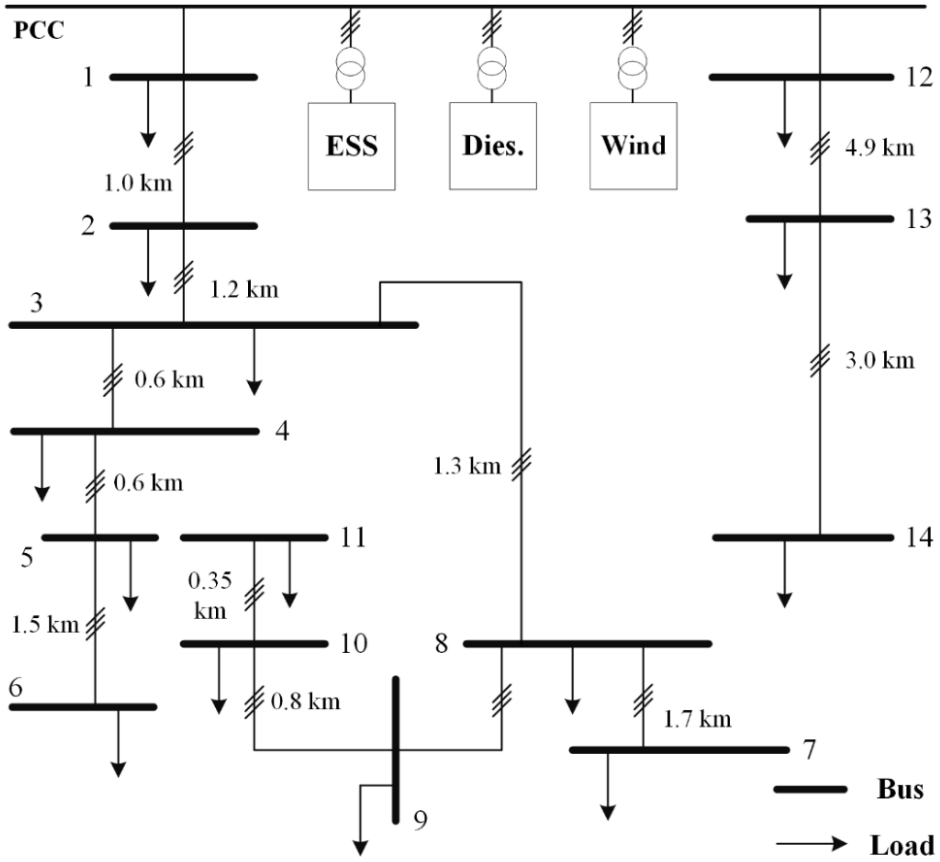

Fig. 25. Modified version of CIGRE benchmark microgrid.

TABLE 3. Line Parameters for CIGRE Test System

From	To	R'_{ph} [Ω/km]	X'_{ph} [Ω/km]	B'_{ph} [μS/km]	R'_0 [Ω/km]	X'_0 [Ω/km]	B'_0 [μS/km]	l [km]
1	2	0.173	0.432	3.83	0.351	1.8	1.57	1.2
2	3	0.173	0.432	3.83	0.351	1.8	1.57	1
3	4	0.173	0.432	3.83	0.351	1.8	1.57	0.61
4	5	0.173	0.432	3.83	0.351	1.8	1.57	0.56
5	6	0.173	0.432	3.83	0.351	1.8	1.57	1.54
6	7	0.173	0.432	3.83	0.351	1.8	1.57	0.24
7	8	0.173	0.432	3.83	0.351	1.8	1.57	1.67
8	9	0.173	0.432	3.83	0.351	1.8	1.57	0.32
9	10	0.173	0.432	3.83	0.351	1.8	1.57	0.77
10	11	0.173	0.432	3.83	0.351	1.8	1.57	0.33
3	8	0.173	0.432	3.83	0.351	1.8	1.57	1.3
12	13	0.173	0.432	3.83	0.351	1.8	1.57	4.89
13	14	0.173	0.432	3.83	0.351	1.8	1.57	2.99

TABLE 4. Diesel Gen-Set Parameters for CIGRE Test System (in p.u.)

Ac1A Exciter Parameters				
K_A	T_A	T_B	T_C	K_F
310	0.012 s	0 s	0 s	0.03
T_F	K_E	T_E	K_D	K_C
1 s	1	0.5 s	0.38	0.2
VR_{max}	VR_{min}	VA_{max}	VA_{min}	
6.03	-5.43	14.5	-14.5	
Woodward Governor Parameters				
a_n	b_n	c_n	a_d	b_n
0	0.38	1	1	1000
c_d	K_G	$T1_{lead}$	$T1_{lag}$	$T2_{lead}$
55555.5	277777.7	0.35 s	0.002	0
$T2_{lag}$	T_i			
0.015	1 s			
Gen-Set Parameters (units in pu unless specified otherwise)				
H	R_a	X_p	X_d	X'_a
0.5134 s	0.005	0.063	1.91	0.1318
T'_{d0}	X''_d	T''_{d0}	X_q	X''_q
3.03 s	0.092	0.054 s	0.96	0.122
T''_{q0}	ω	V^{LN}_{RMS}	I^{L}_{RMS}	
0.05 s	377 rad/s	0.346 kV	1.366 kA	

TABLE 5. ESS Design Parameters for CIGRE Test System

L_f	R_f	C_f	R_d	$V_{ratedDC}$
0.166 mH	4.2 mΩ	626.8 µF	84.7 mΩ	750 v
$C_{DC-link}$	R_B	L_{chopf}	f_s	V_{RMSL-L}
20 mF	0.2 Ω	3.3 mH	3 kHz	460 v

In this case study, the diesel and wind generators are not connected, with the ESS operating in the grid-forming mode. The system base load is scaled down to 950 kW and 100 kVar by multiplying all P loads by 0.95 and Q loads by 0.1. At *t = 0.5*s, the load reactive power is increased by 100% to 200 kVar, and the active power load is kept near the ESS rated power. To evaluate the impact of unbalanced loading, the performance of the system is first simulated with balanced loading, and then the load at phase *c* is scaled up to twice the load on phases *a* and *b*, while keeping the total 3-phase unbalanced load power equal to its equivalent balanced load values.

TABLE 6. Base Load Parameters for CIGRE Test System

Node	P_0 *[p.u.]*	Q_0 *[p.u.]*
1	0.084	0.084
2	0.1092	0.1092
3	0.0713	0.0713
4	0.0582	0.0582
5	0.0905	0.0905
6	0.0468	0.0468
7	0.0582	0.0582
8	0.0655	0.0655
9	0.0509	0.0509
10	0.0728	0.0728
11	0.08	0.08
12	0.084	0.084
13	0.0633	0.0633
14	0.0643	0.0643

Fig. 26 illustrates the active power, reactive power, instantaneous voltages, and dc link voltages of the ESS. The system remains stable when the loading is balanced after the load perturbation, whereas it shows sustained oscillations after the perturbation when unbalanced. As illustrated in Fig. 26(d), the dc-link capacitor voltage ripple becomes significant for the system with unbalanced loading, leading to system instability. Note that the chosen dc link capacitor is relatively large for a 1 MW ESS, and the active power is within the range for which the system is designed. Also, observe that the voltage magnitudes at the PCC bus are close to 1 p.u. for the balanced loading scenario, while for the unbalanced case, there are significant differences in the phase voltages. This is an

example of Power Supply and Balance Stability, in which the dc-link capacitor is unable to keep the voltage ripples within acceptable ranges due to the excessive reactive power demand.

5.1.2 VSC Modeling [32]

In this case, the diesel and wind generators are not connected and the ESS controls voltage and frequency. The total active power load is scaled down to 950 kW, while the reactive power is scaled down to 100 kVar, balanced among the three phases. At t = 0.5s, the loads' reactive powers are proportionally increased by a total of 100 kVar, and at t = 11.5s, the total load reactive power is again proportionally increased by 100 kVar; note that the active power load is near the ESS rated power. To evaluate the impact of DERs modeling on microgrid stability, the performance of the system with the ESS modeled in detail, with the buck/boost converter (Fig. 10) and the VSC (Fig. 2), is compared with the ideal-dc-link and VSC inverter model (Fig. 2), as well as with the average ESS model (Fig. 6). Note that the controls and system parameters are the same for all these 3 models.

Fig. 27 shows the ESS active power, reactive power, and RMS voltage of phase *a* at the PCC bus. Note that before t = 11.5s, the ESS performance is satisfactory for all the three modeling techniques. Due to switching in the system, there is some ripple in both the active and reactive powers in the ideal-dc-link and full detailed models of the ESS. The Total Harmonic Distortion (THD) of the instantaneous voltage is 0.25% for the average model, 3.92% for ideal-dc-link model, and 3.63% for the detailed model. After t = 11.5s, the system remains stable for the average and ideal-dc-link models, whereas it shows unsustained oscillations for the detailed model. Also, observe that the voltage magnitudes at the PCC are close to the nominal values in the average and ideal dc link models, as compared to the detailed model of the ESS which exhibits considerable voltage deviations.

The differences observed in the performance of different modelling approaches can be due to the: the dc-link voltage dynamic and/or the high frequency switching. To effectively isolate the impact of each factor, an eigenvalue study is performed first based on a signal-processing technique applied to the dc-link voltage signal. Second, the model proposed in [32] is used to isolate the impact of the higher frequencies on the system.

The dc-link voltage signal of the detailed model is used to identify the critical eigenvalues shown in Fig. 28, before and after the second disturbance, using MATLAB's Steiglitz-McBride function. Observe that the dominant eigenvalues are pushed to the right-half plane after the second disturbance, resulting in the undamped oscillations in Fig. 27.

To identify and isolate the impact of switches on the performance of the system, the model in Fig. 29, in which the switches are replaced by dependent voltage and current sources is used; the control system remains the same as in Figs. 2 and 10. Two models are developed based on the value of the dependent voltage and current sources. Thus, to emulate the

performance of the model with switches, the currents through and voltages across the switches are analyzed in each switching state and the dependent voltage and current sources values are determined accordingly; this model is referred to as the Switching Dependent Source Model (SDSM). To eliminate the impact of high-frequency switching, an averaging technique based on the fundamental frequency component is used, and the values of dependent voltage and current sources are defined accordingly; this model is referred here as the Average DSM (ADSM). Details of these calculations are provided in [32].

Fig. 30 shows the ESS active power, reactive power, and phase *a* RMS voltage at the PCC for the ADSM and SDSM. Observe that the performance of the ADSM is exactly the same as the performance of the average model shown in Fig. 27, and the performance of the SDSM is exactly the same as the performance of the detailed model. By comparing the performance of these models, it is possible to isolate the impact of high-frequency switching due to the switches, since the physical components of both DSMs are all the same, and only the values of the coefficients of the dependent sources are different, reflecting the different switching content in the two models. Comparing Figs. 27 and 30 confirms that it is not possible to capture the behaviour of the detailed model by neglecting the switches and/or the impact of high-frequency switching. In addition, it can be concluded that including the dc-link voltage dynamics is necessary but not sufficient to capture the accurate dynamic performance of the system.

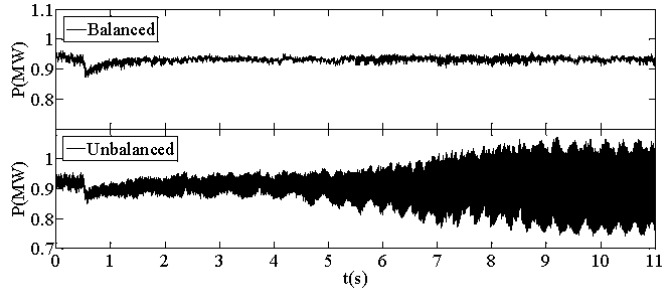

(a)

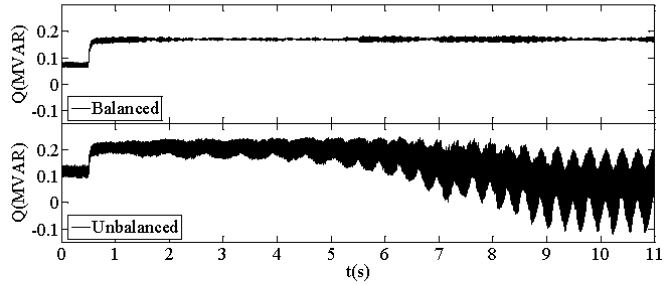

(b)

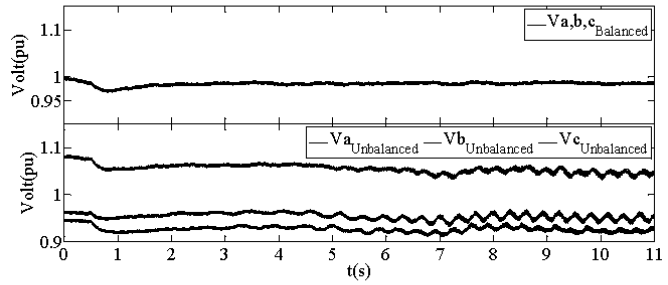

(c)

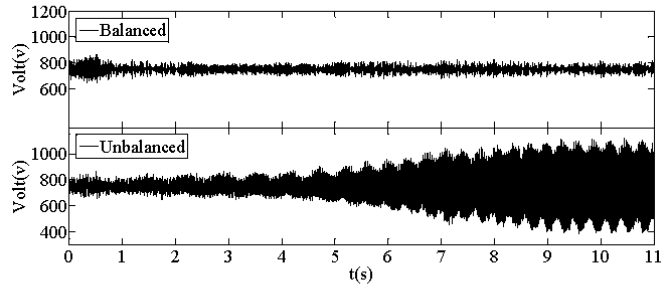

(d)

Fig. 26. Balanced versus unbalanced load: ESS (a) active power, (b) reactive power, (c) instantaneous voltages at the PCC bus, and (d) dc-link voltages.

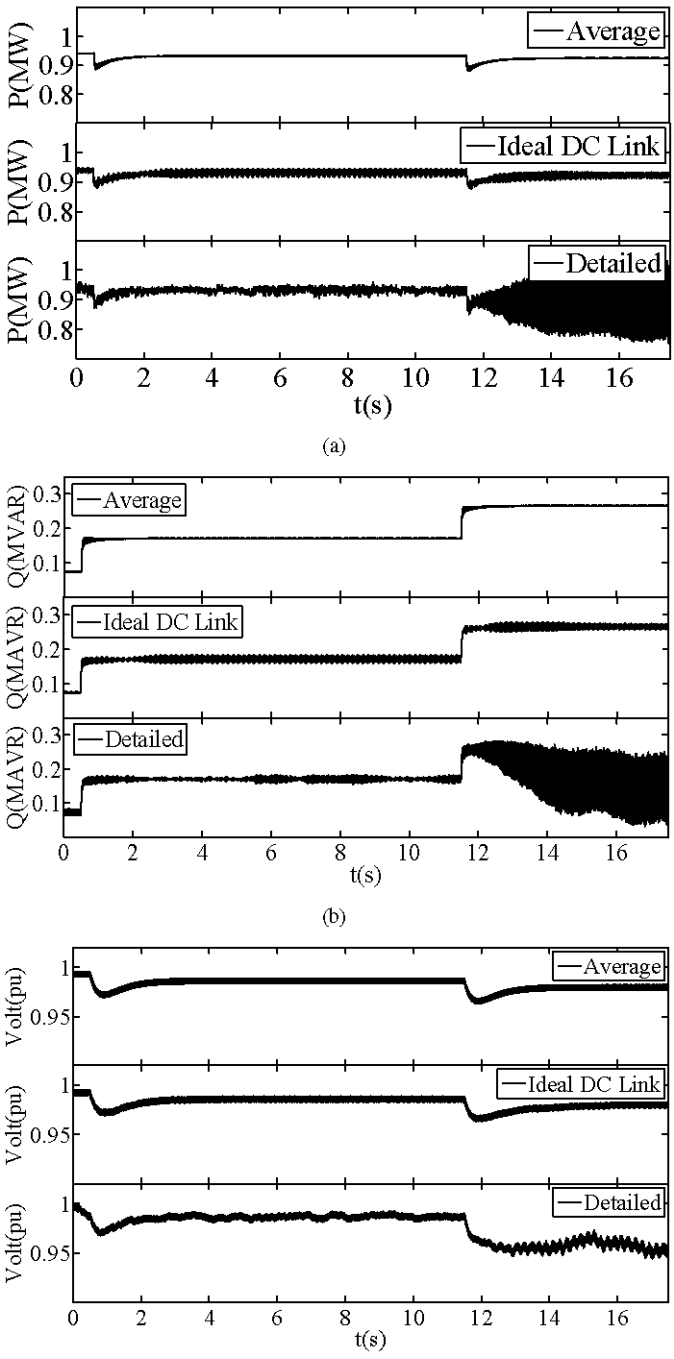

Fig. 27. Impact of VSC modeling: ESS (a) active power, (b) reactive power, and (c) RMS phase *a* voltage at the PCC bus.

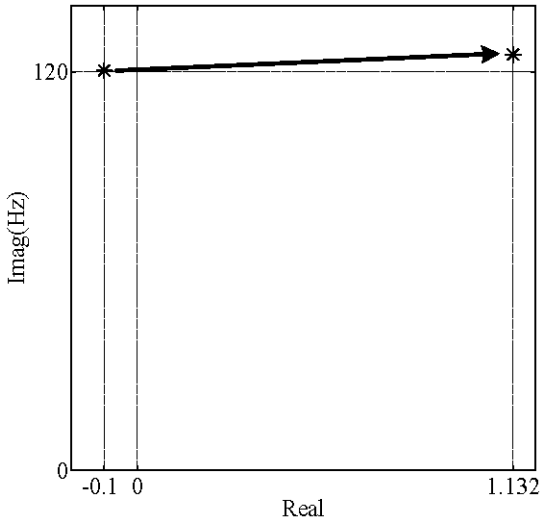

Fig. 28. Impact of VSC modeling: dominant eigenvalue before and after instability.

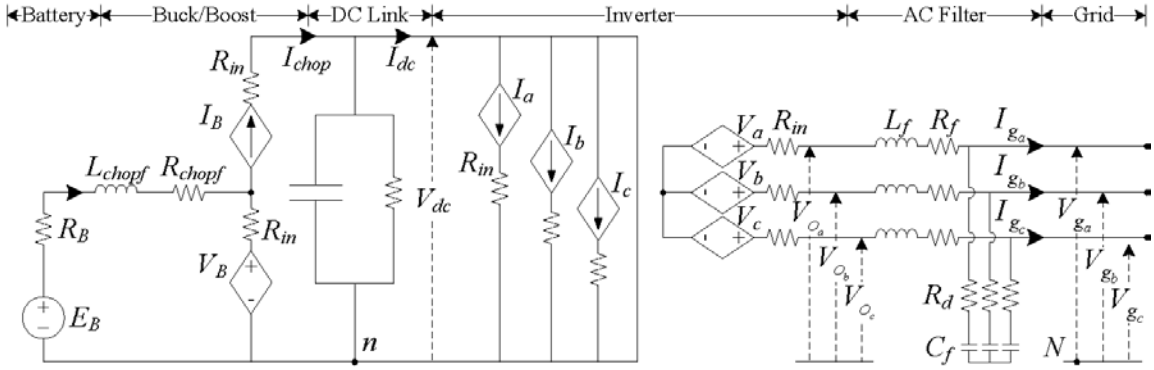

Fig. 29. Impact of VSC modeling: schematic of a Battery ESS with switches modeled as dependent sources [32].

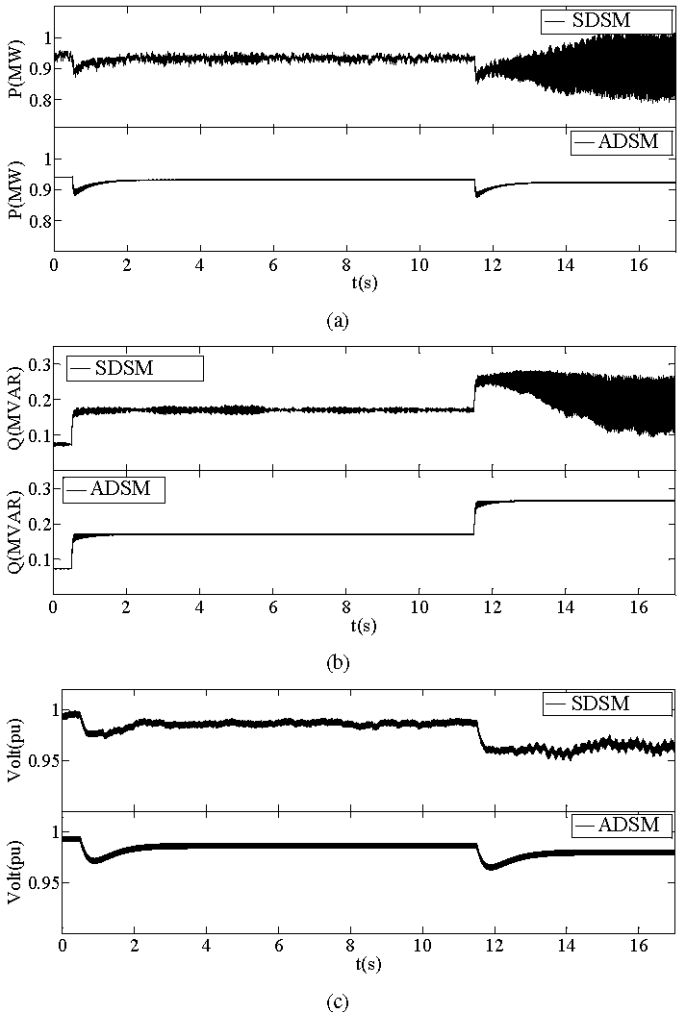

Fig. 30. Impact of VSC modeling: ESS (a) active power, (b) reactive power, and (c) RMS phase *a* voltage at the PCC bus.

5.1.3 Voltage-Frequency Dependency

In this case, the diesel generator is connected and is the master voltage and frequency controller, and the ESS is providing 0.5 MW of active power in the grid-feeding mode. The wind turbine is generating 300 kW of active power, and the load scaled so that the total system demand is 1.6 MW and 0.2 MVar, balanced among the three phases. At $t = 1$s, the wind generator active power output is decreased to 50 kW. In addition, to demonstrate the impact of voltage changes on the system frequency, a -0.1 step change is passed through a lag filter with a time constant of 0.4 s, and is then added to the machine voltage regulator set-point, to simulate the effect of the Voltage-Frequency Controller (VFC) [44].

Fig. 31 shows the wind power output, diesel engine active power, system frequency, and the RMS voltage at the PCC bus. Note in these figures that the voltage change has a considerable impact on the system frequency response, compensating for the power mismatch in the system due to the wind power reduction. As seen in Fig. 31(b), the diesel engine active power output barely increases when the system voltage changes, compared to a 250 kW increase for the base system. This is due to the linkage between the voltage magnitude and active power consumption [46], which is the base of the VFC proposed in [44]. Thus, a closed-loop version of the VFC is demonstrated here, as shown in Fig. 32.

The parameters of the VFC in Fig. 32 are shown in Table. 7, and are first estimated based on the Ziegler-Nichols tuning technique, and then refined experimentally. Fig. 33 shows the frequency response of the system with the modified VFC is much improved compared to the base system. In addition, the voltage steady-state error is zero, due to the negative feedback loop of the VFC. This is an example of Frequency Stability in microgrids, discussing a control mitigation approach based on the particular characteristics of microgrids.

TABLE 7. VFC Parameters

VFC Parameters				
K_P	K_I	K_{VFC}	τ_{lead}	τ_{lag}
0.04	0.154	1	0.04 s	0.001 s
VFC_{max}	VFC_{min}	G	τ_1	
0.1	-0.1	2.5	0.1 s	

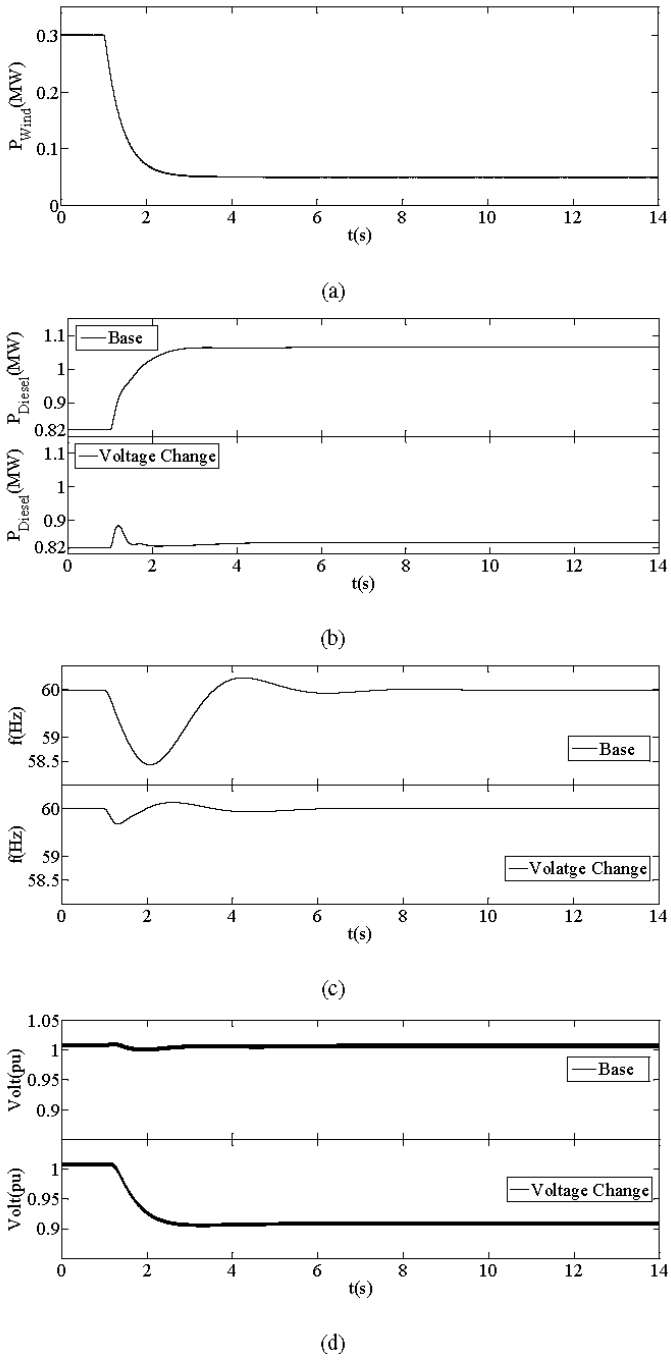

Fig. 31. Voltage-frequency dependency: (a) wind turbine active power, (b) diesel engine active power, (c) frequency, and (d) RMS voltage at PCC bus.

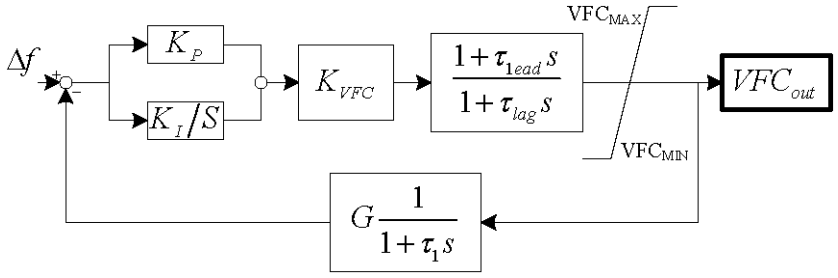

Fig. 32. Modified version of the VFC in [44].

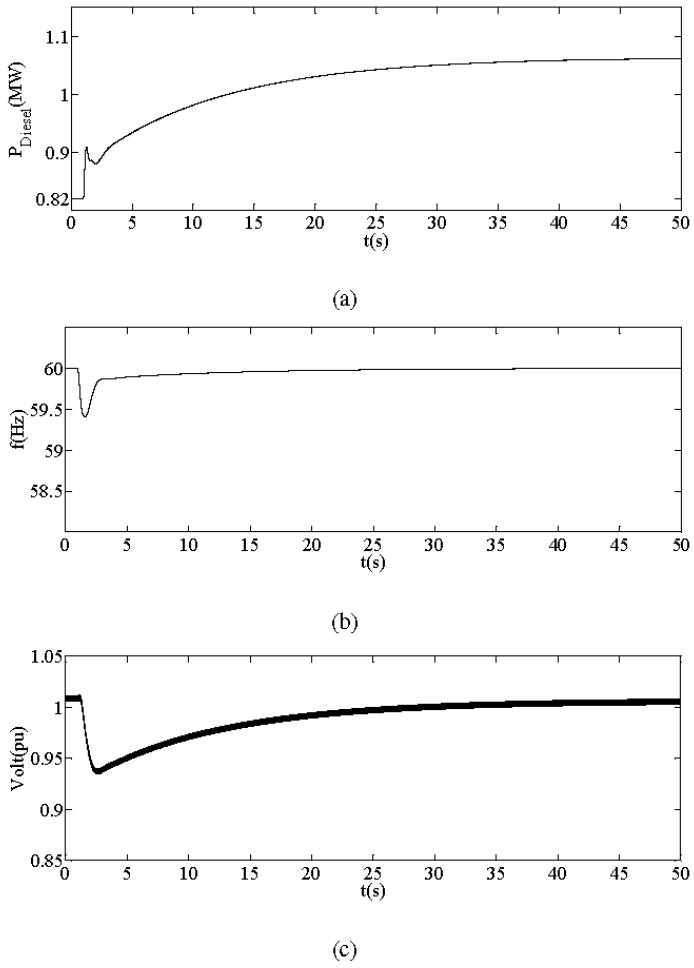

Fig. 33. Case C with VFC: (a) diesel engine active power; (b) frequency, and (c) RMS voltage at PCC.

5.2 Impact of the Bandwidth of the PLL Synchronization Loop

A study of the three-bus system, shown in Fig. 34 has been carried out in a real-time digital simulation platform. When the loadability is close to 1 and the slack bus voltage is slightly distorted (THD=0.52%), an instability would be misjudged by the PLL. A fast PLL can maintain stability in this case.

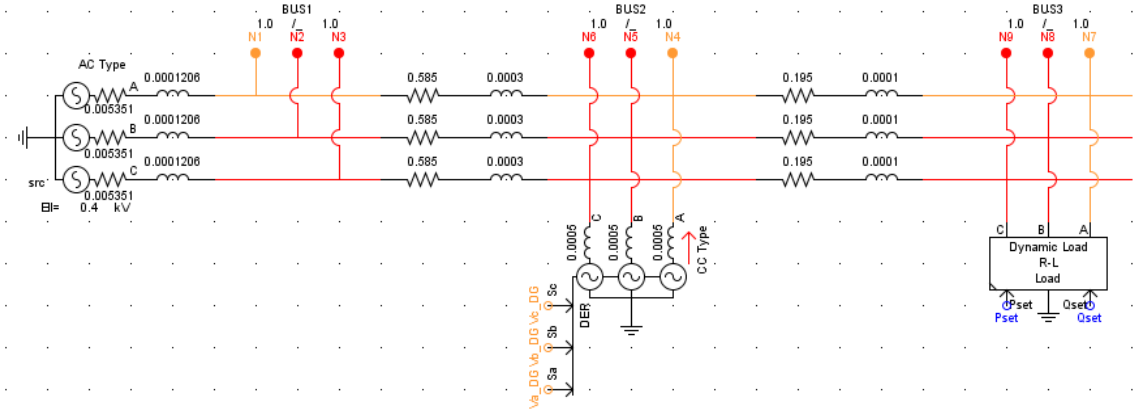

Fig. 34. Three-bus test system for PLL stability studies.

The current control scheme for the grid-connected inverter at Bus 02 is shown in Fig. 35, where the current controller G_c is implemented in the dq frame and the phase angle θ' for the (inverse) Park transform is obtained from a Synchronous Reference Frame (SRF) PLL. An equivalent ZIP model of the inverter using such current control as well as PLL is represented by

$$\begin{bmatrix}\Delta i_d\\ \Delta i_q\end{bmatrix} = \overbrace{\begin{bmatrix}Y_{dd} & 0\\ 0 & Y_{qq}\end{bmatrix}\begin{bmatrix}\Delta v_d\\ \Delta v_q\end{bmatrix}}^{\text{Z-component}} + \overbrace{\begin{bmatrix}I_{dd} & 0\\ 0 & I_{qq}\end{bmatrix}\begin{bmatrix}\Delta i_{dref}\\ \Delta i_{qref}\end{bmatrix}}^{\text{I-component}} + \begin{bmatrix}\theta_{d1}\\ \theta_{q1}\end{bmatrix}\Delta\theta' \tag{47}$$
$$= \begin{bmatrix}Y_{dd} & 0\\ 0 & Y_{qq}\end{bmatrix}\begin{bmatrix}\Delta v_d\\ \Delta v_q\end{bmatrix} + \begin{bmatrix}I_{dd} & 0\\ 0 & I_{qq}\end{bmatrix}\begin{bmatrix}\Delta i_{dref}\\ \Delta i_{qref}\end{bmatrix} + \begin{bmatrix}0 & \theta_{d1}G_{PLL\_op(s)}\\ 0 & \theta_{q1}G_{PLL\_op(s)}\end{bmatrix}\begin{bmatrix}\Delta v_d\\ \Delta v_q\end{bmatrix}$$

where i_{dref}, i_{qref}, i_d, i_q, v_d, and v_q are the current reference, grid current, and grid voltage in the dq frame, respectively; Y_{dd}, Y_{qq}, I_{dd}, and I_{qq} are the equivalent admittance and current components of the inverter when the PLL is not considered, and the constant power component is zero. The effects of synchronization, represented by the open-loop transfer function of PLL G_{PLL_op}, can be considered as part of the constant impedance component.

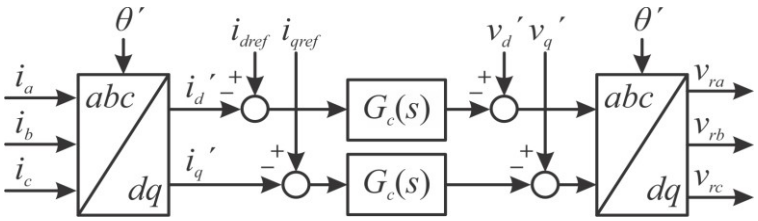

Fig. 35. Three-bus test system for PLL stability studies.

As shown in Fig. 36, when the load at Bus 3 increases at t = 3.5s and max loadability is approached, a converter with a slow PLL will cause a system collapse, as shown in Fig. 36(a), while a fast PLL can keep the system in stable conditions, as illustrated in Fig. 36(b). This is an example of Control System Stability, and particularly Converter Stability.

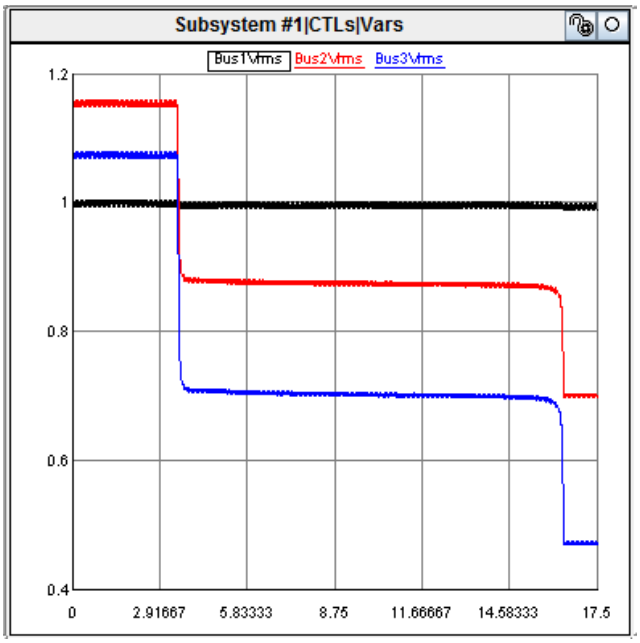

(a)

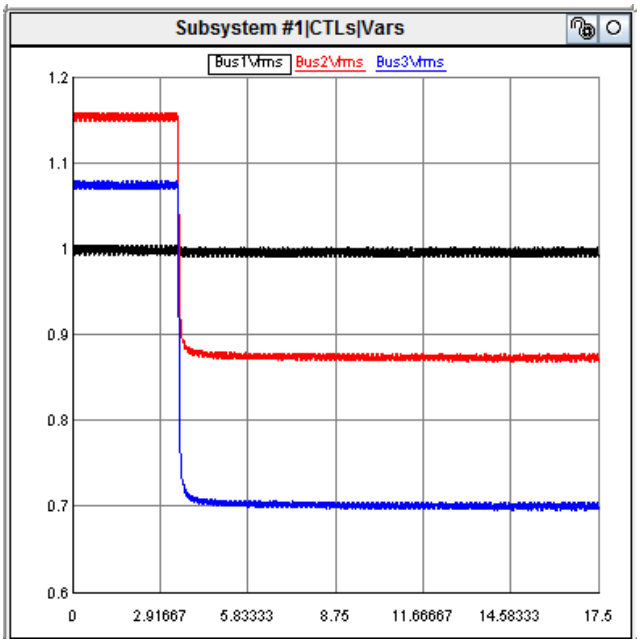

(b)

Fig. 36. Three-bus test system voltages (in pu): (a) 5.7 Hz PLL, and (b) 20 Hz PLL.

5.3 Parallel Converter Droop Control Issues

This example demonstrates that oscillations can occur in parallel converters with V-I droop control [136], when the droop control parameters for the two converters are set differently. These types of oscillations will not be observable if the parallel converters are modeled as an aggregated converter or their droop parameters are the same, reflecting a Power Supply and Balance Stability issue. Roughly speaking, such oscillation are because of the loop current, and hence powers, flowing from one converter to another due to the difference in two voltage sources representing the two converters. When the droop parameters are exactly the same, the two voltage phasors are the same; when the droop parameters are different, the two voltage phasors are not the same.

Fig. 37 depicts the test system [136], and Fig. 38 illustrates the control block for the V-I droop. A linearized system model is built for the system and eigenvalue analyses are carried out, obtaining the map of poles and zeros of the microgrid with V-I droop using Control Design Toolbox in MATLAB. The locations of the dominant poles can be found for specific droop coefficients. The *m* and *n* values are based on physical units (V/A); thus, for $m_1 = 0.4$ and $m_2 = 0.8$, increasing n_1 from 0.01 to 1 and n_2 from 0.02 to 2, yields the plot of dominant poles shown in Fig. 39. With an increasing n_k, the dominant poles are drifted away from the imaginary-axis, so that the dynamic response becomes faster and the damping ratio gets larger. This figure also shows the movement of dominant poles with increasing m_1 from 0.004 to 0.4 and m_2 from 0.008 to 0.8, for $n_1 = 1$ and $n_2 = 2$.

The results depicted in Fig. 39 show that the dominant poles are closer to the imaginary-axis with decreasing m_k or n_k, but they are still in the Left Half Plane (LHP); hence, for small m_k or n_k values, oscillations may appear due to the low system damping. However, if both of m_k and n_k are small, the system becomes unstable because of the locations of the dominant poles, as shown in Fig. 41(a), unless $m_1 = m_2$ and $n_1 = n_2$, which make the system stable, as shown in Fig. 41(b).

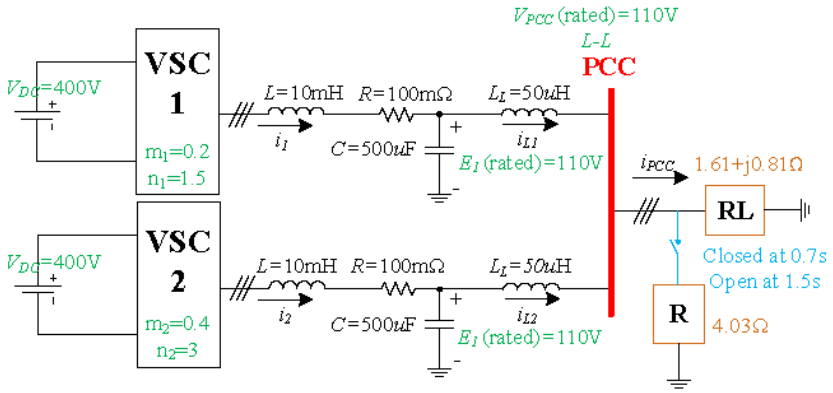

Fig. 37. Two DERs support one load through parallel VSCs.

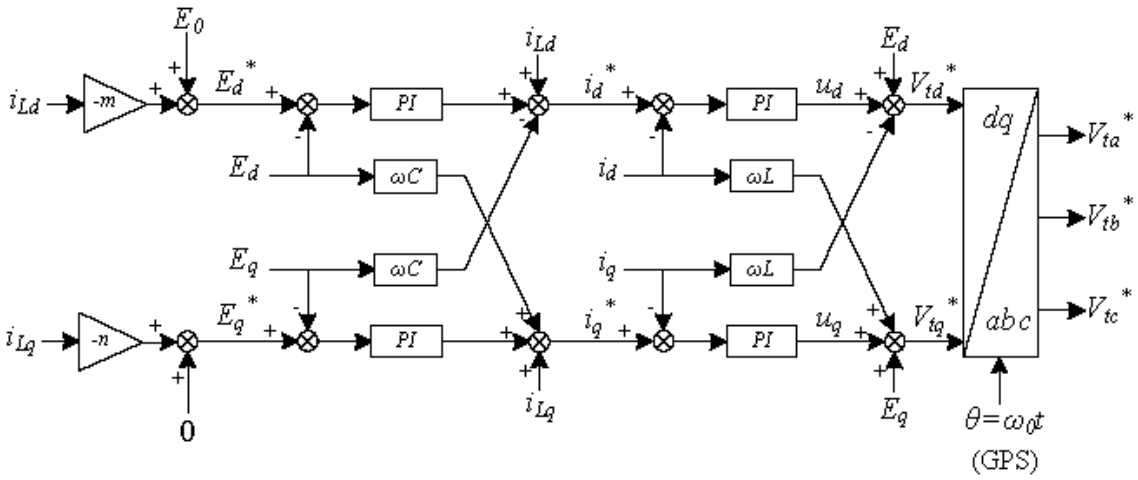

Fig. 38. Control block diagram for V-I droop.

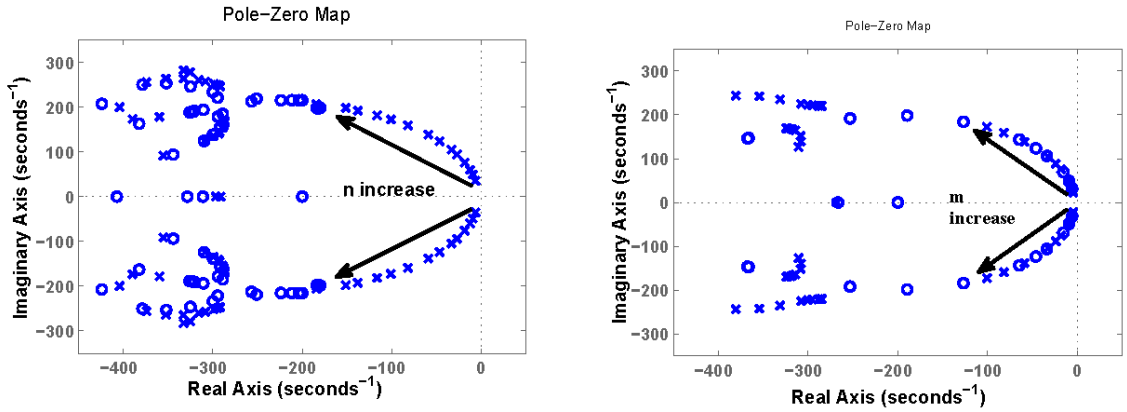

Fig. 39. Increasing n_1 and n_2 and m_1 and m_2 leads to the dominant poles moving to the LHP.

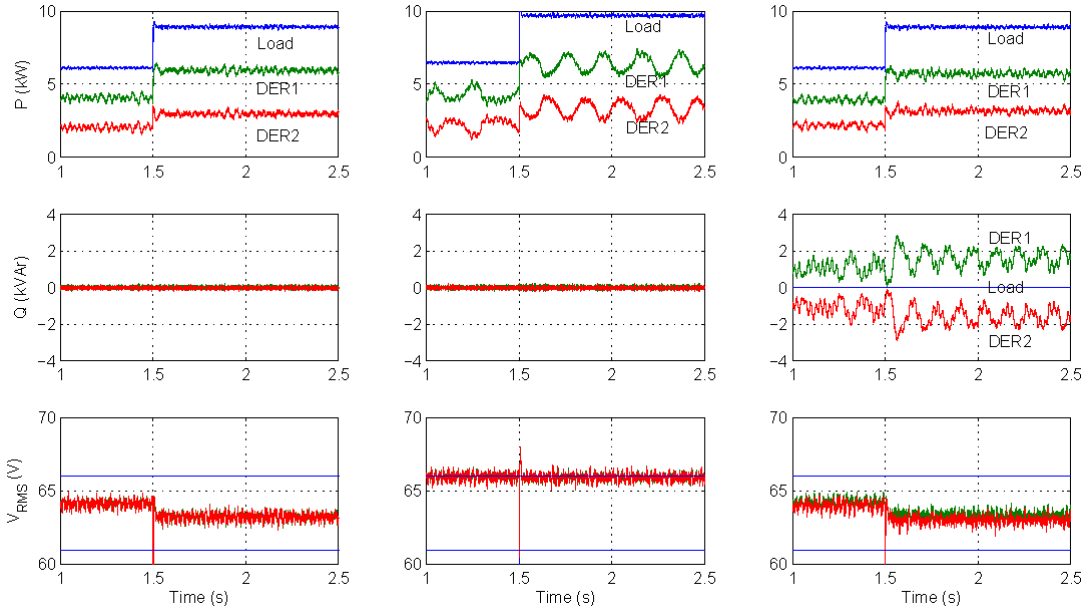

Fig. 40. (a) $m_1 = 0.09$, $m_2 = 0.18$, $n_1 = 1$, $n_2 = 2$; (b) $m_1 = 0.004$, $m_2 = 0.008$, $n_1 = 1$, $n_2 = 2$; (c) $m_1 = 0.09$, $m_2 = 0.18$, $n_1 = 0.01$, $n_2 = 0.02$. The straight lines in voltage plots represent a ±4% range.

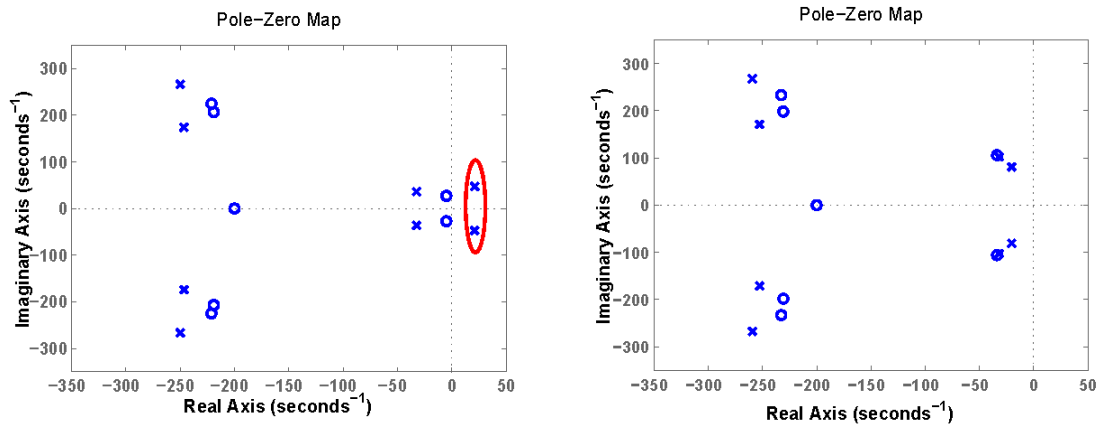

Fig. 41. (a) $m_1 = 0.004$, $m_2 = 0.008$, $n_1 = 0.01$, $n_2 = 0.02$; (b) poles and zeros when $m_1 = m_2 = 0.04$, $n_1 = n_2 = 0.04$.

Simulation results of the detailed model, including power electronic switching, are used to verify the capability of the V-I droop control power sharing and the effect of parameters on stability. In this case, loads are modeled as impedances, with the load impedance being

reduced to have a power increase. Due to the effect of the current controller, the currents are kept constant at the moment when the step change is applied; this causes a sudden reduction in the PCC voltage or load bus voltage. The results of these simulations are shown in Fig. 40. In Fig. 40 (a), there is no oscillation issue with the chosen droop coefficients, with the voltages being within the ±4% range. If m_1 and m_2 are reduced to 0.004 and 0.008, power oscillations appear as shown in Fig. 40 (b). If n_1 and n_2 are reduced to 0.01 and 0.02, then reactive power shows oscillations as illustrated in Fig. 40 (c); these oscillations are caused by circulating currents which are basically q-axis currents going back and forth between the DER units, and therefore increasing the stress on and losses in transmission lines. This is an example of Power Supply and Balance Stability.

5.4 Interactions Among Diesel Engines and Converters with f-P and V-Q Droops

This example, from [137], demonstrates that the droop gains of diesel engine synchronous generators and inverters should be coordinated to avoid instability. The study system is shown in Fig. 42, based on the benchmark system of IEEE standard 399-1997 [138], and has two diesel-engine generators and two converter-interfaced DERs that form a microgrid. Under islanded conditions, the breaker connecting the microgrid to the utility is open.

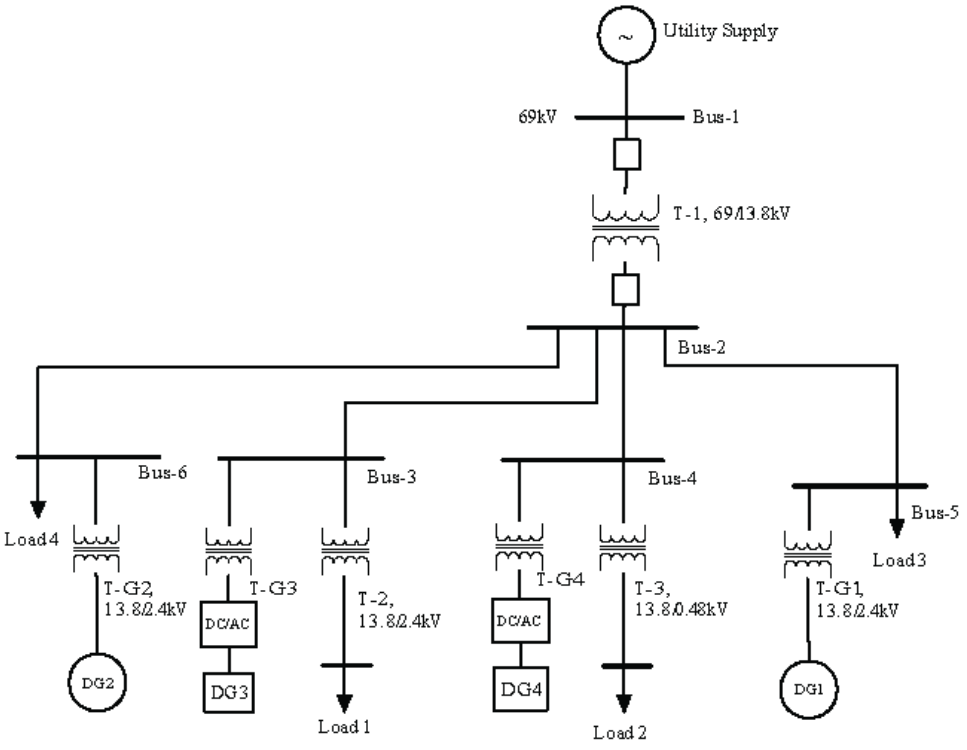

Fig. 42. IEEE distribution test system.

DG1 and DG2 are diesel-engine synchronous generators that are equipped with primary frequency controls as shown in Fig. 43. DG3 and DG4 are inverter-interfaced generators with the f-P and v-Q droop controls, shown in Fig. 44. A root locus analysis of the system shows that there is a gain limit for the diesel generators, as shown in Fig. 45, where the droop gain of the diesel engine is limited to 4.33. Fig. 46 illustrates the oscillatory instability due to a large droop gain in the diesel engine when the system is subject to a small disturbance. This is an example of Power Supply and Balance Stability, since the instability can be avoided by modifying the droop gains of either the diesel engines and/or the inverter-interfaced generators.

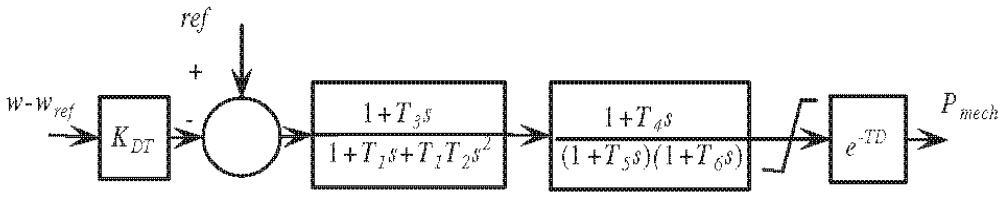

Fig. 43. DG1 and DG2 diesel generator governor model.

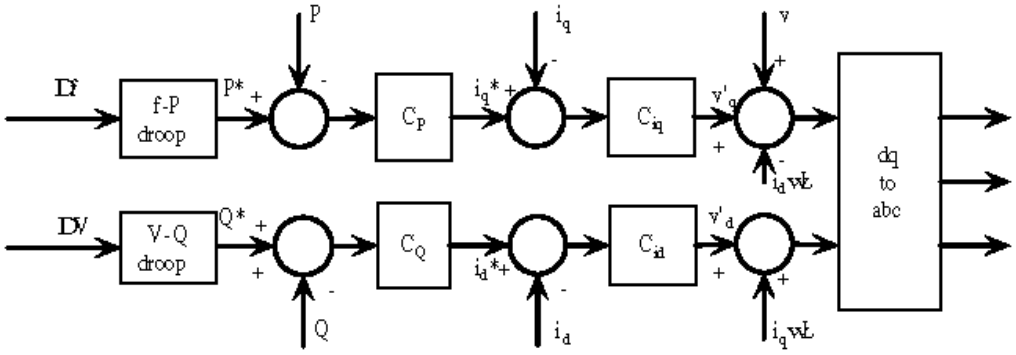

Fig 44. Control system of DG3 and DG4 inverter-interfaced generators.

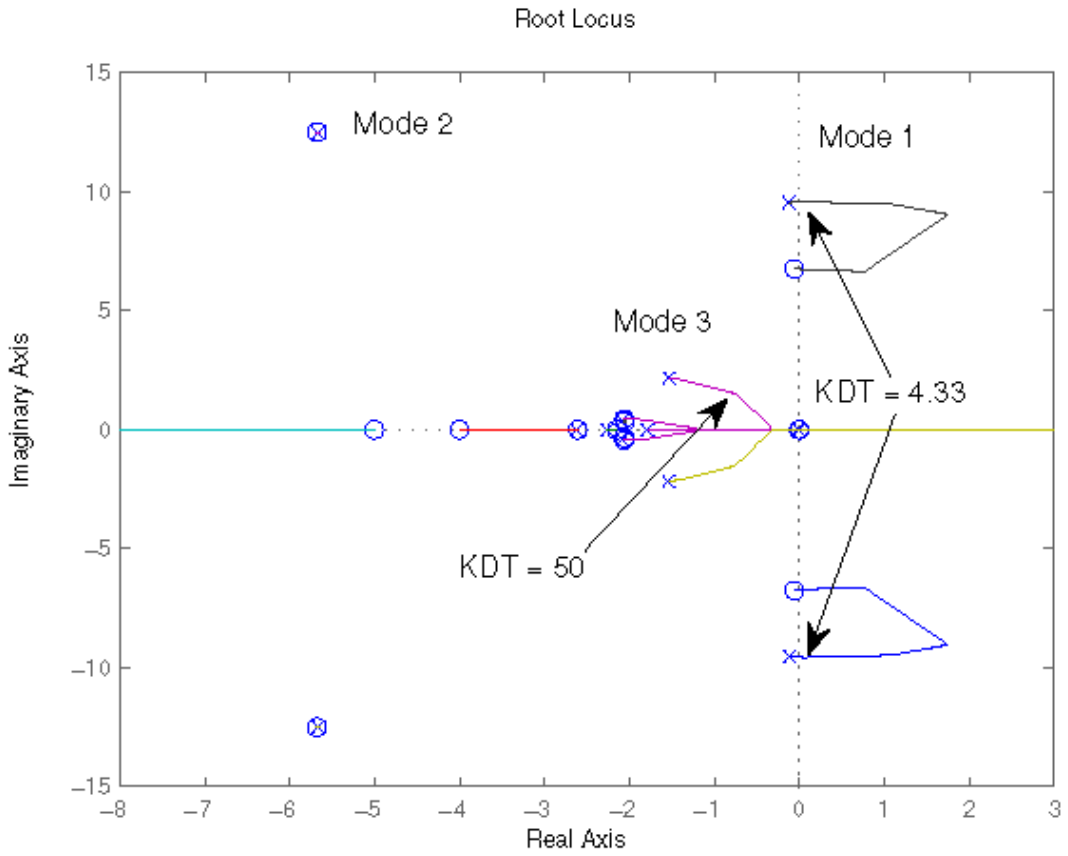

Fig. 45. Root locus with a changing f-p droop gain of the diesel generator, with an f-p droop gain of the inverters K_{inv} = 25.

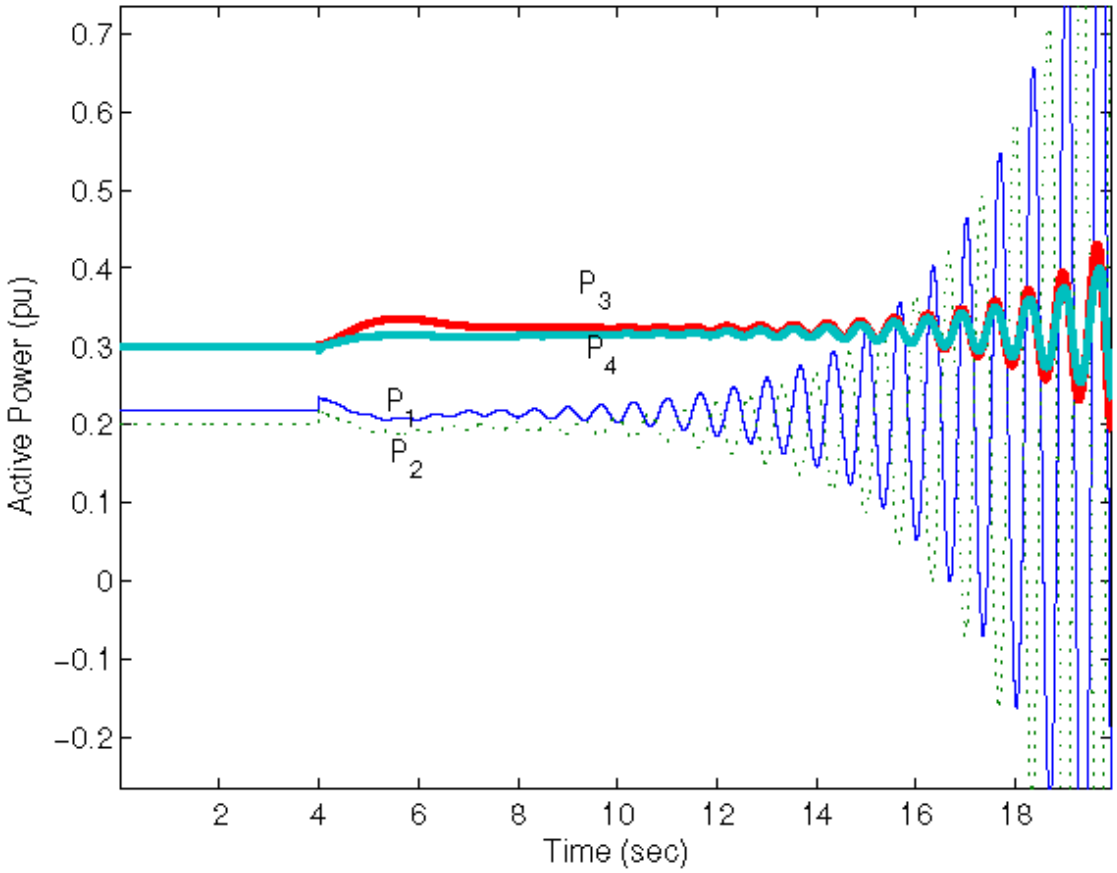

Fig. 46. Dynamic response of DERs when there is an increase of 0.034 pu in the load at Bus 5, for K_{inv} = 25, and K_{DT} = 10.

5.5 Canadian Solar Microgrid Test Centre Examples

The Canadian Solar Microgrid Test Centre (MTC) is an industry-based effort to establish a hardware simulation tool for development and testing of high renewable-energy penetration microgrids, for both islanded and grid-tied systems. The MTC is equipped with a diesel generator, renewable energy resources (wind turbine and PV system), PV and wind resource simulators, grid simulator, energy storage devices, and various test loads to facilitate design and testing of microgrid solutions. Fig. 47 shows the MTC facility diagram, which can be operated in islanded mode, grid-connected mode through the main breaker, and grid-connected mode through the grid simulator. Transition between off-grid and grid-connected modes can be accomplished seamlessly.

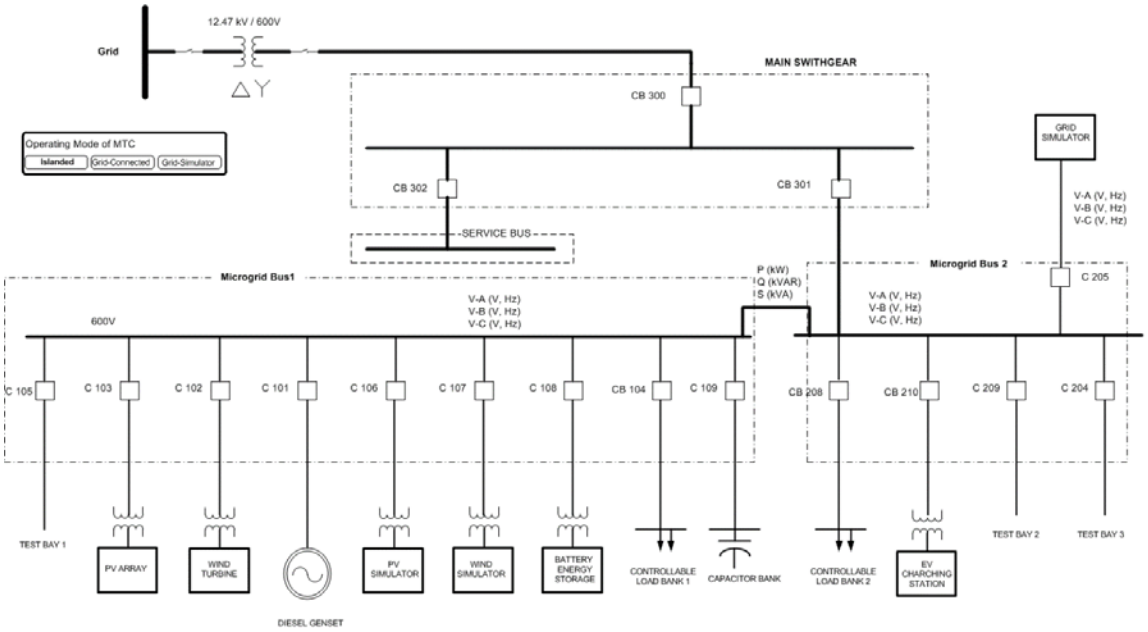

Fig. 47. Canadian Solar microgrid test facility.

At least one asset in the microgrid should be in grid-forming mode, while the rest can be in grid-following mode. The battery energy storage inverter (200 kW) and diesel generator (100 kVA) have a capability to be operated in both grid-forming and grid-following modes, while the PV simulator inverter (90 kW) and wind simulator inverter (100 kW) can be only in grid-following mode. The battery energy storage system is based on Li-Ion technology, and the battery inverter can be operated in PQ mode, i.e. grid-following, or in droop mode, i.e. grid-forming. The diesel-based synchronous machine is equipped with a governor, AVR, and communication inner controllers. The PV inverter is equipped with MPPT and also external PQ curtailment control. The wind inverter is equipped with external PQ control with curtailment capability. The facility has a 200 kW R-L controllable load bank, and a 30 kVAR capacitor bank to emulate RLC loads; three phase/single phase and unbalanced load profiles can be applied using the load bank controller.

For the four cases discussed next, the system includes the diesel generator, the load bank, the PV simulator, and the battery energy storage system in off-grid mode for Cases 1, 2, and 3. The wind simulator, grid simulator, and battery energy storage system are utilized in Case 4.

5.5.1 Frequency Stability

Case 1: In this test, the diesel generator and the load bank are connected to the microgrid bus. The diesel genset is the only generator in this case, which is the master voltage and frequency control operating in isochronous mode. To demonstrate the impact of load drop on system frequency, the load is decreased from 80 kW to 40 kW.

Fig. 48 illustrates the waveform of the voltage at the microgrid bus recorded by a power quality meter. Observe that the voltage slightly increases; also, frequency increases from 60 Hz to 61.61 Hz, with F in Fig. 48 being the point at which the frequency is higher than 60.1 Hz.

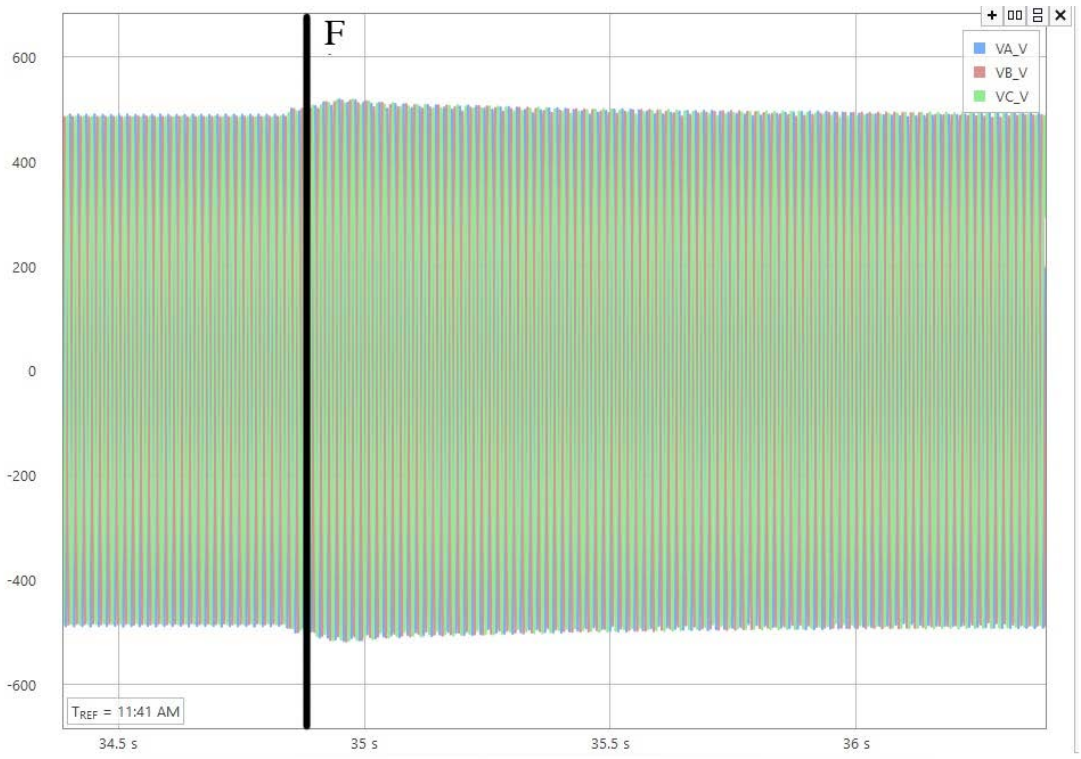

Fig. 48. Voltage waveform of the microgrid bus (in V) with only diesel genset and a 40 kW load drop, with F indicating the point at which frequency exceeds 60.1 Hz.

Case 2: In this test, the diesel generator, the load bank, and the PV inverters are connected to the microgrid bus. The diesel genset is the grid-forming unit operating in the isochronous mode. The PV inverters are in MPPT mode. The load is 80 kW, the PV simulator active power output is 50 kW, and the diesel genset covers the rest of the load (i.e., 30 kW). To

demonstrate the impact of an active power drop of the renewable energy resource, the active power output of the PV array simulator is decreased from 50 kW to 10 kW.

Fig. 49 illustrates the waveform of the voltage at the microgrid bus when the PV output is decreased. Note that, the voltage decreases from 490.6 V to 462 V. The frequency decreases from 60 Hz to 58.472 Hz, with F in Fig. 49 being the point at which the frequency is less than 59.9 Hz.

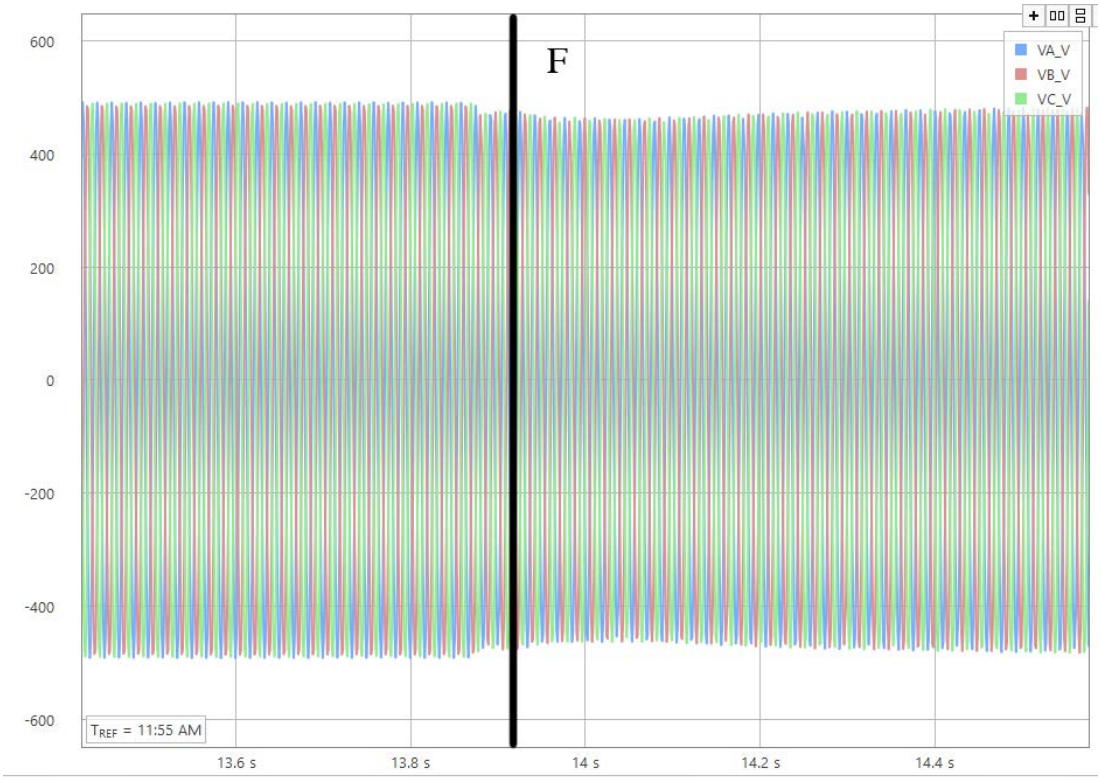

Fig. 49. Voltage waveform of the microgrid bus (in V) with PV and diesel generator for a 40 kW drop in PV output.

Case 3: In this test, the diesel generator, load bank, PV inverters, and battery energy storage are connected to the microgrid bus. The load, diesel generator, and PV inverter are similar to Case 2, but the battery energy storage is added in a droop mode to mitigate the frequency deviation due to rapid changes in load and/or generation. To demonstrate the impact of an active power drop of the renewable energy resource on the system frequency, the active power of PV array simulator is decreased from 50 kW to 10 kW.

Fig. 50 illustrates the waveform of the voltage of microgrid bus when the PV output drops. In this case, the frequency decreases from 60 Hz to 58.96 Hz, which is less than in Case 2

due to the battery energy storage system, and is within the required IEEE 1547 ranges. The black lines in Fig. 50 show the time-spans during which the frequency is below 59.9.

Fig. 51 shows the active power of diesel generator, battery energy storage system, and PV system when the output of PV array simulator is decreased from 50 kW to 5 kW at t=2' 55", and then is increased to 50 kW at t=3' 59"; in this case, the load is 80 kW. As shown, the battery energy storage system injects active power to the microgrid when the frequency decreases to help the diesel generator to regulate voltage and frequency, mitigating frequency deviations.

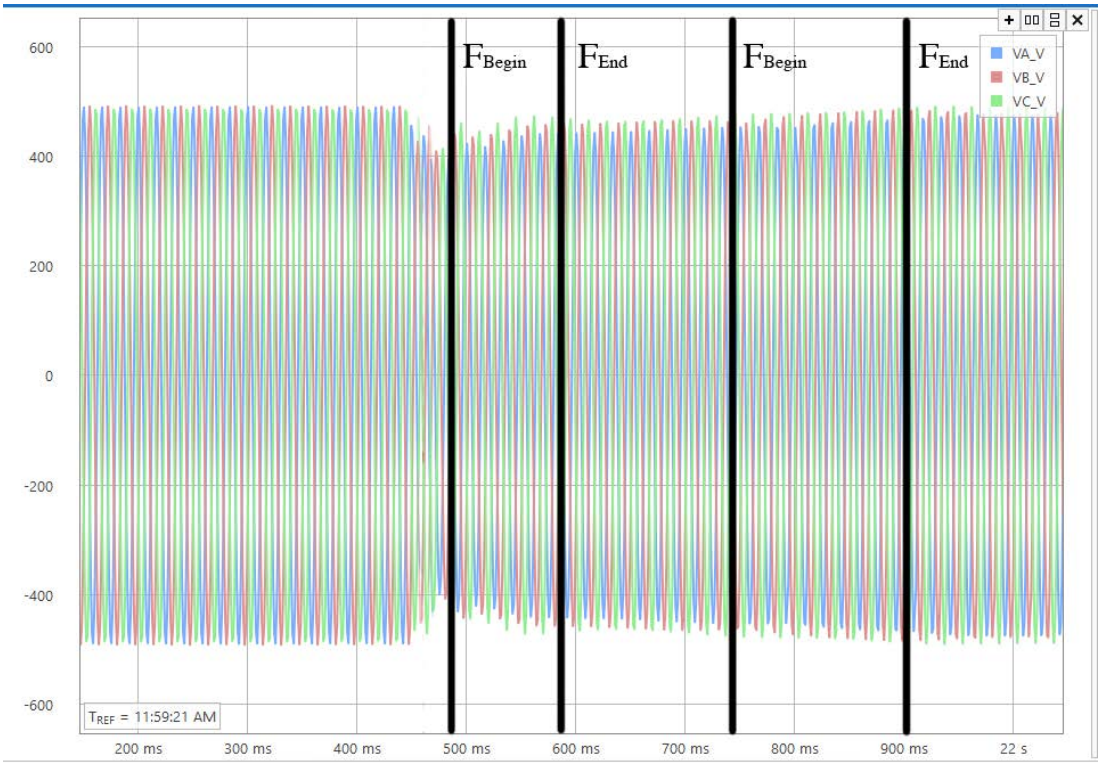

Fig. 50. Voltage waveform of the microgrid bus (in V) with PV, diesel generator, and battery energy storage system for a 40 kW drop in PV output.

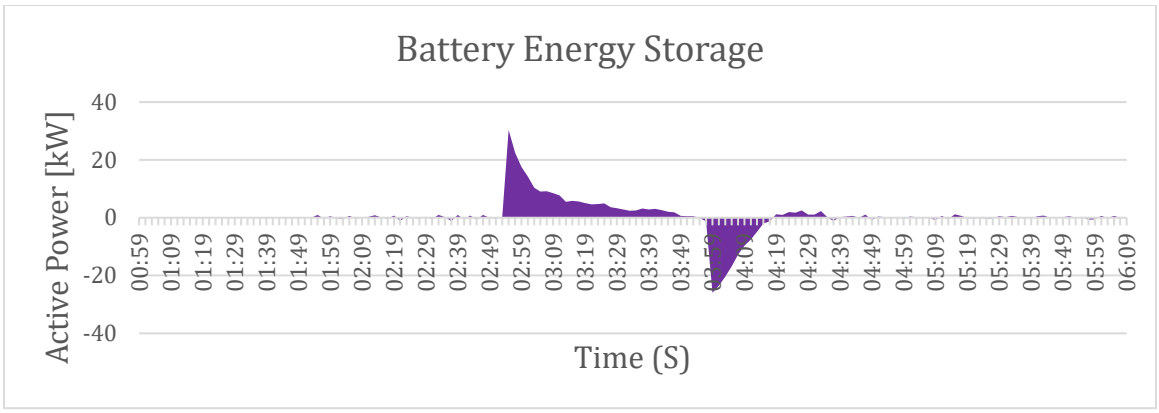

(a)

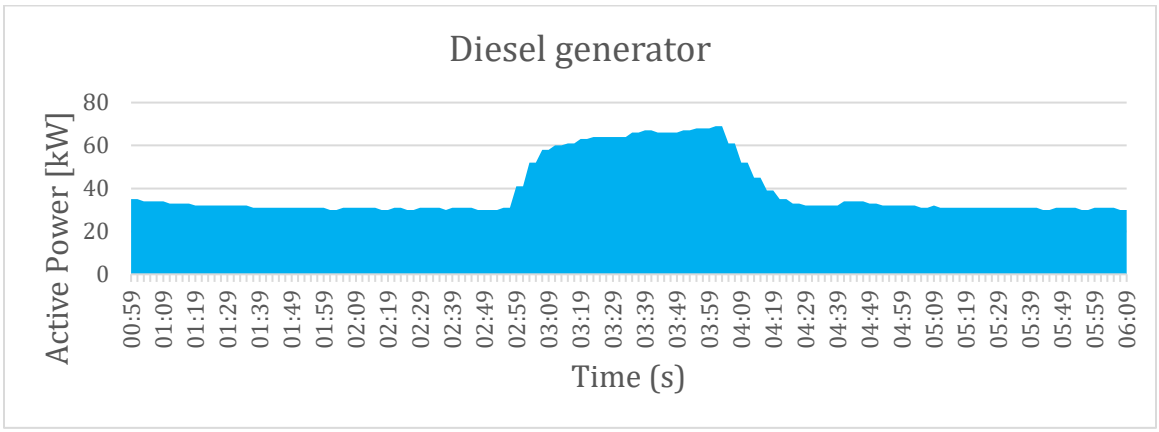

(b)

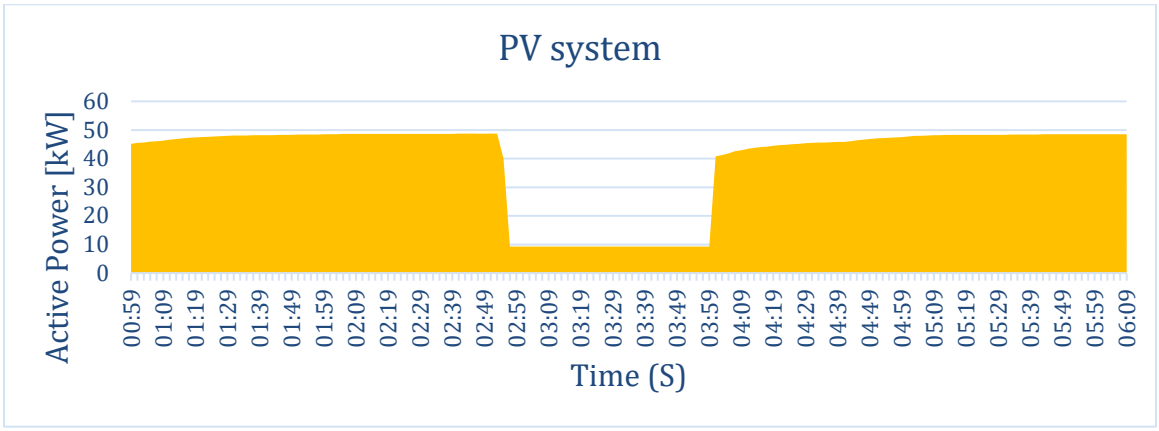

(c)

Fig. 51. Active power of (a) battery energy storage system, (b) diesel generator, and (c) PV system in Case 3.

5.5.2 Synchronization to a weak grid

In this test, the battery energy storage system, and wind simulator inverter are connected to the microgrid bus. The grid simulator is used to represent a weak grid, with the simulator being an inverter-based power supply that emulates the behavior of the grid. The battery inverter is initially in grid-forming mode, while the wind simulator is in PQ mode. A synch-relay is used so that the entire microgrid can synchronize to the grid simulator across the contactor connecting these two systems. This ensures that the grid simulator cannot connect to the microgrid with a different voltage, frequency, or phase. In this case, when the voltage, frequency, and angle of the microgrid bus and the grid simulator are matched, the contactor is closed and the mode of battery energy storage is changed from grid-forming to the PQ mode. The wind simulator inverter should stay online during the synchronization process. If inner loop controllers are not properly tuned for synchronization to a weak grid, there is a slightly phase deviation during the synchronization that results in the inverter in PQ mode not being able to synchronize and thus tripping. The wind inverter is running in PQ mode (P =0 kW), the battery inverter is running in grid-forming mode, and there is no load; then, the microgrid bus is synchronized to the grid simulator, with the battery inverter mode changing from grid-forming to PQ mode.

Fig. 52 shows the voltage and current of the wind simulator during the synchronization process. Note that the output of wind simulator is slightly more than zero due to transformer losses. Observe that the wind simulator cannot stay online due to the overcurrent trip during the synchronization process. A similar test for synchronization of the microgrid to a stiff grid does not result in synchronization loss. This is an example of Control System Stability, as the inner loop controllers are not properly tuned for synchronization to a weak grid, resulting in phase deviation during the synchronization.

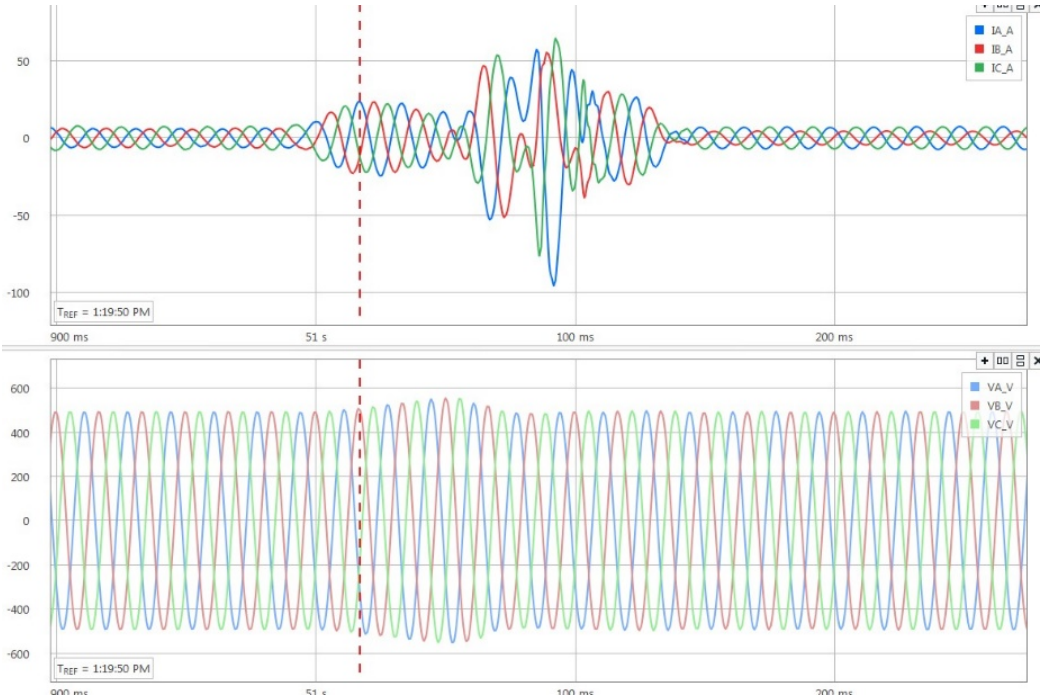

Fig. 52. Voltage (V) and current (A) waveforms at the wind simulator for the synchronization of the microgrid to a weak grid.

5.5.3 Transformer Energization

The switching of breakers and energizing of transformers in inverter-based microgrids can result in the loss of the entire system. Since the maximum current contribution capability of the inverter-based DERs are limited compared to synchronous machine-based DER, the grid-forming units should be properly sized for inverter-based microgrids. In this test, the battery energy storage is in grid-forming mode and is connected to the microgrid bus; the rated power of the battery inverter is 200 kW. Since there is no load connected to the microgrid bus, the inverter output power is zero. Then, the breaker of the wind turbine simulator transformer (112.5 kVA, 480V/600V) is closed.

Fig. 53 shows the voltage and current waveforms of the battery energy storage during the switching of the transformer. Although the rated power of the battery inverter is two times greater than the rated power of transformer, the battery inverter trips due to its overcurrent protection. Inverters can generally contribute in-rush currents from 1.2-1.5 pu of their rated powers. It should be mentioned that there are various techniques to energize the transformers to reduce in-rush currents; thus, proper attention should be paid in the design of inverter-based microgrids and the procedures to energize transformers. This is an example of Power Supply and Balance Stability, and in particular Voltage Stability.

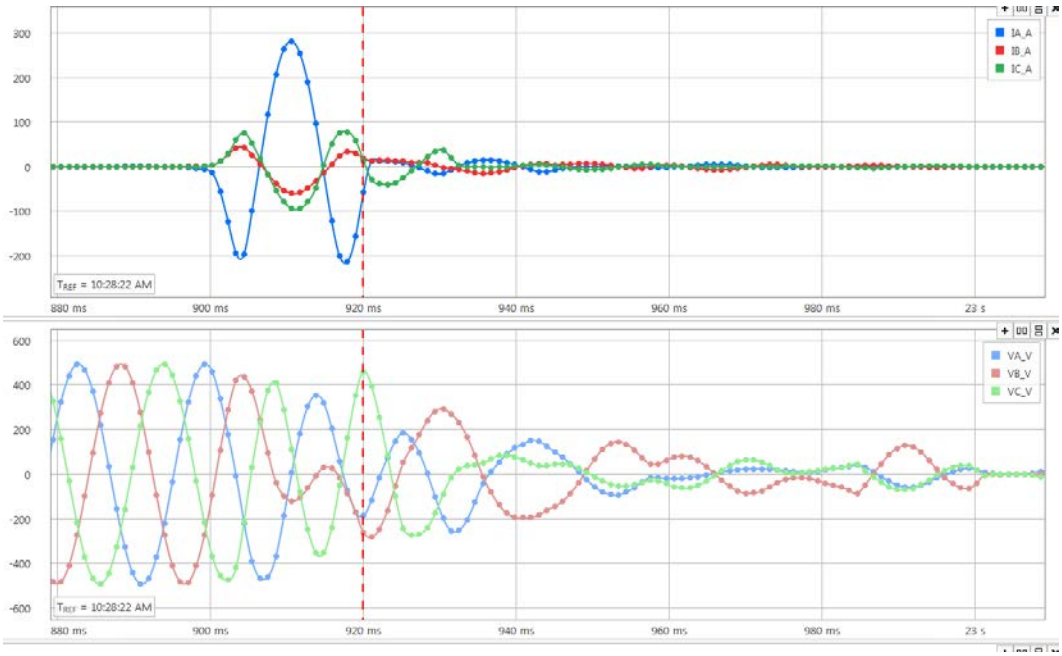

Fig. 53. Voltage (V) and current (A) waveform of battery energy storage during energization of a transformer.

5.6 Impact of Load Dynamics

In order to compare the characteristics of different load types (e.g., static loads, DOL loads, VSD loads), a three-phase short-circuit fault was simulated on the microgrid shown in Fig. 54, which comprises a total load of 60 kW, with each load type having equal capacity, i.e., 20 kW for each static, DOL and VSD loads. The static load is represented by a ZIP load model with a 0.85 lagging power factor, and has equal proportion of constant current, power, and impedance load. The DOL motor load is represented by a fan load, and the VSD motor load is represented by a pump load. Initially, the microgrid is operated in grid-connected mode, but does not exchange active power with the main grid. The solar PV system generates 35 kW, the diesel generator generates 20 kW, and the battery energy storage system injects 5.5 kW to maintain the power balance in the microgrid.

Fig. 55 represents the active and reactive power for each load type, following a 150 ms three-phase short-circuit fault, with a fault impedance of 0.1+ j 0.1 pu at the microgrid 400 V busbar during grid-connected and islanded modes. Observe that the different load types result in substantially different system responses during the short-circuit fault. Both the static and DOL motor loads' active and reactive power consumption substantially decrease

during the fault, and recover rapidly following fault clearance. However, unlike the static load, the DOL motor load requires substantial reactive power during the recovery phase, i.e., three times the rated reactive power, even though limited by a soft-starter; this would affect the overall stability of the microgrid. The VSD motor load is less affected in grid-connected mode, and maintains almost the same active and reactive power consumption. However, in islanded mode, the VSD motor load trips due to commutation failure at the front-end rectifier [139], resulting in active and reactive power decreasing to zero, as shown in Fig. 55(c).

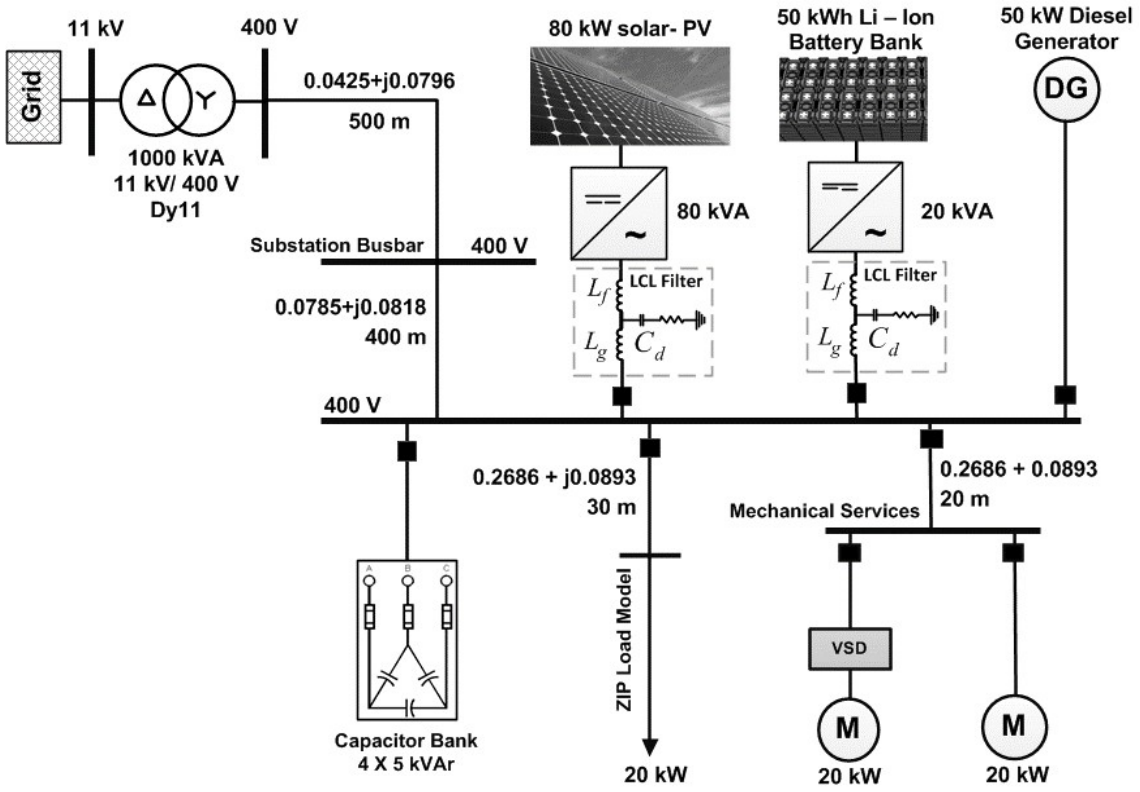

Fig. 54. Microgrid test system for dynamic load studies.

Fig. 56 illustrates the various loads' dynamic responses following a 12 kW load switching event, (20% load increase) in the microgrid for grid-connected and islanded modes. All three load types have negligibly affected during the load switching event when operating in grid-connected mode; however, in islanded mode, 0.05% - 5% oscillations are observed in all three load types. This example shows the importance of the load characteristics for microgrid stability.

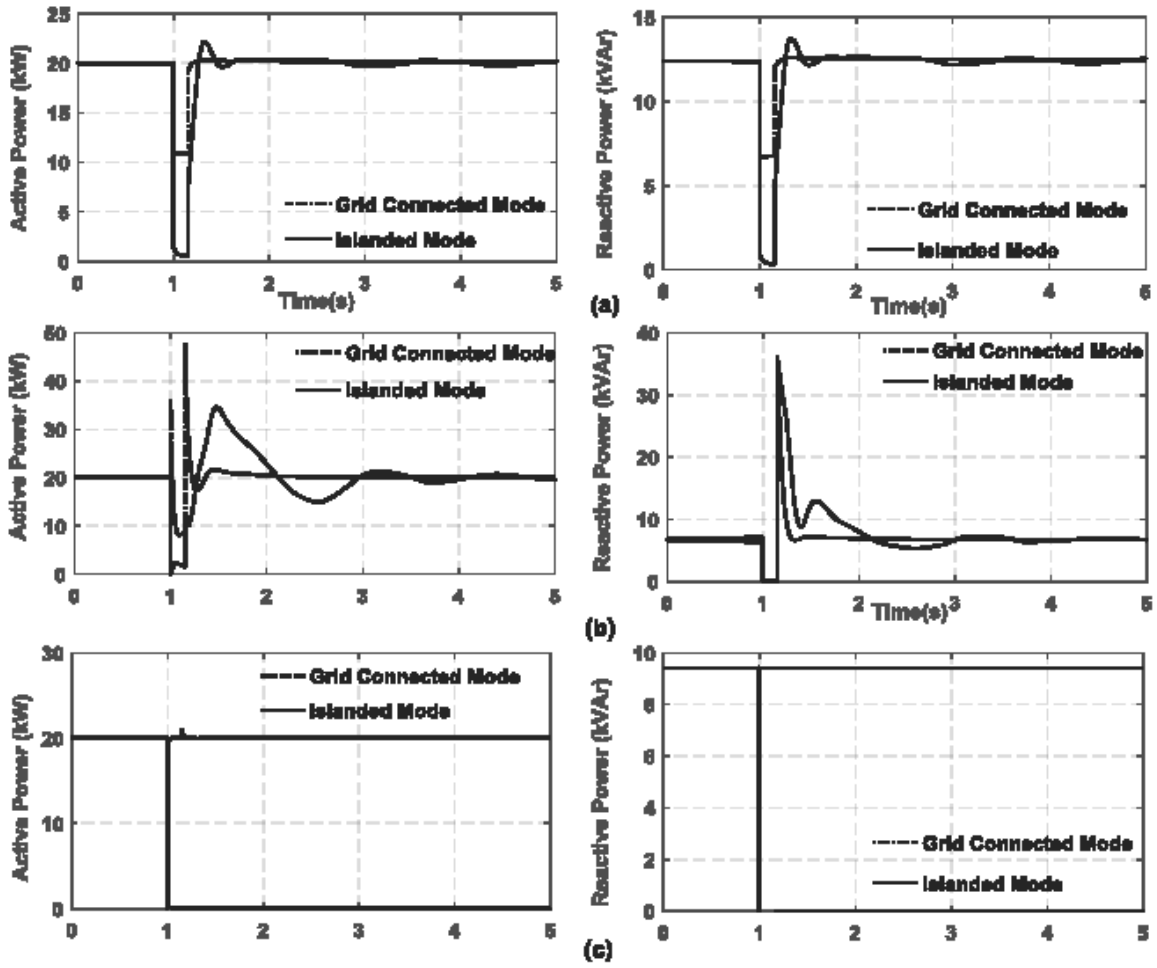

Fig. 55. Dynamic characteristics of different load types during a fault in a microgrid: (a) static (ZIP) load, (b) DOL motor load, and (c) VSD motor load.

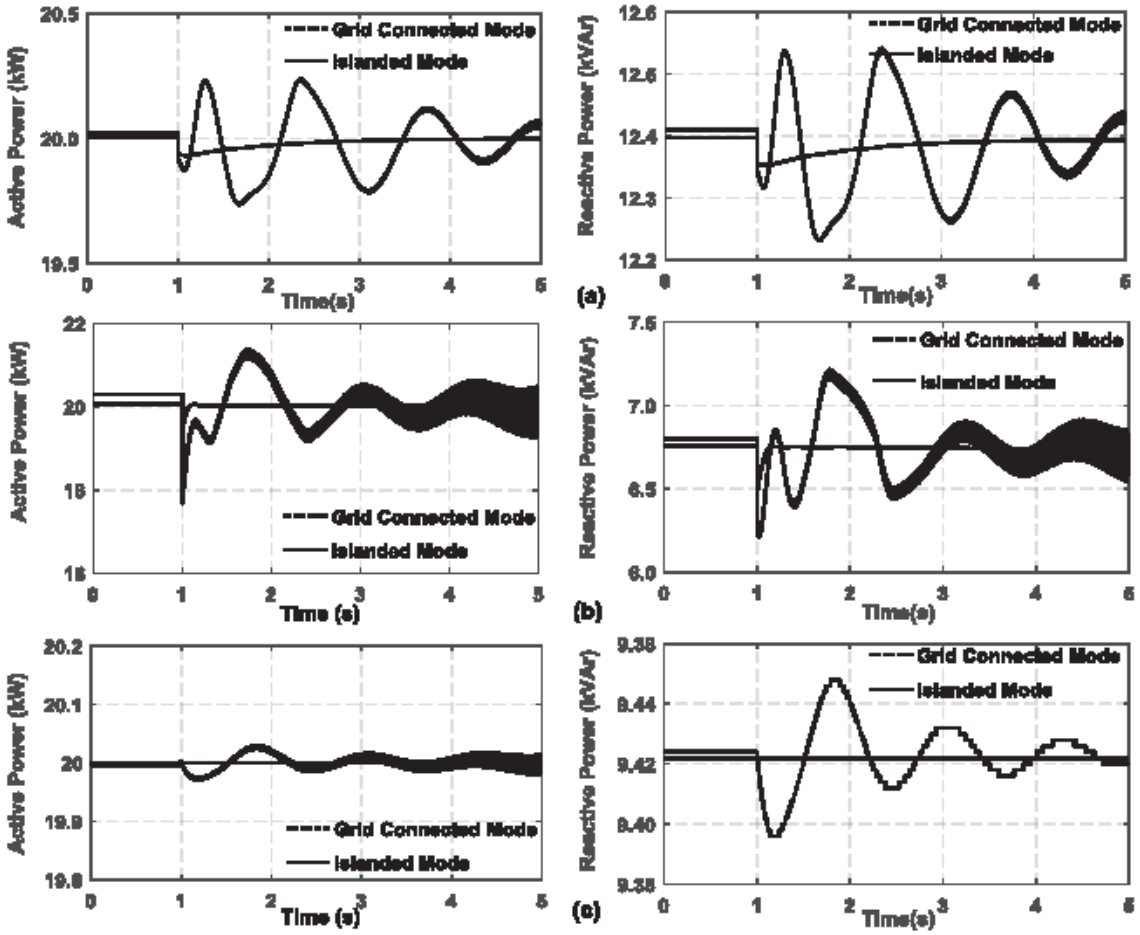

Fig. 56. Dynamic response of different load types during a 20% load switch event.

5.7 Virtual Inertia Mitigation Techniques

Virtual (Synthetic) inertia has been widely proposed in the literature as a solution for low inertia issues. Some of the most popular topologies involve a synchronverter [140], Virtual Synchronous Machines (VISMA) [141], Ise Lab's topology [142], Synchronous Power Controllers (SPC) [143], VSYNC topology [144], virtual oscillator control [145], and others. Droop controllers used in parallel operation of DERs have also been shown to provide virtual inertia under certain conditions [146]. The basic concept is the same in all of these techniques, with the aim of replicating inertial response through control algorithms and power electronic converters [69]. The required energy can be obtained through ESS or curtailed operation of DERs. One of the basic requirements of these systems is that they

operate autonomously and quickly (from a few cycles to less than 10 s) to counter-act the fast decay of frequency in low-inertia microgrid systems.

Fig. 57 shows a typical configuration of a virtual-inertia system, with the virtual-inertia algorithm at the core of the system. The controller senses the frequency of the system typically using a PLL. Based on the frequency measurements and its rate-of-change, power references can be generated for the inverter as follows:

$$P_{VI} = K_D \Delta\omega + K_I \frac{d\Delta\omega}{dt} \tag{48}$$

where $\Delta\omega$ and $d\Delta\omega/dt$ are the change in frequency and its Rate of Change (ROCOF). K_D and K_I are the damping and the inertia constants, respectively.

More sophisticated control approaches like the synchronverter, VSIMA, SPC, etc., try to mimic the exact dynamics of a synchronous generator either through detailed equations or some kind of approximation. Virtual-inertia algorithms are already implemented in commercial inverters; however, certain challenges still remain in the integration of virtual-inertia systems in the context of microgrids. Improved control design, aggregation of multiple virtual inertia units and energy usage minimization are a few of the challenges that need to be addressed [147].

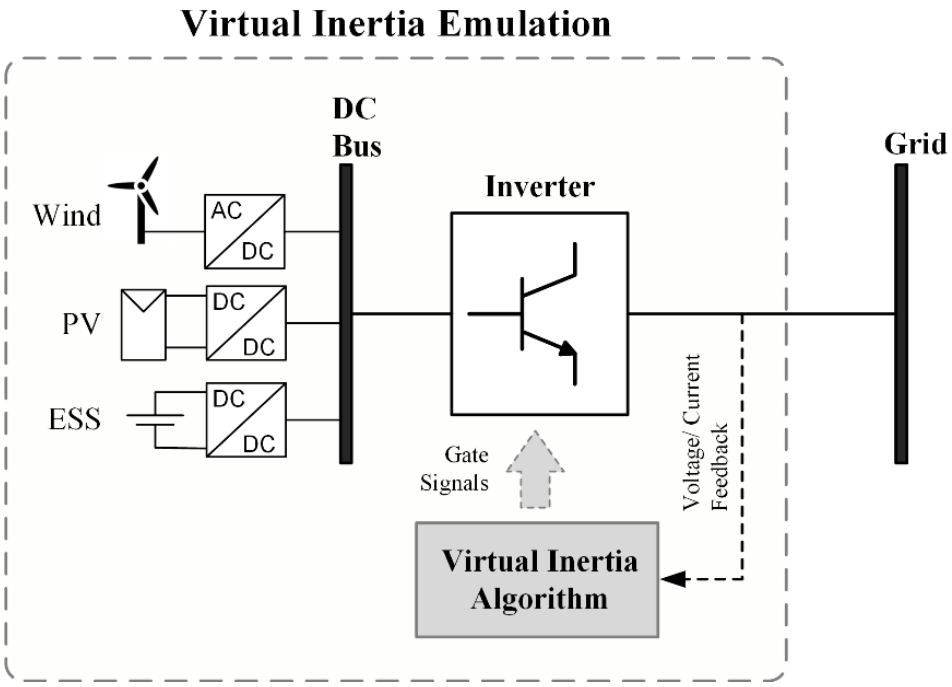

Fig. 57. Virtual-inertia using a power electronic converter.

5.7.1 Benchmark PV-Hydro Microgrid System

To demonstrate the impact of high renewable penetration in the frequency stability of microgrids, a PV-hydro benchmark system, introduced in [68], is used here. This benchmark system consists of a 39 kVA hydro generator and a 25 kWp PV system, as shown in Fig. 58. The hydro unit was adapted from the remote village of Bhujung in Nepal, scaling it to match the PV installation at the South Dakota State University (SDSU) Microgrid Research laboratory. The microgrid is a three-phase system operating at 208 V with a rated frequency of 60 Hz. The PV is modeled using current sources with no inertial response, whose magnitude depends on the available solar irradiance. High penetration of intermittent PV in such systems can lead to frequency stability, as fast changes in PV generation cannot be absorbed by the relative low inertia of the small-hydro system.

The test system was analyzed using a 250 s snapshot of real irradiance data, as shown in Fig. 59. The frequency variations were obtained for three different levels of PV penetration, i.e., 10, 15, and 25 kWp, as shown in Fig. 60. Large frequency variations outside the ISO8528 recommended limits for generators [148] can be observed; with increased PV penetration, the magnitude of the frequency excursions are much higher. The ROCOF are extremely high (as high as 4.8 Hz/s for 25 kWp penetration). This affects the frequency stability of the system, since such conditions can trigger frequency relays leading to cascading failures of generation units in a microgrid.

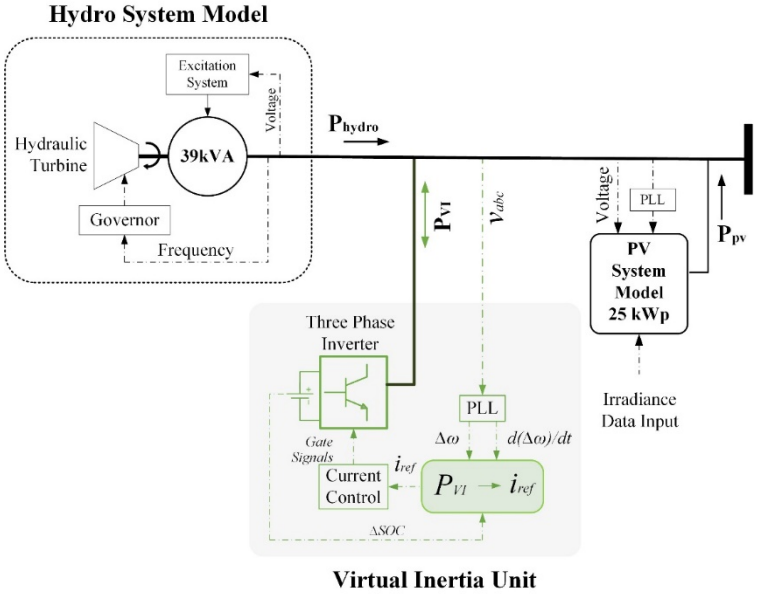

Fig. 58. Virtual-inertia unit implemented in a benchmark PV-hydro microgrid system.

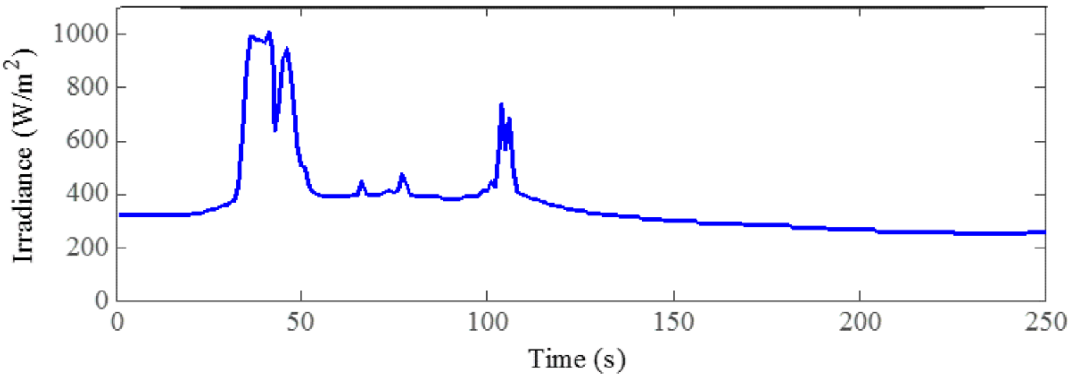

Fig. 59. Snapshot of irradiance data for July 19, 2012 (sampling rate is 1 s).

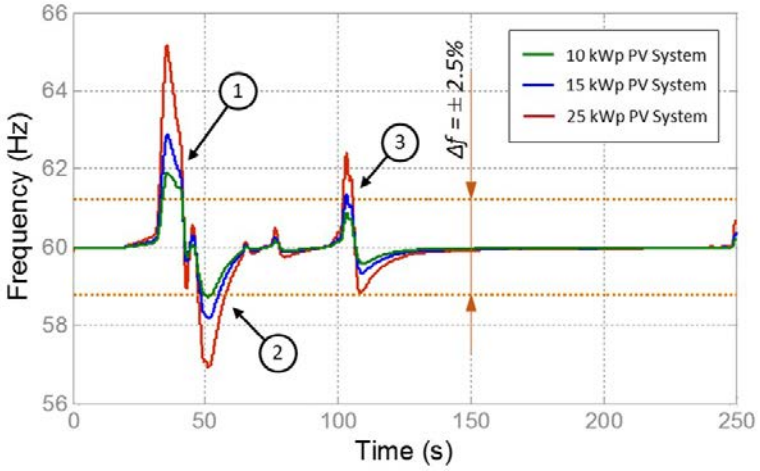

Fig. 60. Frequency variations observed in the PV-hydro benchmark system for PV penetration levels of 10, 15, and 25 kWp.

Simulations are then performed with a dedicated inverter emulating virtual inertia installed in the system, as shown in Fig. 58. The frequency of the system for 25 kWp PV penetration after addition of virtual inertia is shown in Fig. 61 with solid lines. The reduction in the ROCOF and the frequency excursions are summarized in Table 8. The maximum and minimum frequency excursions can be reduced by 6.3% and 4.7%, respectively; similarly, the maximum ROCOF can be reduced by as much as 85.4%. After the addition of VI, both the frequency and its rate of change are within the permissible limits.

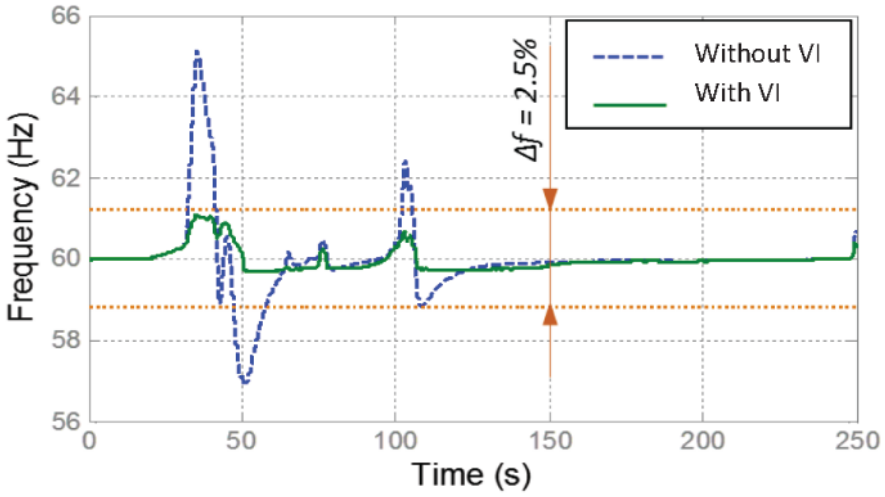

Fig. 61. Reduction in frequency deviations in the PV-hydro benchmark with virtual inertia unit.

TABLE 8. Comparison of Frequency Variation and ROCOF With and Without Virtual Inertia

	Without Virtual Inertia	With Virtual Inertia
Minimum Frequency	56.9 Hz	59.6 Hz
Maximum Frequency	65.1 Hz	61.0 Hz
Maximum ROCOF	4.8 Hz/s	0.7 Hz/s

5.8 Isolation and reconnection of a microgrid

One of the desired features of a microgrid is its capability of disconnection from and re-synchronization to a larger grid, in cases such as faults and intentional islanding. In this example, a small perturbation stability analysis of pre- and post-isolation shows how the system could become unstable.

The microgrid under study is shown in Fig. 62, where two inverter-interfaced DERs feed local loads, with the possibility of grid connection through a static switch. The microgrid model includes realistic distribution line parameters, as well as coupling transformers for each DER. The parameters are summarized in Table 9. The DER model is shown in Fig. 2 with LCL filters, average model for the VSC (as in Fig. 6), and traditional low-pass-filtered frequency droop control (voltage droop control is neglected for simplicity).

TABLE 9. Parameters for Microgrid Components

Parameters	Value	Units
Nominal frequency (f_0)	60	Hz
DERs rated power ($P_{1,2}$)	10	kW
DERs rated phase voltage ($V_{1,2}$)	120	V
DERs resistance ($R_{1,2}$)	0.0188	Ω
DERs inductance ($L_{1,2}$)	0.62	mH
Filter inductance (L_f)	0.3379	mH
Filter capacitance (C_f)	53.2544	μF
Filter resistance (R_f)	0.026	Ω
DER 1 power set-point (P_{10})	545.8	W
DER 2 power set-point (P_{20})	-569.5	W
Transformer series reactance (X_t)	0.0481	Ω
Transformer series resistance (R_t)	0.0481	Ω
Feeder 2 reactance (X_{Z2})	0.00064	Ω
Feeder 2 resistance (R_{Z2})	0.0049	Ω
Feeder 3 reactance (X_{Z3})	0.0072	Ω
Feeder 3 resistance(R_{Z3})	0.0547	Ω
Feeder 4 reactance (X_{Z4})	0.0024	Ω
Feeder 4 resistance(R_{Z4})	0.0182	Ω

Using dynamic phasor modeling [149], a small-perturbation stability study is carried out on this microgrid, showing that when the droop gains are arbitrarily modified, the behavior of the microgrid for islanded and grid-connected conditions is rather different. The system eigenvalues for the islanded case are shown in Fig. 63, for a droop gain of the DER 1 between 5% to 20%, while maintaining the droop gain of DER 2 at 5%. Observe that the system is stable at all droop gains; the results of sweeping the droop gain of DER 2 are

similar, but not shown here. The system eigenvalues for the grid-tied case are shown in Fig. 64, for the same droop gains; note that, in this case, the system becomes unstable for droop gains above 16%.

The results of this study are verified by a time-domain simulation of the microgrid model in Fig. 62. The model considers grid islanding and re-synchronization throughout the simulation. Thus, Fig. 65 illustrates the case of microgrid islanding, when the droop gains of DERs 1 and 2 are at 5%. Observe that, when the static switch is opened at $t = 10$ s, the microgrid transits into an island seamlessly, with a reduction in frequency due to the droop control, and the power of the impedance load being reduced due to the voltage drop. It is worth noting that, before islanding, both DERs feed power equal to their set-points, with grid feeding the load and part of the microgrid losses. After the transition, both sources feed the load according to their power and frequency set-points, with a frequency drop of 0.3 Hz. As Figs. 63 and 64 illustrate, on both states the microgrid is stable.

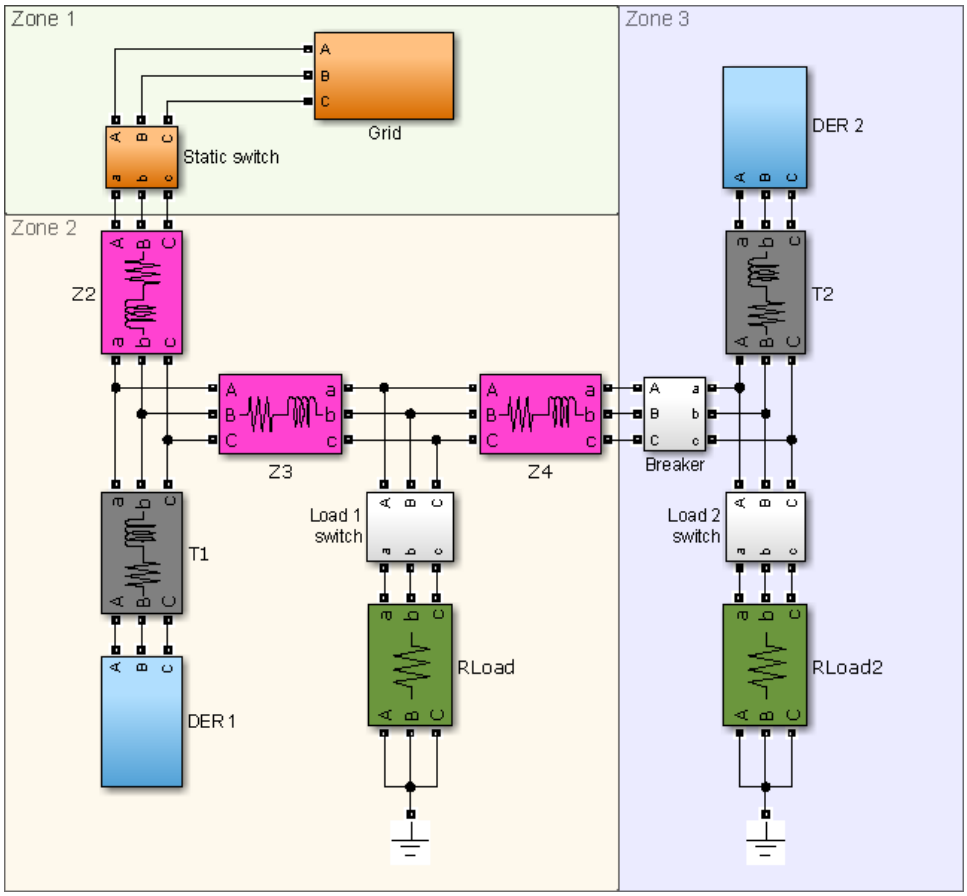

Fig. 62. Simulation model of a microgrid for islanding and synchronization analysis.

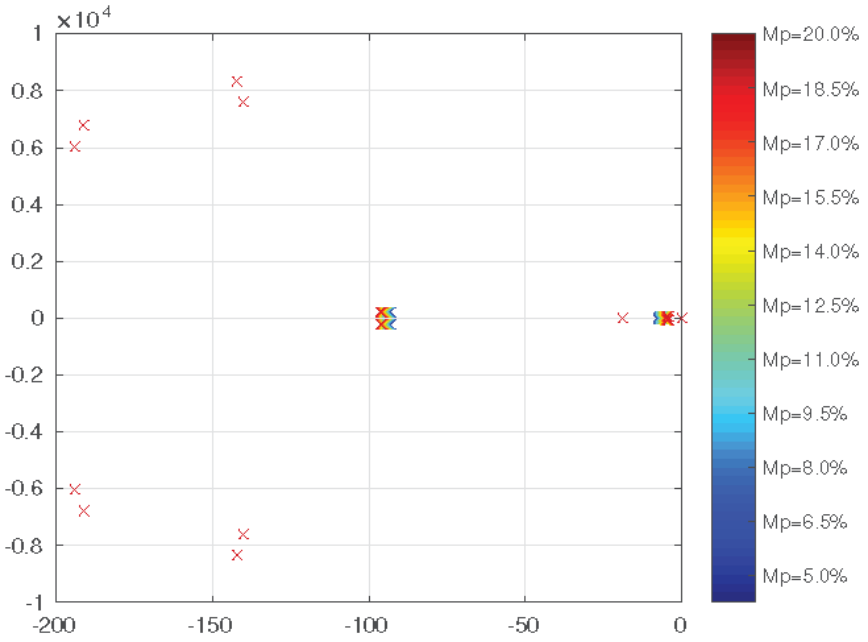

Fig. 63. Eigenvalues of the islanded microgrid, stable case.

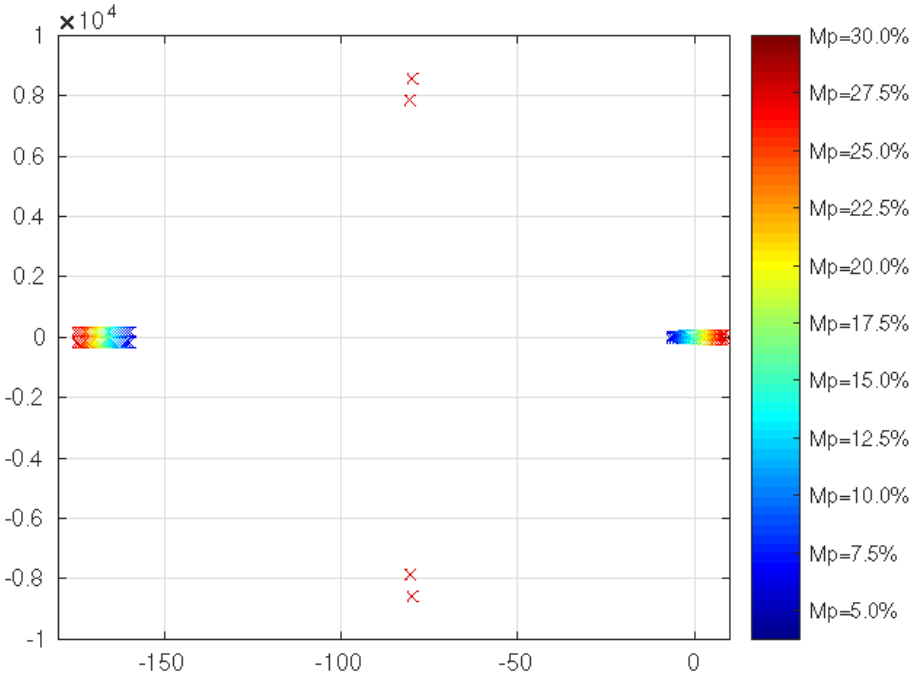

Fig. 64. Eigenvalues of the grid-connected microgrid, unstable case.

Fig. 66 shows the microgrid re-synchronization process starting at t = 15 s. Observe that the microgrid presents poor oscillation damping, but otherwise the synchronization is stable. The droop gains of the DERs are again at 5%, thus ensuring stability. This particular results are an example of Power Supply and Balance Stability, since both inverters are tuned similar, and oscillations arise from poor power sharing between the DERs rather than a poorly tuned inverter.

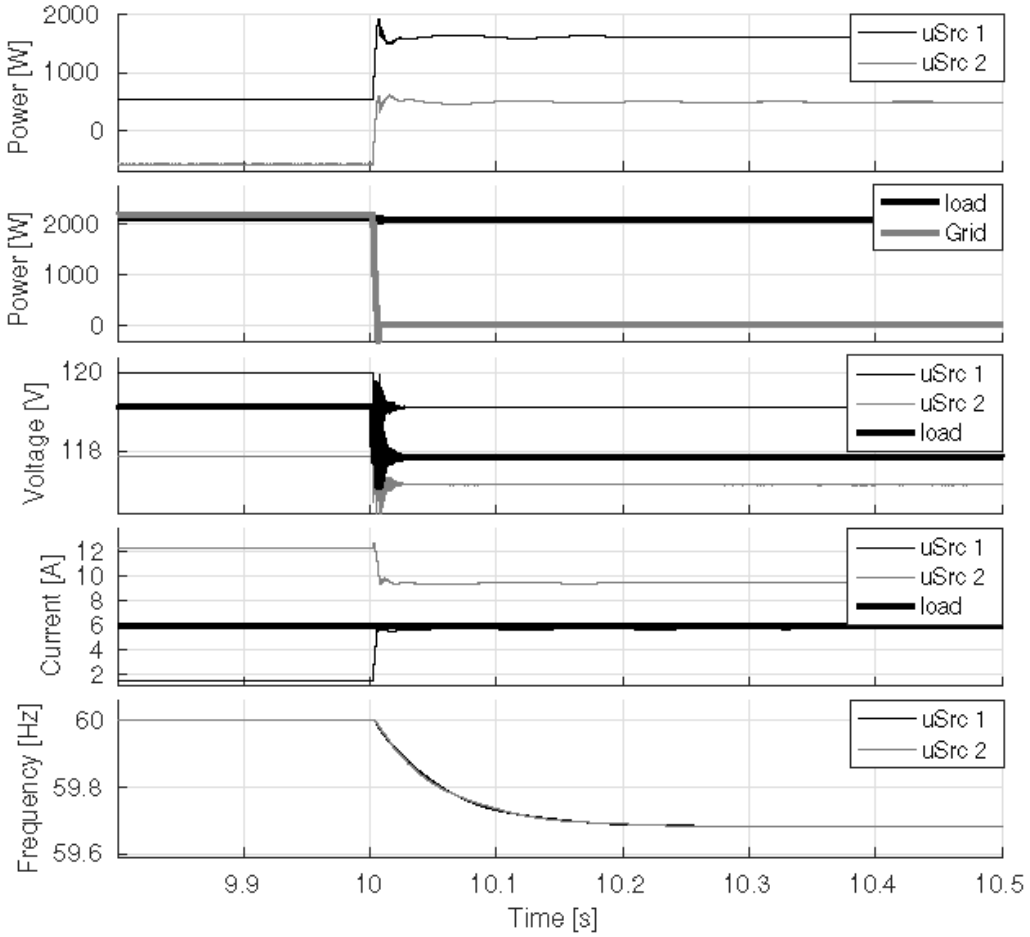

Fig. 65. Simulation results for microgrid islanding: stable case.

Fig. 67 illustrates the case of the microgrid in grid-tied mode, with the droop gain of DER 1 being increased from 5% to 20% at t = 20 s. As expected from the eigenvalues shown in Fig. 64, the system is unstable in this case. The time-domain simulation shows that before t = 27 s, the power and frequency waveforms of DER 1 and the grid show sustained oscillations until t = 27 s, when the static switch is opened and the microgrid is islanded, reaching stable operation after a few seconds, which is expected from the eigenvalues

depicted in Fig. 63. This is an example of Control System Stability, since the droop gain of one individual inverter, is unrealistically high, i.e., it is poorly tuned for grid-tied operation.

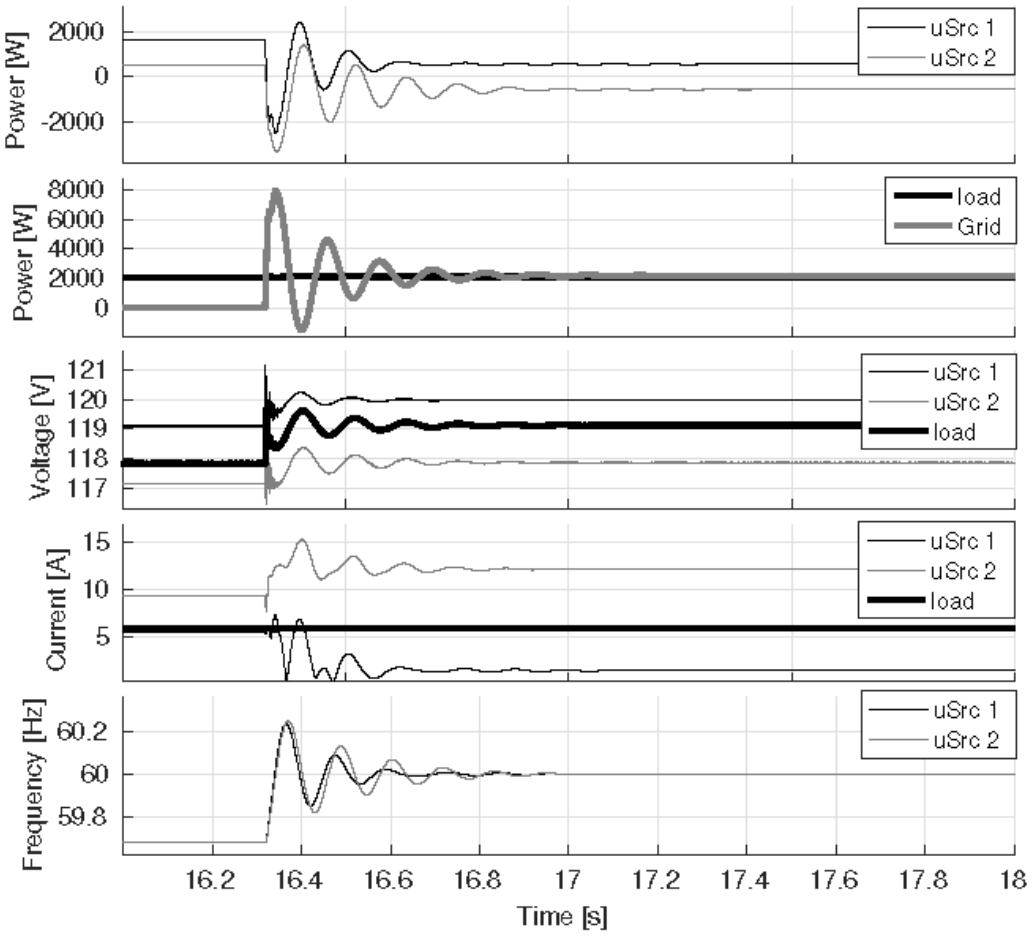

Fig. 66. Simulation results for grid synchronization: stable case.

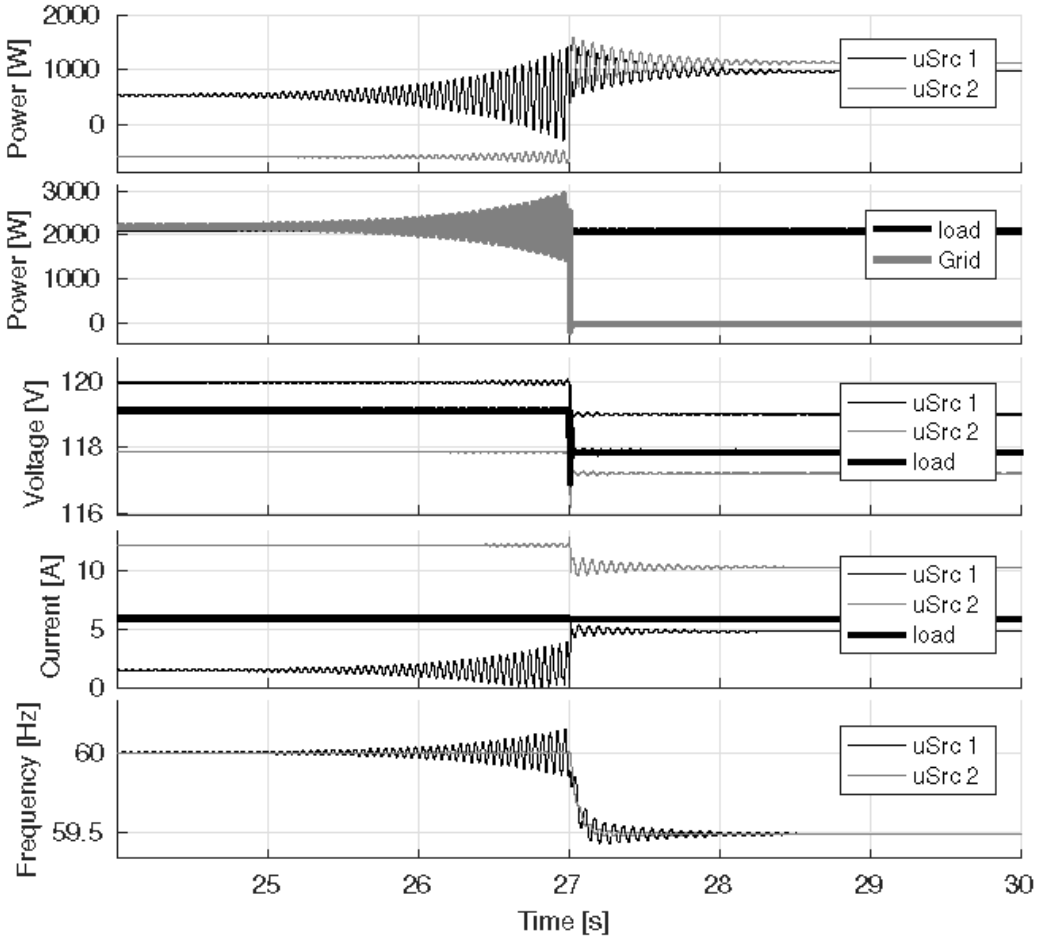

Fig. 67. Simulation results for grid synchronization: unstable case.

5.9 Alaska Power System Integration Laboratory Examples

The Alaska Center for Energy and Power (ACEP) Power Systems Integration (PSI) laboratory is a hardware and software-based research facility designed to investigate and test renewable energy and energy storage integration schemes for Remote Islanded Microgrids (RIMs). The laboratory houses a 500 kW test bed consisting of a 320 kW diesel generator with a programmable controller, 100 kW wind turbine simulator, 100 kW PV simulator, 1000 Ah battery bank, 325 kW inverter, two 250 kW digitally-controlled RL load banks, and distributed control and data acquisition infrastructure. A one-line diagram of the ACEP PSI laboratory test bed is shown in Fig. 68.

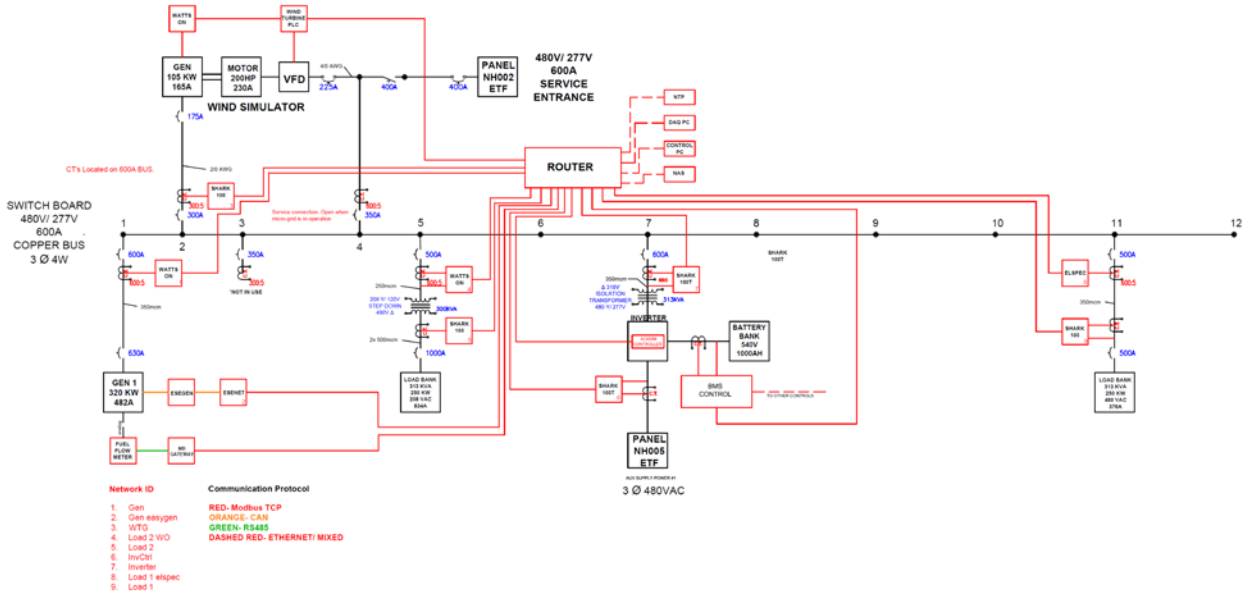

Fig. 68. One-line diagram of Alaska Center for Energy and Power's Power System Integration Laboratory microgrid test bed.

Two key features of the PSI laboratory for testing RIMs with high penetration of renewable energy are the inverter and distributed controllers. The inverter can operate in grid-forming and grid-following mode, and the local diesel controller can switch in real-time between isochronous and droop mode to follow the inverter. The inverter with distributed controls and battery bank allow for the system to transition between high penetration renewable-diesel mode and diesel-off (renewable only) mode. This, combined with capabilities of the digitally-controlled RL load banks with minimum steps of 5 kW and 1 kVAR, provides a platform for testing the stability of the system under a number of loading and renewable penetration scenarios.

A simulation model of the PSI laboratory in wind-diesel mode, as depicted in Fig. 69, was developed and validated with measurements to study frequency stability of RIMs under various levels of wind penetration and load conditions [150]. This model was further enhanced to investigate the use of distributed secondary load control for frequency stability in high penetration wind-diesel mode [151]-[153]. Examples from these studies are provided next.

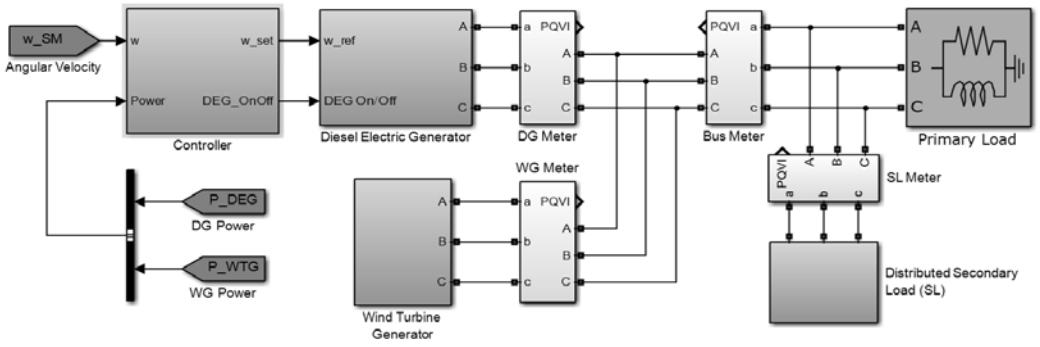

Fig. 69. Model of the Power System Integration Laboratory (PSI) microgrid test bed in wind-diesel mode with a distributed secondary load controller.

5.9.1 Modeling Issues in Wind-Diesel Microgrids

Actual measurements and simulation results of system voltage, frequency, and current taken from the PSI microgrid system and its model in diesel-only with a load transition are shown in Fig. 70. The same variables in wind-diesel mode at three different wind penetration levels are illustrated in Figs. 71-73. While the modelled frequency shows typical responses, the measured frequency shows both usual and unusual response characteristics. Thus, observe the differences in magnitude, peak time, and settling time of the responses, particularly in the diesel-only case under medium-high load transitions (Fig. 70). The difficulty with the diesel model is in tuning the diesel engine speed controller and accurately modelling its inertial response; in this case, the diesel engine is simply modelled as a time delay. Note in Figs. 71-73 that the frequency response to a low penetration wind transient is more accurately modelled than a medium-high penetration wind transient. In this case, the inverter in grid-following mode is assisting in providing P and Q in tandem with the diesel operating in isochronous mode. These studies shown the importance of proper modeling of the microgrid components, especially under high RE penetration, as discussed in Section 4.

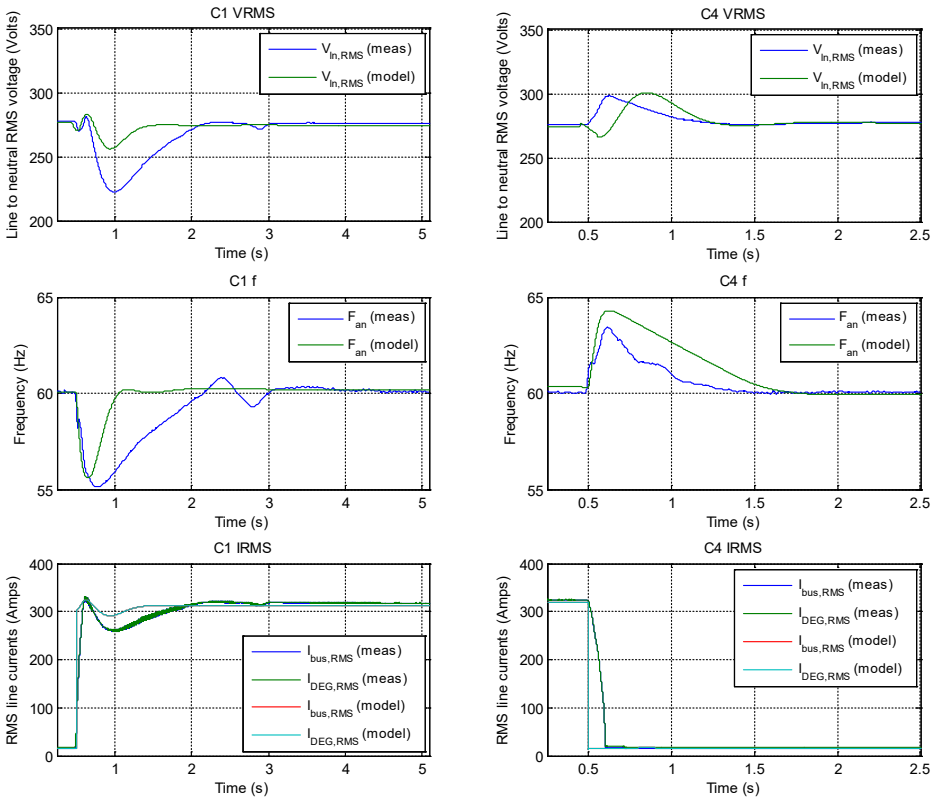

Fig. 70. Plots comparing measured and modelled voltage, frequency, and current for a 250 kW load increase (left) and a 250 kW decrease (right) for diesel-only mode (power factor = 1.0).

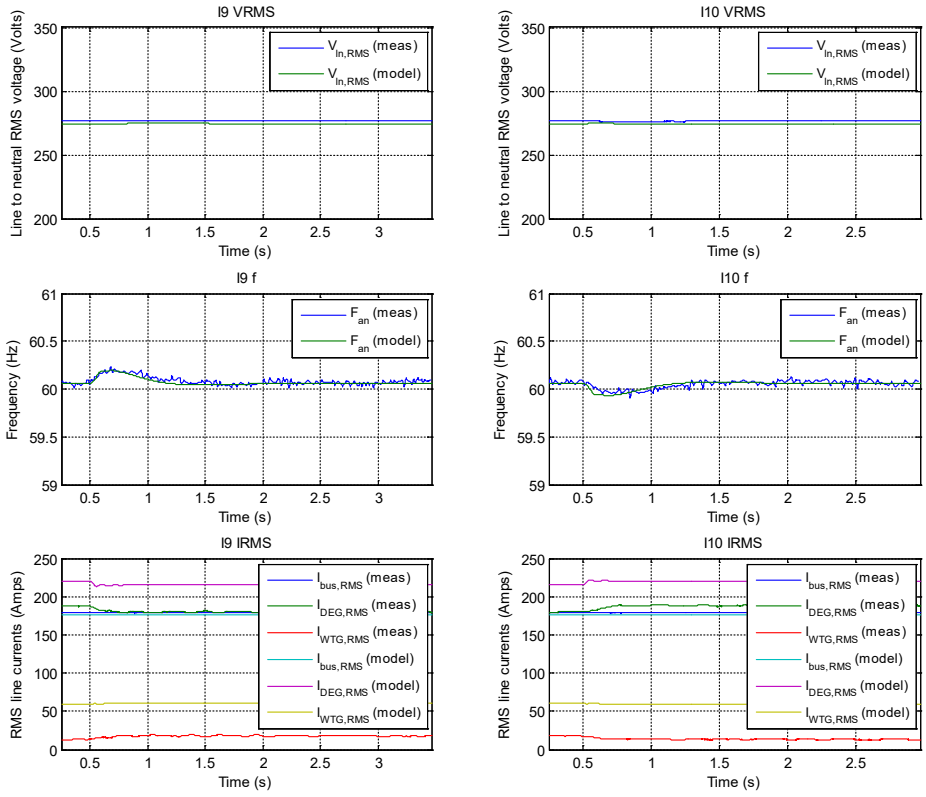

Fig. 71. Plots comparing measured and modelled voltage, frequency, and current for a 10 kW wind generation increase (left) and a 10 kW decrease (right) with low penetration, and a 100 kW load in wind-diesel mode (power factor = 0.8 lagging).

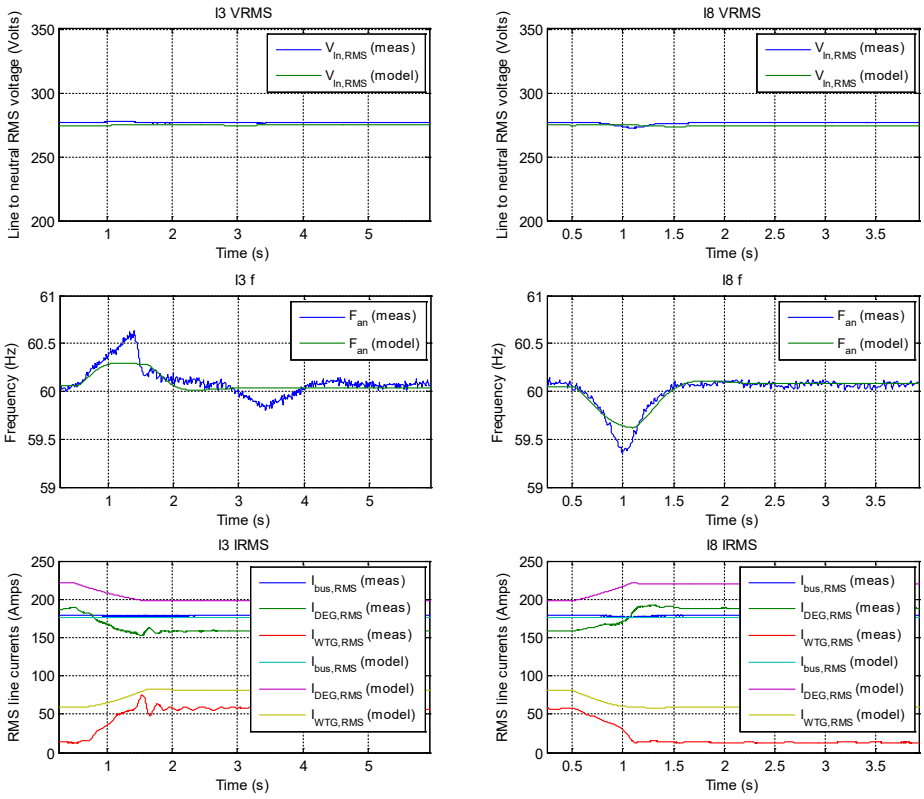

Fig. 72. Measured and modelled voltage, frequency, and current for a 45 kW wind generation increase (left) and a 45 kW decrease (right) with medium penetration, and a 100 kW load in wind-diesel mode (power factor = 0.8 lagging).

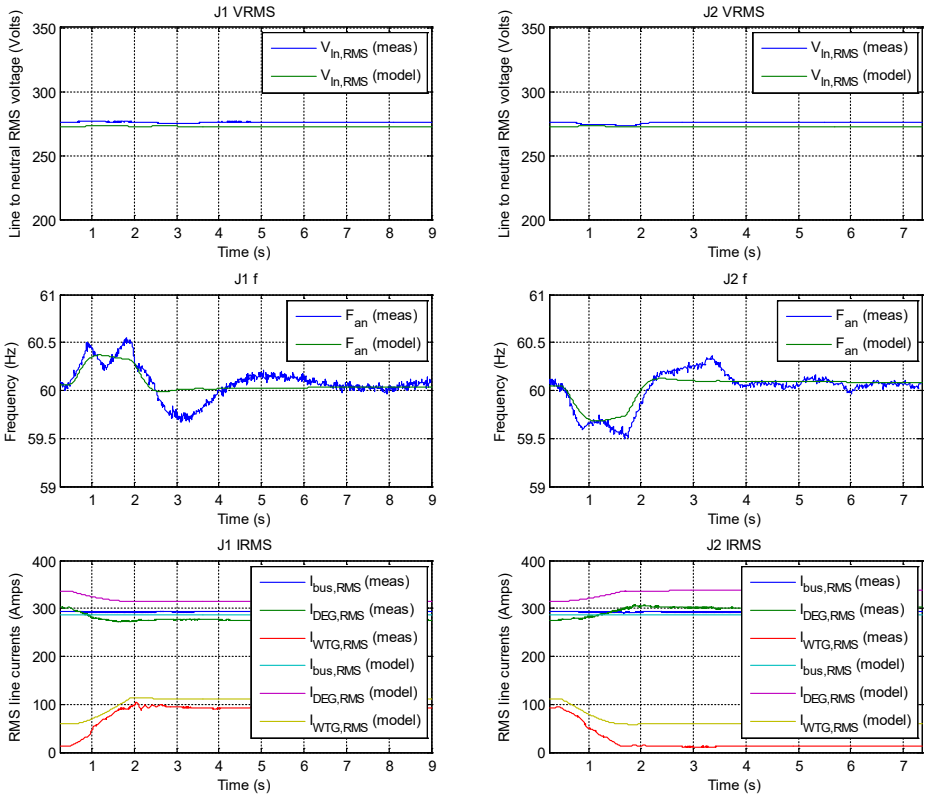

Fig. 73. Measured and modelled voltage, frequency, and current for a 75 kW wind generation increase (left) and 75 kW decrease (right) with medium-high penetration, and a 100 kW load in wind-diesel mode (power factor = 0.8 lagging).

5.9.2 Distributed Secondary Load Control

In wind-diesel RIM systems, a centralized secondary load controller is typically used to buffer wind generation and demand events. While a central dump load or electric hot water tank is often used for this purpose, the excess energy from the wind can be stored using distributed electric thermal loads with autonomous controls. In this case, each electric thermal load has a PI controller that uses the frequency of the load current to actuate four load steps in proportion to increases in frequency above 60 Hz during wind events. Simulations using the model of the PSI wind-diesel system with distributed secondary load control for a ramp-up/ramp-down wind profile and for a synthesized dynamic wind profile are shown in Figs. 74 and 75, respectively.

In Fig. 74, a transition can be observed from diesel-only mode with decrease in the primary load from 75 kW to 50 kW, to wind-diesel mode with a ramp-up wind profile, until the

diesel reaches its Minimum Optimal Load (MOL) and distributed secondary load control is actuated. The diesel operates in isochronous mode, controlling frequency and voltage with the inverter in grid following mode (WD-Low). The diesel switches to droop mode after its output power drops below the 50 kW MOL (WD-High). The system then transitions to wind-only mode once the power consumed (16 kW here) by the synchronous generator, now operating as a synchronous condenser, equals the difference between the power output of the diesel and wind generator.

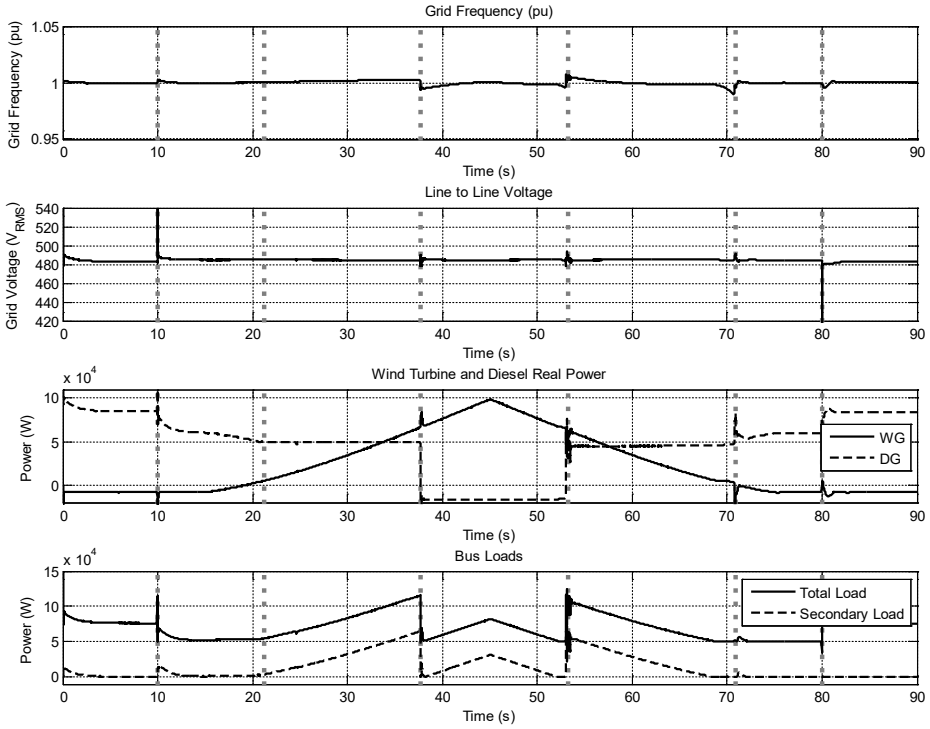

Fig. 74. System frequency, voltage, power generation, and load for a ramp-up/ramp-down wind profile using autonomous distributed secondary load control.

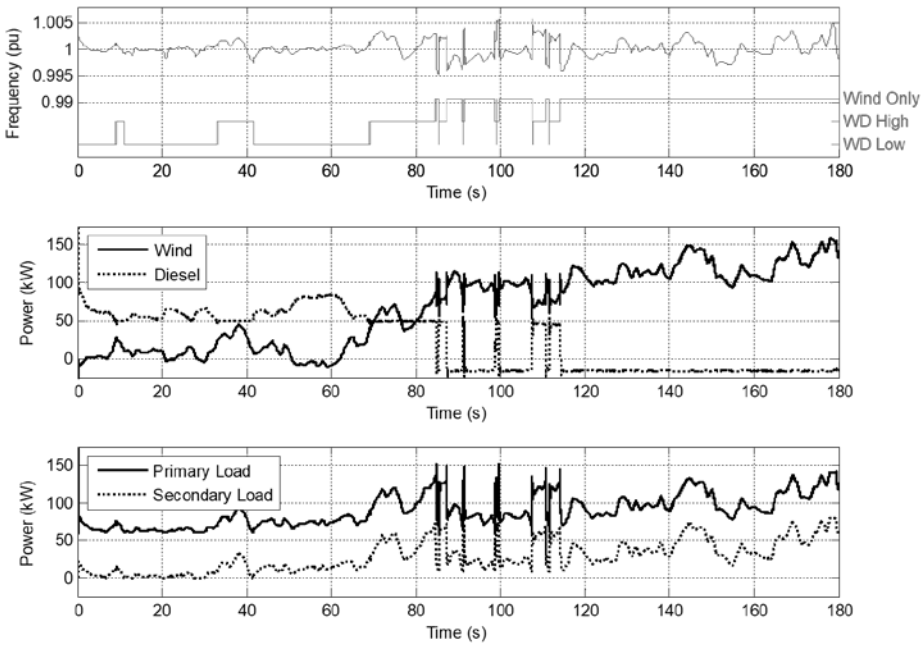

Fig. 75. System frequency and control mode, wind and diesel power, and primary and secondary load simulation response to a synthesized dynamic wind profile (mean wind speed = 8 m/s) with the transition from wind-diesel to wind-only mode being managed by the autonomous distributed secondary load control.

For a more realistic wind profile, a three-minute synthesized dynamic wind speed profile (mean speed = 8 m/s) is generated based on synthesized one-second Shinozuka turbulence as discussed in [154], and introduced to the system under a steady load of 60 kW. In [155], this method is shown to be accurate for short dynamic time scales. As seen in Fig. 75, the system is allowed to transition from WD-Low to wind-only mode using the distributed secondary loads for frequency control during and after the transition. Up to t = 85 s, the diesel can freely switch between isochronous and droop modes as the amount of wind power varies. At t = 114 s, the distributed secondary loads take over control of the frequency regulation (within +/- 0.5%) as the diesel is now isolated from the system. This is an example of frequency stability improvements through load control, especially under high RE penetration.

5.10 Hardware in the Loop Simulation Example

The studies presented next describe HIL setups of real hardware equipment (inverter and loads) interfaced with a DRTS through an amplifier, to validate the equipment being tested and also study its impact on the microgrid.

5.10.1 PHIL Validation of Inverter Supplementary Controls

The PHIL setup depicted in Fig. 76 consists of a simulated network with a synchronous generator, low voltage lines, a load, and a storage system, integrated with a hardware PV inverter connected to a PV simulator. The inverter has P-f droop control, and the simulated storage system has a virtual inertia control. In order to evaluate the contribution of these controls to frequency regulation, a load change is analyzed with and without droop and virtual inertia controls.

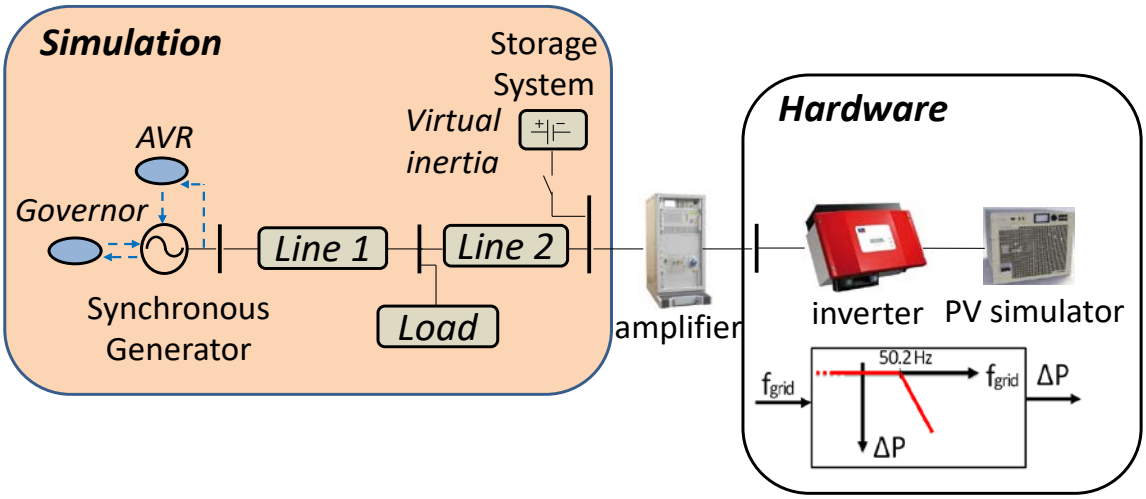

Fig. 76. PHIL setup.

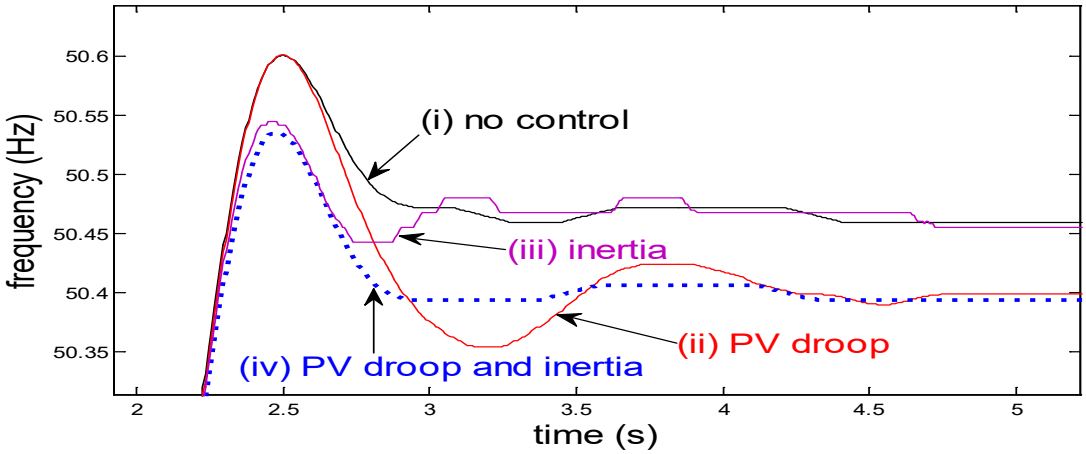

Fig. 77. Frequency for PHIL studies.

Fig. 77 illustrates the frequency deviation for the various controls studies with the PHIL setup. The droop control (slow controller of the hardware inverter) reduces the steady state error, and the simulated virtual inertia control reduces the transient peak compared to the case with no DER frequency controls. The best case is observed when both droop and virtual inertia controls are included [156]. This is an example of frequency stability improvement.

In standardized testing of P-f droop curves, the inverter is typically tested under specific frequency profiles and without having any interaction with other equipment. With the PHIL experiments, the hardware inverter can be tested integrated with a microgrid, and its effect on the system can also be evaluated.

5.10.2 CHIL and PHIL Testing of Microgrid Frequency Controller

The setup depicted in Fig. 78 shows a simulated microgrid, which includes a synchronous generator, a LV line, a load, and a PV, interfaced through a PHIL setup with some real external loads and an external controller (CHIL). The purpose of the controller is to activate the real external dump loads to satisfy the minimum load requirement of the synchronous generator (30% of nominal power), which can be an issue with high PV penetration as load and solar radiation changes during the day.

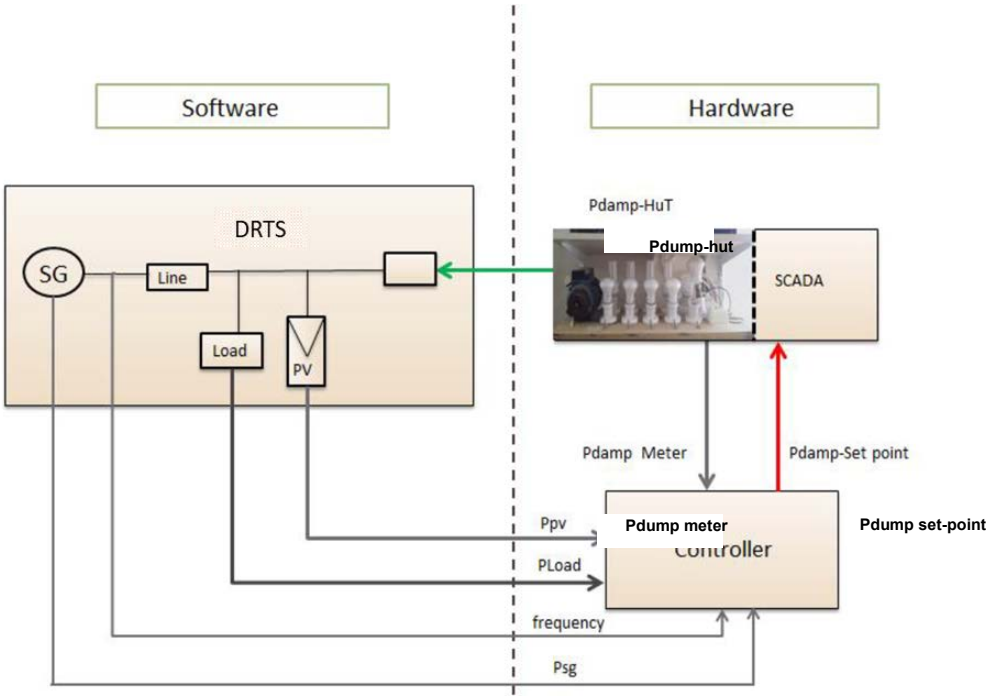

Fig. 78. CHIL and PHIL testing of islanded microgrid controller.

The activation of the dump loads is shown in Fig. 79, resulting in the frequency regulation illustrated in Fig. 80; observe the reduction in the steady state frequency deviation. The transient response of frequency and active power of the synchronous generator for a sudden increase in solar irradiation and corresponding activation of the dump loads are illustrated in Figs. 81 and 82, respectively. This is an example of frequency stability improvement.

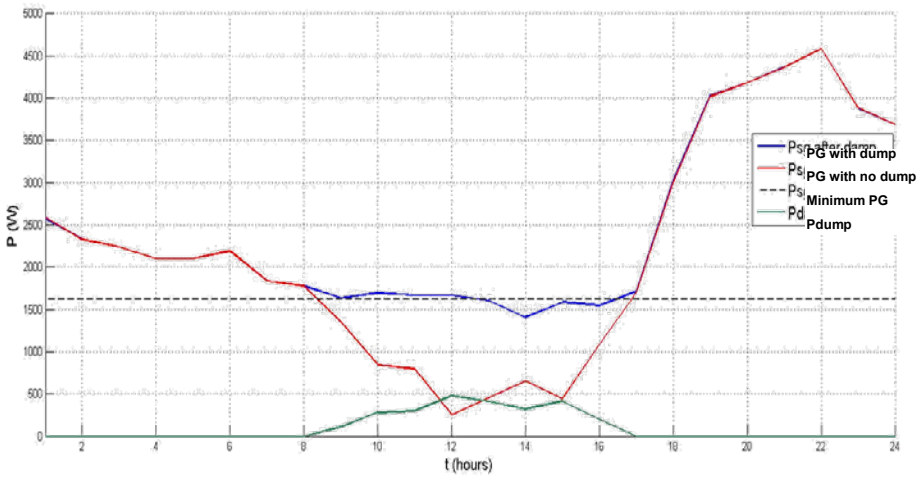

Fig. 79. CHIL and PHIL synchronous generator and dump load active power during daily operation.

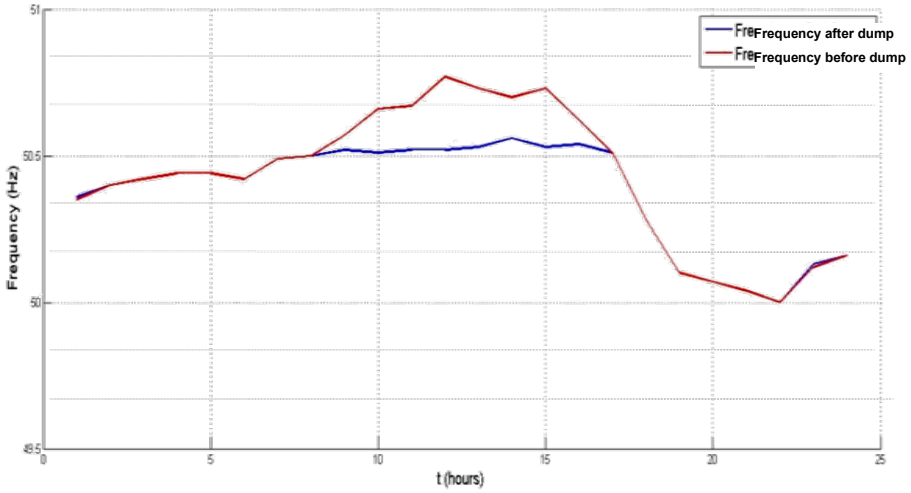

Fig. 80. CHIL and PHIL frequency before and after the activation of the dump loads during daily operation.

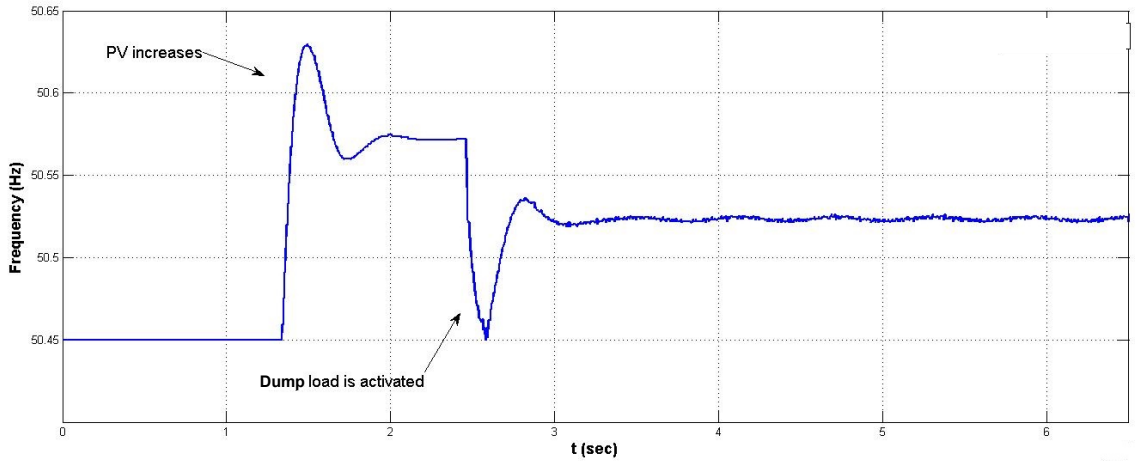

Fig. 81. CHIL and PHIL Frequency response for fast solar radiation changes.

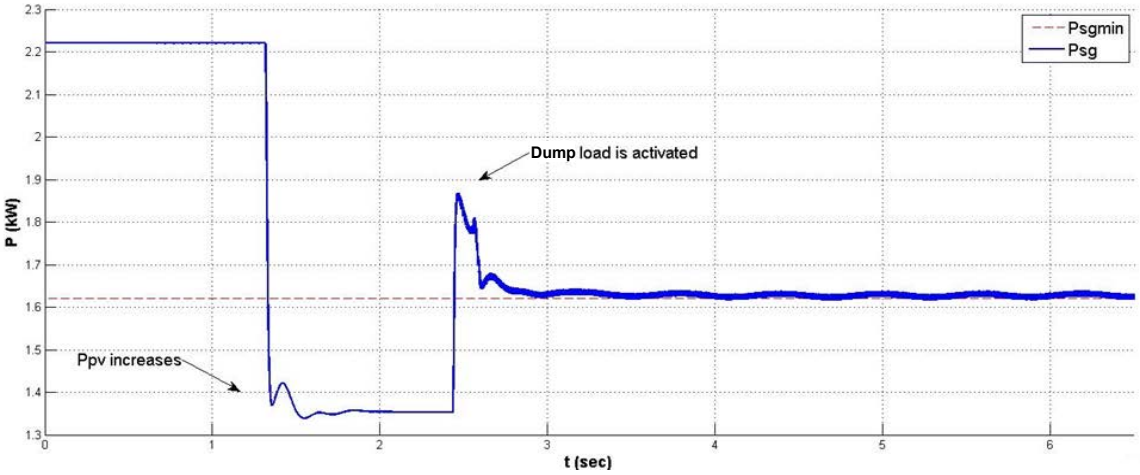

Fig. 82. CHIL and PHIL synchronous generator power response for fast solar radiation changes.

6. CONCLUSIONS

Microgrids present some unique characteristics, compared to transmission systems, associated with their distribution voltage levels and generation equipment, such as unbalanced operation, feeder characteristics (small X/R ratio, short length), load voltage dependency, inverter-based generation and storage, low inertia, low short-circuit capacity, and high load and generation variability and uncertainty. These particular grid characteristics have a significant impact on the stability of islanded microgrids, presenting particular stability issues different from the classical problems observed in bulk power systems.

This document focused on presenting relevant microgrid stability definitions, modeling, analysis techniques, and examples. It provided first a definition of microgrid stability, and classified various forms of instabilities in microgrids based on their fundamental causes and manifestations. A discussion of the modeling of microgrid core components, including DERs, feeders, and loads was also presented. An overview of analyses techniques that allow the study and understanding of stability in microgrids was then presented and discussed. Finally, various microgrid stability examples were provided, including studies of the impact of unbalanced loading, component modeling, the linkage of voltage and frequency, as well as PLL bandwidth and synchronization, parallel converter and diesel droop control issues, frequency stability, load dynamics, and islanding and grid synchronization. Mitigation techniques to improve microgrid stability were also discussed as part of the stability examples, in particular voltage-frequency control and virtual-inertia.

REFERENCES

[1] B. Lasseter, "Microgrids [distributed power generation]," in *Proc. of IEEE Power Eng. Soc. Winter Meet.*, pp. 146–149, Jan. 2001.

[2] R. H. Lasseter, J. H. Eto, B. Schenkman, J. Stevens, H. Vollkommer, D. Klapp, E. Linton, H. Hurtado, and J. Roy, "CERTS microgrid laboratory test bed," *IEEE Trans. Power Del.*, vol. 26, pp. 325–332, Jan. 2011.

[3] D. E. Olivares, A. Mehrizi-Sani, A. H. Etemadi, C. A. Canizares, R. Iravani, M. Kazerani, A. H. Hajimiragha, O. Gomis-Bellmunt, M. Saeedifard, R. Palma-Behnke, G. A. Jimenez-Estevez, and N. D. Hatziargyriou, "Trends in microgrid control," *IEEE Trans. Smart Grid*, vol. 5, no. 4, pp. 1905–1919, July 2014.

[4] N. Hatziargyriou, H. Asano, R. Iravani, and C. Marnay, "Microgrids," *IEEE Power Energy Mag.*, vol. 5, no. 4, pp. 78–94, July 2007.

[5] N. Hatziargyriou, *Microgrids Architectures and Control*. West Sussex, United Kingdom: Wiley- IEEE Press, 2014.

[6] F. Katiraei, M. Iravani, and P. W. Lehn, "Micro-grid autonomous operation during and subsequent to islanding process," *IEEE Trans. Power Del*., vol. 20, no. 1, pp. 248–257, Jan. 2005.

[7] M. Liserre, G. Buticchi, M. Andresen, G. D. Carne, L. F. Costa, and Z. X. Zoue, "The smart transformer: Impact on the electric grid and technology challenges," *IEEE Ind. Electron. Mag*., vol. 10, no. 2, pp. 46–58, 2016.

[8] H. Karimi, H. Nikkhajoei, and M. R. Iravani, "Control of an electronically-coupled distributed resource unit subsequent to an islanding event," *IEEE Trans. Power Del*., vol. 23, no. 1, pp. 493– 501, Jan. 2008.

[9] H. Karimi, A. Yazdani, and M. R. Iravani, "Negative-sequence current injection for fast islanding detection of a distributed resource unit," *IEEE Trans. Power Electron*., vol. 23, no. 1, pp. 298–307, Jan. 2008.

[10] M. Arriaga, C. Canizares, and M. Kazerani, "Northern lights: Access to electricity in Canada's northern and remote communities," *IEEE Power Energy Mag*., vol. 12, no. 4, pp. 50–59, Aug. 2014.

[11] A. H. Hajimiragha and M. R. D. Zadeh, "Research and development of a microgrid control and monitoring system for remote community of bella coola: Challenges,

solutions, achievements and lessons learned," in *Proc. of IEEE Int. Conf. on Smart Ener. Grid. Eng. (SEGE)*, pp. 1–6, Aug. 2013.

[12] D. Neves, C. A. Silva, and S. Connors, "Design and implementation of hybrid renewable energy systems on micro-communities: A review on case studies," *Renewable and Sustainable Energy Reviews*, vol. 31, pp. 935–946, Mar. 2014.

[13] R. Palma-Behnke, C. Benavides, F. Lanas, B. Severino, L. Reyes, J. Llanos, and D. Saez, "A microgrid energy management system based on the rolling horizon strategy," *IEEE Trans. Smart Grid*, vol. 4, no. 2, pp. 996–1006, June 2013.

[14] N. W. A. Lidula and A. D. Rajapakse, "Microgrids research: A review of experimental microgrids and test systems," *Renewable and Sustainable Energy Reviews*, vol. 15, no. 1, pp. 186–202, Jan. 2011.

[15] D. T. Ton, and W-T. P. Wang, "A more resilient grid: The U.S. Department of Energy joins with stakeholders in an R&D plan," *IEEE Power Energy Mag*., vol. 13, no. 3, pp. 26-34, May/Jun. 2015.

[16] K. P. Schneider, F. K. Tuffner, M. A. Elizondo, C. C. Liu, Y. Xu and D. Ton, "Evaluating the Feasibility to Use Microgrids as a Resiliency Resource," in *IEEE Trans. Smart Grid*, vol. 8, no. 2, pp. 687-696, Mar. 2017.

[17] J. M. Guerrero, F. Blaabjerg, T. Zhelev, K. Hemmes, E. Monmasson, S. Jemei, M. P. Comech, R. Granadino, and J. I. Frau, "Distributed generation: toward a new energy paradigm," *IEEE Ind. Electron. Mag*., vol. 4, no. 1, pp. 52-64, Mar. 2010.

[18] "Global Microgrid Market 2016-2020," TechNavio, Dublin, Ireland, Tech. Rep. 3829462, Aug. 2016.

[19] P. Kundur, J. Paserba, V. Ajjarapu, G. Andersson, A. Bose, C. Canizares, N. Hatziargyriou, D. Hill, A. Stankovic, C. Taylor, T. V. Cutsem, and V. Vittal, "Definition and classification of power system stability," *IEEE Trans. Power Syst.*, vol. 19, no. 2, pp. 1387–1401, May 2004.

[20] Power System Dynamic Performance Committee, Power System Stability Controls Subcommittee, Task Force on Contribution to Bulk System Control and Stability by Distributed Energy Resources connected at Distribution Network, "Contribution to bulk system control and stability by distributed energy resources connected at distribution network," IEEE, Tech. Rep. PES TR22, Jan. 2017.

[21] *IEEE Guide for Design, Operation, and Integration of Distributed Resource Island Systems with Electric Power Systems*, IEEE Std. 1547.4, 2011.

[22] F. Katiraei, R. Iravani, N. Hatziargyriou, and A. Dimeas, "Microgrids management," *IEEE Power Energy Mag*., vol. 6, no. 3, pp. 54–65, June 2008.

[23] Commission Staff Working Paper, "Analysis of options beyond 20% GHG emission reductions: Member state results," European Commission, Brussel, Belgium, Tech. Rep. 1.2.2012, Jan. 2012.

[24] REN21 Steering Committee, "Renewables 2010 global status report," REN21, Paris, France, Tech. Rep. REN21.2010, Sep. 2010.

[25] "Green energy act, 2009," Government of Ontario, Tech. Rep. [Online]. Available: https: //www.ontario.ca/laws/statute/09g12

[26] A. Ipakchi and F. Albuyeh, "Grid of the future," *IEEE Power Energy Mag*., vol. 7, no. 2, pp. 52–62, Apr. 2009.

[27] C. Yuen, A. Oudalov, and A. Timbus, "The provision of frequency control reserves from multiple microgrids," *IEEE Trans. Ind. Electron*., vol. 58, no. 1, pp. 173–183, Jan. 2011.

[28] C. Li, S. K. Chaudhary, M. Savaghebi, J. C. Vasquez, and J. M. Guerrero, "Power flow analysis for low-voltage ac and dc microgrids considering droop control and virtual impedance," *IEEE Trans. Smart Grid*, vol. 8, no. 8, pp. 2754-2764, Nov. 2017.

[29] K. Strunz, E. Abbasi, C. Abbey, C. Andrieu, U. Annakkage, S. Barsali, R. C. Campbell, R. Fletcher, F. Gao, T. Gaunt, A. Gole, N. Hatziargyriou, R. Iravani, G. Joos, H. Konishi, M. Kuschke, E. Lakervi, C. Liu, J. Mahseredjian, F. Mosallat, D. Muthumuni, A. Orths, S. Papathanassiou, K. Rudion, Z. Styczynski, and S. C. Verma, "Benchmark systems for network integration of renewable and distributed energy resources," CIGRE, Paris, France, Tech. Rep. C6.04.02, Apr. 2014.

[30] M. Arriaga and C. A. Canizares, "Overview and analysis of data for microgrid at kasabonika lake first nation (KLFN)," Hatch Project Confidential Report, University of Waterloo, Tech. Rep., Sep. 2015.

[31] E. Nasr-Azadani, C. A. Canizares, D. E. Olivares, and K. Bhattacharya, "Stability analysis of unbalanced distribution systems with synchronous machine and DFIG based distributed generators," *IEEE Trans. Smart Grid*, vol. 5, no. 5, pp. 2326–2338, Sep. 2014.

[32] M. Farrokhabadi, S. Konig, C. Canizares, K. Bhattacharya, and T. Leibfried, "Battery energy storage system models for microgrid stability analysis and dynamic simulation," *IEEE Trans. Power Syst*., vol. 33, no. 2, pp. 2301-2312, Aug. 2017.

[33] "Distributed generation technical interconnection requirements: Interconnections at voltages 50kV and below," Hydro One Networks Inc., Toronto, Ontario, Tech. Rep. DT-10-015 R3, Mar. 2013.

[34] J. Wang, H. Zhang, and Y. Zhou, "Intelligent under frequency and under voltage load shedding method based on the active participation of smart appliances," *IEEE Trans. Smart Grid*, vol. 8, no. 1, pp. 353–361, Jan. 2017.

[35] C. W. Taylor, "Concepts of undervoltage load shedding for voltage stability," *IEEE Trans. Power Del*., vol. 7, no. 2, pp. 480–488, Apr. 1992.

[36] V. I. Vorotnikov, *Partial Stability and Control*. Cambridge, MA: Birkhauser, 1998.

[37] N. Rouche, P. Habets, and M. Laloy, *Stability Theory by Liapunov's Direct Method*. New York, NY: Springer, 1977.

[38] A. Bernstein, J. L. Boudec, L. Reyes-Chamorro, and M. Paolone, "Real-time control of microgrids with explicit power setpoints: Unintentional islanding," in *Proc. IEEE PowerTech, Eindhoven,* Netherlands, July 2015, pp. 1–6.

[39] G. Dellile, B. Francois, and G. Malarange, "Dynamic frequency control support by energy storage to reduce the impact of wind and solar generation on isolated power system's inertia," *IEEE Trans. Sustain. Energy*, vol. 3, no. 4, pp. 931–939, Oct. 2012.

[40] A. Borghetti, C. A. Nucci, M. Paolone, G. Ciappi, and A. Solari, "Synchronized phasors monitoring during the islanded maneuver of an active distribution network," *IEEE Trans. Smart Grid*, vol. 2, no. 1, pp. 82–91, Mar. 2011.

[41] Z. Xu, M. Togeby, and J. Østergaard, "Demand as frequency controlled reserve: Final report of the PSO project," Technical University of Denmark, Tech. Rep., 2008.

[42] N. Hatziargyriou, E. Karapidakis, and D. Hatzifotis, "Frequency stability of power systems in large islands with high wind power penetration," in *Bulk Power Syst. Dynamics Control Symp.- IV Restructuring*, vol. PAS-102, 1998, pp. 1501–1504.

[43] K. Christakou, J. Y. LeBoudec, M. Paolone, and D. C. Tomozei, "Efficient computation of sensitivity coefficients of node voltages and line currents in unbalanced radial electrical distribution networks," *IEEE Trans. Smart Grid*, vol. 4, no. 2, pp. 741–750, June 2013.

[44] M. Farrokhabadi, C. A. Canizares, and K. Bhattacharya, "Frequency control in isolated/islanded microgrids through voltage regulation," *IEEE Trans. Smart Grid*, vol. 8, no. 3, pp. 1185-1194, May. 2017.

[45] M. Diaz-Aguilo, J. Sandraz, R. Macwan, F. de Leon, D. Czarkowski, C. Comack, and D. Wang, "Field-validated load model for the analysis of CVR in distribution secondary networks: Energy conservation," *IEEE Trans. Power Del*., vol. 28, no. 4, pp. 2428 – 2436, Oct. 2013.

[46] G. Delille, L. Capely, D. Souque, and C. Ferrouillat, "Experimental validation of a novel approach to stabilize power system frequency by taking advantage of load voltage sensitivity," in *Proc. of IEEE PowerTech*., Eindhoven, Netherlands, June 2015.

[47] N. Pogaku, M. Prodanovic, and T. C. Green, "Modeling, analysis and testing of autonomous operation of an inverter-based microgrid," *IEEE Trans. Power Electron.*, vol. 22, no. 2, pp. 613–625, Mar. 2007.

[48] R. Prada and L. Souza, "Voltage stability and thermal limit: constraints on the maximum loading of electrical energy distribution feeders," *IEE Proceedings - Generation, Transmission and Distribution*, vol. 145, no. 5, pp. 573–577, Sep. 1998.

[49] C. K. Sao and P. W. Lehn "Autonomous Load Sharing of Voltage Source Converters," *IEEE Trans. Power Del*., vol. 20, no. 2, pp. 1009–1016, Aug. 2016.

[50] J. M. Guerrero, M. Chandorka, T. Lee, and P. C. Loh, "Advanced control architectures for intelligent microgrids–part I: Decentralized and hierarchical control," *IEEE Trans. Ind. Electron.*, vol. 60, no. 4, pp. 1254–1262, April 2012.

[51] W. Yao, M. Chen, J. Matas, J. M. Guerrero, and Z. Qian, "Design and analysis of the droop control method for parallel inverters considering the impact of the complex impedance on the power sharing," *IEEE Trans. Ind. Electron*., vol. 58, no. 2, pp. 576–588, Feb. 2011.

[52] G. Olson. (2010). White paper on paralleling dissimilar generators: Part 3-load sharing compatibility, Cummins Power Generation. [Online]. Available: https://power.cummins.com/sites/default/files/literature/technicalpapers/PT-9017-P3-Dissimilar-en.pdf.

[53] A. Hajimiragha, M. R. D. Zadeh, and S. Moazeni, "Microgrids frequency control considerations within the framework of the microgrid generation scheduling problem," *IEEE Trans. Smart Grid*, vol. 6, no. 2, pp. 534–547, 2015.

[54] R. Belkacemi, S. Zarrabian, A. Babalola, and R. Craven, "Experimental transient stability analysis of microgrid systems: Lessons learned," *IEEE Trans. Power Del*., vol. 28, no. 4, pp. 2428 – 2436, Oct. 2013.

[55] P. Kundur, *Power System Stability and Control*. New York, US: McGraw-Hill Professional, 1994.

[56] X. Wang, F. Blaabjerg, and W. Wu, "Modeling and analysis of harmonic stability in an ac power- electronic-based power system," *IEEE Trans. Power Electron*., vol. 29, no. 12, pp. 6421–6432, Dec. 2014.

[57] X. Wang, F. Blaabjerg, and Z. Chen, "Autonomous control of inverter-interfaced distributed generation units for harmonic current filtering and resonance damping in an islanded microgrid," *IEEE Trans. Ind. Appl*., vol. 50, no. 1, pp. 452–461, Jan. 2014.

[58] J. He, Y. W. Li, D. Bosnjak, and B. Harris, "Investigation and active damping of multiple resonances in a parallel-inverter-based microgrid," *IEEE Trans. Power Electron*., vol. 28, no. 1, pp. 234–246, Jan. 2013.

[59] X. Wang, F. Blaabjerg, M. Liserre, Z. Chen, J. He, and Y.Li, "An active damper for stabilizing power-electronic-based ac systems," *IEEE Trans. Power Electron*., vol. 29, no. 7, pp. 3318–3329, July 2014.

[60] M. Liserre, F. Blaabjerg, and S. Hansen, "Design and control of an LCL-filter based three-phase active rectifier," *IEEE Trans. Ind. Appl*., vol. 41, no. 5, pp. 1281–1291, Sep. 2005.

[61] S. G. Parker, B. P. McGrath, and D. G. Holmes, "Regions of active damping control for LCL filters," *IEEE Trans. Ind. Appl*., vol. 50, no. 1, pp. 424–434, Jan. 2014.

[62] L. Harnefors, M. Bongiorno, and S. Lundberg, "Input-admittance calculation and shaping for controlled voltage-source converters," *IEEE Trans. Ind. Electron*., vol. 54, no. 6, pp. 3323–3334, Dec. 2007.

[63] M. Cespedes and J. Sun, "Impedance modeling and analysis of grid-connected voltage-source converters," *IEEE Trans. Power Electron*., vol. 29, no. 3, pp. 1254–1261, Mar. 2014.

[64] B. Wen, D. Boroyevich, P. Mattavelli, Z. Shen, and R. Burgos, "Influence of phase-locked loop on input admittance of three-phase voltage-source converters," in *Proc. of the 28th Annu. IEEE Appl. power Electron. Conf. Expo*., Mar. 2013, pp. 1–8.

[65] O. Goksu, R. Teodorescu, C. L. Bak, F. Iov, and P. Carne, "Instability of wind turbine converters during current injection to low voltage grid faults and PLL frequency based stability solution," *IEEE Trans. Power Syst*., vol. 29, no. 4, pp. 1683–1691, July 2014.

[66] A. H. K. Alaboudy, H. H. Zeineldin, and J. L. Kirtley, "Microgrid stability characterization subsequent to fault-triggered islanding incidents," *IEEE Trans. Power Del*., vol. 27, no. 2, pp. 658–669, Apr. 2012.

[67] S. Pelland, D. Turcotte, G. Colgate, and A. Swingler, "Nemiah valley photovoltaic-diesel mini-grid: System performance and fuel saving based on one year of monitored data," *IEEE Trans. Sust. Energy*, vol. 3, no. 1, pp. 167–175, Jan. 2012.

[68] U. Tamrakar, D. Galipeau, R. Tonkoski, and I. Tamrakar, "Improving transient stability of photovoltaic-hydro microgrids using virtual synchronous machines," in *Proc. IEEE PowerTech*, June 2015, pp. 1–6.

[69] M. Torres and L. A. Lopes, "Inverter-based diesel generator emulator for the study of frequency variations in a laboratory-scale autonomous power system," *Energy and Power Engineering*, vol. 5, no. 3, pp. 274–283, May 2013.

[70] D. Maksimovic, A. M. Stankovic, V. J. Thottuvelil, and G. C. Verghese, "Modeling and simulation of power electronic converters," in *Proc. IEEE*, vol. 89, no. 6, pp. 898–912, 2001.

[71] R. Middlebrook and S. Cuk, "A general unified approach to modeling switching power converter stages," in *Proc. IEEE Power Electron. Spec. Conf*., 1982, 1976, pp. 240–250.

[72] R. D. Middlebrook, "Small-signal modeling of pulse-width modulated switched-mode power converters," in *Proc. IEEE*, vol. 76, no. 4, Apr. 1988, pp. 343–354.

[73] E. P. Weichmann, P. D. Ziogas, and V. R. Stefanovic, "Generalized functional model for three-phase PWM inverter/rectifier converters," *IEEE Trans. Ind. Appl*., vol. IA-23, no. 2, pp. 236–246, Mar. 1987.

[74] B.-K. Lee and M. Ehsani, "A simplified functional simulation model for three-phase voltage-source inverter using switching function concept," *IEEE Trans. Ind. Electron*., vol. 48, no. 2, pp. 309–321, Apr. 2001.

[75] P. Zuniga-Haro and J. M. Ramirez, "SSSC switching functions model," *IEEE Trans. Power Del*., vol. 21, no. 1, pp. 518–520, Jan. 2006.

[76] O. S. Nduka and B. C. Pal, "Harmonic domain modeling of PV system for the assessment of grid integration impact," *IEEE Trans. Sust. Ener.*, vol. 8, no. 3, pp. 1154–1165, July 2017.

[77] H. Le-Huy, G. Sybille, R. Gagnon, and V. Q. Do, "Real-time simulation of PWM power converters in a doubly-fed induction generator using switching-function-based models," in *Proc. IEEE Ind. Electron. Conf. (IECON)*, Nov. 2006, pp. 1878–1883.

[78] J. Mahdavi, A. Emaadi, M. D. Bellar, and M. Ehsani, "Analysis of power electronic converters using the generalized state-space averaging approach," *IEEE Trans. Circuits Syst. I, Fundam. Theory Appl*., vol. 44, no. 8, pp. 767–770, Aug. 1997.

[79] L. Salazar and G. Joos, "PSPICE simulation of three-phase inverters by means of switching functions," *IEEE Trans. Power Electron*., vol. 9, no. 1, pp. 35–42, Jan. 1994.

[80] V. Monteiro, J. G. Pinto, B. Exposto, and J. L. Afonso, "Comprehensive comparison of a current- source and a voltage-source converter for three-phase EV fast battery chargers," in *Proc. Int. Conf. Compat. Power Electron. (CPE)*, June 2015, pp. 173–178.

[81] Y. Suh, J. Steinke, and P. Steimer, "A study on efficiency of voltage source and current source converter systems for large motor drives," in *Proc. IEEE Power Electron. Specialists Conf.*, June 2006, pp. 1–7.

[82] M. Mohr and F. W. Fuchs, "Comparison of three phase current source inverters and voltage source inverters linked with dc to dc boost converters for fuel cell generation systems," in *Proc. European Conf. Power Electron. Applications*, Sept. 2005.

[83] Y. W. Li, "Control and resonance damping of voltage-source and current-source converters with LC filters," *IEEE Trans. Ind. Electron.*, vol. 56, no. 5, pp. 1511–1521, May 2009.

[84] J. Rocabert, A. Luna, F. Blaabjerg, and P. Rodriguez, "Control of power converters in AC microgrids," *IEEE Trans. Power Electron.*, vol. 27, no. 11, pp. 4734–4749, Nov. 2012.

[85] H. Akagi, E. H. Watanabe, and M. Aredes, *Instantaneous Power Theory and Applications to Power Conditioning*. IEEE Press, 2007.

[86] A. Yazdani and R. Iravani, *Voltage-Sourced Converters in Power Systems: Modeling, Control, and Applications*. Hoboken, NJ: Wiley-IEEE Press, 2010.

[87] R. Teodorescu, M. Liserre, and P. Rodriguez, *Grid Converters for Photovoltaic and Wind Power Systems*. West Sussex, UK: Wiley-IEEE Press, 2011.

[88] Z. Jankovic, B. Novakovic, V. Bhavaraju, and A. Nasiri, "Average modeling of a three-phase inverter for integration in a microgrid," in *Proc. IEEE Energy Conversion Cong. Expos.*, Milwaukee, WI, Nov. 2014.

[89] A. Mitra and D. Chatterjee, "Active power control of DFIG-based wind farm for improvement of transient stability of power systems," *IEEE Trans. Power Syst.*, vol. 13, no. 1, pp. 82–93, Feb. 2015.

[90] Y. Zhou, D. Nguyen, P. Kjaer, and S. Saylors, "Connecting wind power plant with weak grid- challenges and solutions," in *Proc. IEEE Power Eng. Soc. Gen. Meeting*, Vancouver, BC, July 2015, pp. 1–7.

[91] J. Hu, Y. Huang, D. Wang, H. Yuan, and X. Yuan, "Modeling of grid-connected DFIG-based wind turbines for dc-link voltage stability analysis," *IEEE Trans. Sust. Ener.*, vol. 6, no. 4, pp. 1325–1336, Oct. 2015.

[92] L. Fan and Z. Miao, "An explanation of oscillations due to wind power plants weak grid interconnection," *IEEE Trans. Sust. Ener.*, vol. 9, no. 1, pp. 488-490, Jan. 2018.

[93] G. Delille, B. Franois, and G. Malarange, "Dynamic frequency control support by energy storage to reduce the impact of wind and solar generation on isolated power system's inertia," *IEEE Trans. Sustain. Ener.*, vol. 3, no. 4, pp. 931–939, Nov. 2012.

[94] M. Bahramipanah, D. Torregrossa, R. Cherkaoui, and M. Paolone, "A decentralized adaptive model- based real-time control for active distribution networks using battery energy storage systems," *IEEE Trans. Smart Grid*, vol. PP, no. 99, pp. 1–14, Nov. 2016.

[95] S. Piller, M. Perrin, and A. Jossen, "Methods for state-of-charge determination and their applications," *J. Power Sources*, vol. 96, pp. 113–120, 2001.

[96] V. Pop, H.J. Bergveld, P.H.L. Notten, and P.P.L. Regtien, "State-of-the-art of battery state-of-charge determination," *Meas. Sci. Technol.*, vol. 16, pp. R93-R110, 2005.

[97] I. Papič, "Simulation model for discharging a lead-acid battery energy storage system for load leveling," *IEEE Trans. Energy Convers*., vol. 21, no. 2, pp. 608-615, June 2006.

[98] M. Coleman, C.K. Lee, C. Zhu, and W.G. Hurley, "State-of-charge determination from EMF voltage estimation: using impedance, terminal voltage, and current for lead-acid and lithium-ion batteries," *IEEE Trans. Ind. Electron*., vol. 54, no. 5, pp. 2550-2557, October 2007.

[99] B. Belvedere, M. Bianchi, A. Borghetti, C. A. Nucci, M. Paolone and A. Peretto, "A microcontroller-based power management system for standalone microgrids with hybrid power supply," *IEEE Trans. Sust. Ener.*, vol. 3, no. 3, pp. 422-431, July 2012.

[100] G. Singh, "Solar power generation by PV (photovoltaic) technology: A review," *Energy*, vol. 53, pp. 1–13, May 2013.

[101] F. Sossan, E. Namor, R. Cherkaoui, and M. Paolone, "Achieving the dispatchability of distribution feeders through prosumers data driven forecasting and model predictive control of electrochemical storage," *IEEE Trans. on Sust. Ener.*, vol. 7, no. 4, pp. 1762-1777, Oct. 2016.

[102] A. R. Reisi, M. H. Moradi, and S. Jamasb, "Classification and comparison of maximum power point tracking techniques for photovoltaic system: A review," *Renewable and Sustainable Energy Revie*ws, vol. 19, pp. 433–443, Mar. 2013.

[103] Z. Salam, J. Ahmed, and B. S. Merugu, "The application of soft computing methods for MPPT of PV system: A technological and status review," *Applied Energy*, vol. 107, pp. 135–148, July 2013.

[104] R. G. Said, A. S. Abdel-Khalik, A. E. Zawawi, and M. S. Hamad, "Integrating flywheel energy storage system to wind farms-fed HVDC system via a solid state transformer," in *Proc. Int. Conf. Renewable Energy Research Application (ICRERA)*, Oct. 2014, pp. 375–380.

[105] *TSAT Manual*, 16th ed., Powertech Labs Inc., April 2016.

[106] R. Ranjan, B. Venkatesh, A. Chaturvedi, and D. Das, "Power flow solution of three-phase unbalanced radial distribution network," *Electric Power Components and Systems*, vol. 32, no. 4, pp. 421–433, Apr. 2004.

[107] M. A. Elizondo, F. K. Tuffner and K. P. Schneider, "Simulation of inrush dynamics for unbalanced distribution systems using dynamic-phasor models," *IEEE Trans. Power Syst.*, vol. 32, no. 1, pp. 633-642, Jan. 2017.

[108] A. J. Collin, G. Tsagarakis, A. E. Kiprakis, and S. McLaughlin, "Development of low-voltage load models for the residential load sector," *IEEE Trans. Power Syst.*, vol. 29, no. 5, pp. 2180–2188, Feb. 2014.

[109] Z. Zou, G. Buticchi, M. Liserre, A. M. Kettner, and M. Paolone, "Voltage stability analysis using a complete model of grid-connected voltage-source converters," in *Proc. IEEE Ener. Conver. Cong. and Expo. (ECCE)*, Milwaukee, WI, Sep. 2016, pp. 1–8.

[110] A. Griffo and J. Wang, "Large signal stability analysis of aircraft power systems with constant power loads," *IEEE Trans. Aerosp. Electron. Syst.*, vol. 48, no. 1, pp. 477–489, Jan. 2012.

[111] R. Majumder, "Some aspects of stability in microgrids," *IEEE Trans. Power Syst.*, vol. 28, no. 3, pp. 3243–3252, Aug. 2013.

[112] J. Sun, "Small-signal methods for ac distributed power systems - a review," *IEEE Trans. Power Electron.*, vol. 24, no. 11, pp. 2545–2554, Nov. 2009.

[113] M. Kabalan, P. Singh, and D. Niebur, "Large signal Lyapunov-based stability studies in microgrids: A review," *IEEE Trans. Smart Grid*, vol. 8, no. 5, pp. 2287–2295, Sept. 2017.

[114] F. Andrade, J. Cusido, and L. Romeral, "Transient stability analysis of inverter interfaced distributed generators in a microgrid system," in *Proc. the 14th European Conf. Power Electron. and Applications (EPE 2011)*, Birmingham, UK, pp. 1–10, Aug. 2011.

[115] K. Acharya, S. K. Mazumder, and I. Basu, "Reaching criterion of a three-phase voltage-source inverter operating with passive and nonlinear loads and its impact on global stability," *IEEE Trans. Ind. Electron.*, vol. 55, no. 4, pp. 1795–1812, Apr. 2008.

[116] M. Kabalan, P. Singh, and D. Niebur, "Nonlinear Lyapunov stability analysis of seven models of a dc/ac droop controlled inverter connected to an infinite bus," *IEEE Trans. Smart Grid*, vol. PP, no. 99, pp. 1–11, Sept. 2017.

[117] W. Ren, M. Steurer and T. Baldwin, "Improve the stability and the accuracy of power hardware-in-the-loop simulation by selecting appropriate interface algorithms," *IEEE Trans. Ind. Appl.*, vol. 44, no. 4, pp. 1286-1294, 2008.

[118] J. Alipoor, Y. Miura, and T. Ise, "Power system stabilization using virtual synchronous generator with alternating moment of inertia," *IEEE Trans. Emerg. Sel. Topics Power Electron.*, vol. 3, no. 2, pp. 451–458, June 2015.

[119] F. Andrade, K. Kampouropoulos, L. Romeral, J. C. Vasquez, and J. M. Guerrero, "Study of large-signal stability of an inverter-based generator using a Lyapunov function," in *Proc. IEEE Ind. Electron. Soc. (IECON)*, Oct. 2014, pp. 1840–1846.

[120] F. A. Rengifo, L. Romeral, J. Cusid, and J. J. Crdenas, "New model of a converter-based generator using electrostatic synchronous machine concept," *IEEE Trans. Energy Convers.*, vol. 29, no. 2, pp. 344–353, June 2014.

[121] H. W. Dommel, "Digital computer solution of electromagnetic transients in single- and multiphase networks," *IEEE Trans. Power App. Syst.*, vol. PAS-88, no. 4, pp. 388-399, Apr. 1969.

[122] Manitoba HVDC Research Centre, PSCAD Software, [Online]. Available: http://hvdc.ca/pscad.

[123] L. Qi and S. Woodruff, "Stability analysis and assessment of integrated power systems using RTDS," in *Proc. IEEE Elec. Ship Tech. Symp.*, July 2005, pp. 325–332.

[124] GE Digital Energy, PSLF Software, [Online]. Available: http://gedigitalenergy.com/UOS.htm

[125] Siemens, PSS/E Software, [Online]. Available: http://www.energy.siemens.com/hq/en/services/power-transmission-distribution/power-technologies-international/software-solutions/pss-e.htm

[126] P. W. Sauer, B. C. Lesieutre, and M. A. Pai, "Transient algebraic circuits for power system dynamic modelling," *Int. Journal Elect. Power Energy Syst.*, vol. 15, no. 5, pp. 315-321, 1993.

[127] C. L. DeMarco, and G. C. Verghese, "Bringing phasor dynamics into the power system load flow," in *Proc. North Amer. Power Symp.*, pp. 463-471, 1993.

[128] P. Zhang, J. R. Marti, and H. W. Dommel, "Shifted-frequency analysis for EMTP simulation of power-system dynamics," *IEEE Trans. Circuits Syst. I*, vol. 57, no. 9, pp. 2564-2574, Sep. 2010.

[129] M. A. Elizondo, F. K. Tuffner and K. P. Schneider, "Three-phase unbalanced transient dynamics and powerflow for modeling distribution systems with synchronous machines," *IEEE Trans. on Power Syst.*, vol. 31, no. 1, pp. 105-115, Jan. 2016.

[130] M. A. Elizondo, F. K. Tuffner and K. P. Schneider, "Simulation of inrush dynamics for unbalanced distribution systems using dynamic-phasor models," *IEEE Trans. Power Syst.*, vol. 32, no. 1, pp. 633-642, Jan. 2017.

[131] K. P. Schneider, F. K. Tuffner, M. A. Elizondo, J. Hansen, J. C. Fuller and D. P. Chassin, "Adaptive dynamic simulations for distribution systems using multi-state load models," *IEEE Trans. Smart Grid*, vol. PP, no. 99, pp. 1-1, Jan. 2018.

[132] M. Maniatopoulos, D. Lagos, P. Kotsampopoulos and N. Hatziargyriou, "Combined control and power hardware in-the-loop simulation for testing smart grid control algorithms," *IET Generation, Transmission & Distribution*, vol. 11, no. 12, pp. 3009-3018, 2017.

[133] P. Kotsampopoulos, F. Lehfuss, G. Lauss, B. Bletterie and N. Hatziargyriou, "The limitations of digital simulation and the advantages of PHIL testing in studying distributed generation provision of ancillary services", *IEEE Trans. Ind. Electron.*, vol. 62, no. 9, pp. 5502-5515, 2015.

[134] S. Leitner, M. Yazdanian, A. Mehrizi-Sani, and A. Muetze, "Small-signal stability analysis of an inverter based microgrid with internal model-based controllers," *IEEE Trans. Smart Grid*, vol. PP, no. 99, pp. 1–10, Mar. 2017.

[135] E. H. Abed, M. A. Hassouneh, and W. A. Hashlamoun, "Modal participation factors revisited: One definition replaced by two," in *Proc. American Control Conf. (ACC)*, St. Louis, MO, USA, June 2009, pp. 1–6.

[136] Y. Li and L. Fan, "Stability analysis of two parallel converters with voltage-current droop control," *IEEE Trans. Power Del.*, vol. 32, no. 6, pp. 2389-2397, Dec. 2017.

[137] Z. Miao, A. Domijan, and L. Fan, "Investigation of microgrids with both inverter interfaced and direct ac-connected distributed energy resources," *IEEE Trans. Power Del.*, vol. 26, no. 3, pp. 1634–1642, July 2011.

[138] IEEE recommended practice for industrial and commercial power system analysis, IEEE Std. 399, 1990.

[139] L. G. Meegahapola, D. Robinson, A. P. Agalgaonkar, S. Perera, and P. Ciufo, "Microgrids of commercial buildings: Strategies to manage mode transfer from grid connected to islanded mode," *IEEE Trans. Sust. Ener.*, vol. 5, no. 4, pp. 1337–1347, Oct. 2014.

[140] Q. C. Zhong and G. Weiss, "Synchronverters: Inverters that mimic synchronous generators," *IEEE Trans. Ind. Electron.*, vol. 58, no. 4, pp. 1259–1267, Apr. 2011.

[141] R. Hesse, D. Turschner, and H.-P. Beck, "Micro grid stabilization using the virtual synchronous machine (VISMA)," in *Proc. Int. Conf. Renewable Energies and Power Quality (ICREPQ)*, Valencia, Spain, Apr. 2009.

[142] K. Sakimoto, Y. Miura, and T. Ise, "Stabilization of a power system with a distributed generator by a virtual synchronous generator function," in *Proc. the 8th Int. Conf. Power Electron. (ECCE Asia)*, Jeju, South Korea, May 2011, pp. 1498–1505.

[143] P. Rodriguez, I. Candela, and A. Luna, "Control of PV generation systems using the synchronous power controller," in *Proc. IEEE Energy Conv. Cong. Expos. (ECCE)*, Denver, Colorado, USA, Sept 2013, pp. 993–998.

[144] J. Morren, J. Pierik, and S. W. de Haan, "Inertial response of variable speed wind turbines," *Electr. Power Syst. Res.*, vol. 76, no. 11, pp. 980–987, 2006.

[145] S. V. Dhople, B. B. Johnson, and A. O. Hamadeh, "Virtual oscillator control for voltage source inverters," in *Proc. of the 51st Ann. Allerton Conf. Commun. Cont. Comput. (Allerton)*, Monticello, Illinois, USA, Oct. 2013, pp. 1359–1363.

[146] S. D'Arco and J. A. Suul, "Virtual synchronous machines- classification of implementations and analysis of equivalence to droop controllers for microgrids," in *Proc. IEEE Grenoble Conf*, Grenoble, France, June 2013, pp. 1–7.

[147] U. Tamrakar, D. Shrestha, M. Maharjan, B. P. Bhattarai, T. M. Hansen, and R. Tonkoski, "Virtual inertia: Current trends and future directions," *Applied Sciences*, vol. 7, no. 7, pp. 1–29, June 2017.

[148] Reciprocating internal combustion engine driven alternating current generating sets- Part 5: Generating sets, International Organization for Standardization Std. ISO 8528-5:2005(E), 2005.

[149] P. A. Mendoza-Araya and G. Venkataramanan, "Stability analysis of ac microgrids using incremental phasor impedance matching," *Electric Power Components and Systems*, vol. 43, no. 4, pp. 473–484, Feb 2015.

[150] N. T. Janssen, R. A. Peterson, and R. W. Wies, "Development of a full-scale-lab-validated dynamic Simulink© model for a stand-alone wind-diesel microgrid," in *Proc. ASME Power Conference*, 2014.

[151] N. T. Janssen, R. W. Wies, and R. A. Peterson, "Frequency regulation by distributed secondary loads on islanded wind-powered microgrids," *IEEE Trans. Sust. Energy*, vol. 7, no. 3, pp. 1028-1035, Jul 2016.

[152] R. W. Wies, N. T. Janssen, and R. A. Peterson, "Distributed self-sensing secondary loads for frequency regulation in wind-powered islanded microgrids," in *Proc. IEEE Power and Ener. Soc. Gen. Meet.*, Denver, CO, Jul 2015.

[153] R. W. Wies, N. T. Janssen, and R. A. Peterson, "Autonomous distributed secondary loads for sole frequency regulation in high penetration wind-diesel microgrids," in *Proc. IEEE Power and Ener. Soc. Gen. Meet.*, Chicago, IL, Jul 2017.

[154] J. F. Manwell, J. G. Mcgowan, and A. L. Rogers, *Wind energy explained: theory, design, and application (second edition)*, West Sussex, United Kingdom: Wiley, 2009.

[155] F. C. Kaminsky, "A comparison of alternative approaches for the synthetic generation of a wind speed time series," *Journal of Solar Energy Engineering*, vol. 113, no. 4, pp. 280–289, 1991.

[156] P. Kotsampopoulos, V. Kleftakis, N. Hatziargyriou, "Laboratory education of modern power systems using PHIL simulation", *IEEE Trans. Power Syst.*, vol. 32, no. 5, pp. 3992-4001, Sept. 2017.